Technische Universität München
Institut für Energietechnik

Lehrstuhl für Thermodynamik

Pollutant Formation in Premixed Natural Gas Swirl Flames with Water Injection

Stephan Eugen Maximilian Lellek

Vollständiger Abdruck der von der Fakultät für Maschinenwesen der Technischen Universität München zur Erlangung des akademischen Grades eines

DOKTOR – INGENIEURS

genehmigten Dissertation.

Vorsitzender:
Prof. Dr.-Ing. Volker Gümmer
Prüfer der Dissertation:
1. Prof. Dr.-Ing. Thomas Sattelmayer
2. Prof. dr.ir. Sikke Klein,
   Technische Universiteit Delft

Die Dissertation wurde am 10.05.2017 bei der Technischen Universität München eingereicht und durch die Fakultät für Maschinenwesen am 11.08.2017 angenommen.

Vorwort

Die hier vorliegende Arbeit entstand während meiner Forschungstätigkeit am Lehrstuhl für Thermodynamik der Technischen Universität München. Die interdisziplinäre Forschung zur Flexibilisierung von Gasturbinenkraftwerken im Rahmen des Verbundprojekts "Energy Valley Bavaria" wurde durch die Munich School of Engineering (MSE) und das Bayerische Staatsministerium für Bildung und Kultus, Wissenschaft und Kunst gefördert.

Mein besonderer Dank gilt meinem Doktorvater Herrn Prof. Dr.-Ing. Thomas Sattelmayer für die wissenschaftliche Betreuung der Arbeit. Das in mich gesetzte Vertrauen und die gestalterische Freiheit bei der Bearbeitung des Projekts wusste ich zu jeder Zeit sehr zu schätzen. Herrn Prof. dr.ir. Sikke Klein danke ich für die freundliche Übernahme des Koreferates und Herrn Prof. Dr.-Ing. Volker Gümmer für die Übernahme des Prüfungsvorsitzes.

Für die harmonische und lehrreiche Zusammenarbeit im Projekt danke ich Nico Stadlmair und Max Baumgärtner, sowie allen weiteren Projektpartnern. Vielen Dank auch an Dr.-Ing. Vera Hoferichter, meiner langjährigen Bürokollegin, für die zahlreichen fachlichen Diskussionen und das Probelesen dieser Arbeit. Weiterhin danke ich allen ehemaligen Studenten für ihren Einsatz und die tatkräftige Unterstützung. Besonders hervorzuheben ist hierbei Christoph Barfuß, mit dem ich viele arbeitsreiche Stunden im Labor verbringen durfte. Allen Kolleginnen und Kollegen danke ich für die freundschaftliche Atmosphäre am Lehrstuhl und die schönen Erinnerungen an unsere gemeinsame Zeit.

Abschließend gebührt der größte Dank meiner Familie. Vielen Dank an meine Eltern, die mich während meiner langen Ausbildungszeit immer bedingungslos unterstützt haben und stets ein offenens Ohr für mich hatten. Herzlichen Dank auch an Theresa für die Unterstützung, die Motivation und dein Verständnis.

Garching, im Oktober 2017 Stephan Lellek

Zusammenfassung

Der steigende Anteil an erneuerbaren Stromerzeugern im europäischen Stromnetz führt zu wachsenden Schwankungen in der Stromproduktion. Eine Maßnahme zum Ausgleich dieser Schwankungen ist der Einsatz von Gasturbinenkraftwerken mit erweitertem Betriebsbereich. In dieser Arbeit wird deshalb das Potential zur Leistungssteigerung durch Injektion von flüssigem Wasser in die Gasturbinenbrennkammer untersucht. Besonderer Wert wird auf den Einfluss des Wassers auf Schadstoffemissionen der Gasturbine gelegt. Ein Betrieb der Gasturbine soll trotz Leistungssteigerung innerhalb der gesetzlich vorgegebenen Grenzwerte möglich sein. Die Machbarkeit der Wasserinjektion in vorgemischten Gasturbinenbrennkammern wird anhand von Untersuchungen in einem Einzelbrennerprüfstand gezeigt. Des Weiteren werden Wärmefreisetzung und Schadstoffentstehung mittels experimenteller Untersuchungen erforscht. Der Einfluss des flüssigen Wassers auf den Verbrennungsvorgang wird untersucht und geeignete Betriebsbedingungen der vorgemischten Verbrennung mit Wasserinjektion werden identifiziert.

Abstract

Rising shares of renewable power producers in the European energy grid lead to increasing fluctuations in power generation. A measure to compensate for these fluctuations would be the use of gas turbines with an expanded operating range. For that reason, this thesis investigates power augmentation of gas turbines due to the injection of liquid water. The focus of this work especially lies on pollutant formation. Despite the power augmentation, operation of the gas turbine shall be possible within the boundaries of given emission legislation. At first the feasibility of water injection in premixed gas turbine combustors is shown using an atmospheric single burner test rig. Subsequently, heat release as well as pollutant formation are investigated with experimental and numerical methods. Finally, the influence of water injection on the combustion process is determined and favorable operating conditions of water injected premixed combustion are identified.

Contents

List of Tables

List of Figures

Nomenclature

Latin Letters

$[A]$	Molar concentration of species A [mol/m^3]
A	Pre-exponential factor in the Arrhenius equation [s^{-1}]
A_{l}	Laminar flame surface [m^2]
$A_{\mathrm{g,out}}$	Cross-sectional are of the air nozzle outlet [m^2]
A_{P}	Projected area of the particle [m^2]
A_{t}	Turbulent flame surface [m^2]
B_{M}	Spalding mass transfer number [-]
B_{T}	Spalding heat transfer number [-]
c	Reaction progress variable [-]
c_{D}	Drag coefficient [-]
$[CO_2]$	Concentration of carbon dioxide [mol/m^3]
$[CO]$	Concentration of carbon monoxide [mol/m^3]
c_{p}	Specific heat [J/(kg K)]
$\overline{c}_{\mathrm{p,i}}\vert_{T_{\mathrm{ref}}}^{T_{\mathrm{i}}}$	Specific heat averaged between T_{ref} and T_{i} [J/(kg K)]
D	Diffusivity [m^2/s]
d	Droplet diameter [μm]
D_{tu}	Tube diameter [m]
$d_{\mathrm{V,10}}$	D10 representative diameter [μm]
$d_{\mathrm{V,32}}$	Sauter mean diameter [μm]
$d_{\mathrm{V,50}}$	D50 representative diameter [μm]
$d_{\mathrm{V,90}}$	D90 representative diameter [μm]
E_{A}	Activation energy [J/mol]
$E(k_{\mathrm{w}})$	Turbulent energy [J]

F_{A}	Aerodynamic force [N]
F_{D}	Drag force [N]
F_{G}	Gravity force [N]
F_{i}	Force [N]
F_{P}	Pressure force [N]
F_{σ}	Surface tension force [N]
F_{μ}	Viscous force [N]
GLR	Gas to liquid ratio [-]
$\dot{H}^0$	Enthalpy flux at standard conditions [W]
$h^0_{\mathrm{f,i}}$	Enthalpy of formation of species i at standard conditions [J/mol]
H_{LHV}	Lower heating value [MJ/kg]
$\dot{H}$	Enthalpy flux [W]
$I(x,r)$	Intensity at radial position r and axial position x [-]
I_{r}	Relative turbulence intensity [-]
I_{tot}	Total intensity [-]
k	Turbulent kinetic energy [m^2/s^2]
k_{RR}	Reaction rate coefficient for a first order reaction [s^{-1}]
k_{W}	Wave number [m^{-1}]
K	Evaporation constant [m^2/s]
L	Characteristic length scale [m]
l_{δ}	Reaction zone thickness [m]
l_{t}	Characteristic turbulent length scale [m]
m	Partial reaction order for molecule A [-]
$\dot{m}$	Mass flow rate [kg/s]
n	Partial reaction order for molecule B [-]
n	Rotational speed [Hz]
$\dot{n}_{\mathrm{i}}$	Molar flow rate of species i [mol/s]
p	Pressure [Pa]
P	Power output [W]
q_3	Volume fraction [-]
Q_3	Cumulative volume fraction [-]
$\dot{Q}$	Heat flux [W]
r	Radial coordinate [mm]
R	Universal gas constant [J/(kmol K)]

t	Time [s]
s_L^0	Laminar flame speed [m/s]
s_t	Turbulent flame speed [m/s]
$\mathrm{SM}_\mathrm{Comp}$	Compressor surge margin [%]
T	Temperature [K]
$\frac{\partial T}{\partial x}$	Temperature gradient [K/m]
$\mathrm{TIT}_\mathrm{ISO}$	Turbine inlet temperature according to ISO 2314 [K]
u	Flow speed [m/s]
$\overline{u}$	Average velocity [m/s]
u'	Velocity fluctuation [m/s]
v	Reaction rate [mol/(m^3 s)]
x	Axial coordinate [mm]
Y_D	Mass fraction [kg/kg]

Greek Letters

α	Empiric coefficient [-]
α_1	Angle [°]
α_P	Heat transfer coefficient [W/(m^{2}K)]
δ_F^0	Laminar flame thickness [mm]
β	Empiric coefficient [-]
$\Delta h_\mathrm{HL,dry}$	Enthalpy loss at dry operating conditions [J/kg]
ΔH_R^0	Reaction enthalpy [J/mol]
Δh_Vap	Vaporization enthalpy [J/kg]
ϵ	Turbulent dissipation rate [m^2/s^3]
η	Efficiency [-]
η_l	Dynamic viscosity [Pa s]
η_k	Kolmogorov scale [m]
$\gamma_\mathrm{N2,air}$	Mole fraction of nitrogen in air [-]
$\gamma_\mathrm{O2,air}$	Mole fraction of oxygen in air [-]
κ	Heat capacity ratio [-)]
λ	Thermal conductivity [W/(mK)]

ν	Kinematic viscosity [m^{2}s]
Ω	Water to fuel ratio [-]
Π	Pressure ratio [-]
Φ	Equivalence ratio [-]
ρ	Density [kg/m^3]
σ_l	Surface tension [N/m]
τ_c	Characteristic chemical timescale [s]
τ_k	Kolmogorov timescale [s]
τ_t	Characteristic turbulent timescale [s]

Dimensionless numbers

Da	Damköhler number
Ka	Karlovitz number
Ka_δ	Karlovitz number in the reaction layer
Nu	Nußelt number
Oh	Ohnesorge number
Pr	Prandtl number
Re	Reynolds number
Sc	Schmidt number
We	Weber number

Acronyms and Abbreviations

C1	Nozzle configuration C1
C2	Nozzle configuration C2
CO_2	Carbon dioxide
COI_x	Axial center of the OH* intensity
COI_r	Radial center of the OH* intensity
FAR	Fuel to air ratio
FL	Flame length

HRSG	Heat recovery steam generator
IRZ	Inner recirculation zone
NO_x	Nitrogen oxide
ORZ	Outer recirculation zone

Subscripts

0	Value at reference conditions
ad	Value at adiabatic conditions
a	Air property
at	Atomizing air property
ax	Axial component
b	Value in the burnt mixture
CC	Values in the combustion chamber
Comp	Values in the compressor
cond	Transport due to heat conduction
conv	Transport due to convection
Cool	Value for cooling air
crit	Critical value
dry	Value at dry operating conditions
eq	Equilibrium value
est	Estimated value
f	Fuel property
g	Gas property
gas	Values for the regime of secondary atomization
glob	Global value
GT	Gas turbine
heatup	Value for the heatup process
i	Value for component i
in	Value at the inlet
∞	Value at an infinity distance
is	Isentropic values

l	Liquid property
max	Maximum value
meas	Experimentally measured value
norm	Normalized value
OH*	Value determined from OH* measurements
out	Value at the outlet
P	Value for a particle
ϕ	Circumferential component
pol	Polytropic values
pre	Value for preheating conditions
Prod	Products
r	Relative component
rad	Radial component
radi	Transport due to radiation
Reac	Reactants
red	Reduced values
ref	Value at reference conditions
s	Steam property
S	Value at the surface
st	Value at stoichiometric operation
t	Turbulent value
Turb	Value in the turbine
u	Value in the unburnt mixture
vap	Transport due to vaporization
w	Water property
wet	Value at water injected operation

1 Motivation

1.1 New Challenges in a Changing Energy Market

Fossil and nuclear power production have dominated the energy infrastructure in the industrialized countries for a long time. Due to the high availability of fossil fuels as well as low prices of nuclear power production, both technologies contributed to the rise of wealth and importance of today's leading economies. However, recent events have led to a change in the mindset of these societies. Starting in the 1970s, the public awareness for environmental pollution due to the industrialization started to rise. Ongoing research about the harmfulness of air pollutants as well as the increasing effects of global warming intensified this perception about the extensive use of fossil fuels. Similar developments are found for power production from nuclear energy sources. Especially due to the public discussion about permanent disposal sites for nuclear waste, people became aware of the problems of nuclear energy. Finally, the catastrophic events of Fukushima in 2011 led to a fundamental change in the public opinion on nuclear power production.

The increasing environmental awareness in Europe consequently led to changes in the use of valuable resources as well as a rising demand for sustainability in many aspects of daily life. Due to its high contribution to global pollutants and its low level of sustainability, the power production sector was also strongly influenced by this development. In many countries in Europe and especially in Germany the share of power production from renewable energy sources increased quickly and reduced shares of nuclear as well as fossil power production ([11], see Fig. 1.1).

However, due to the changed topology of the old and the new power producers, this progressive development leads to problems in the existing electri-

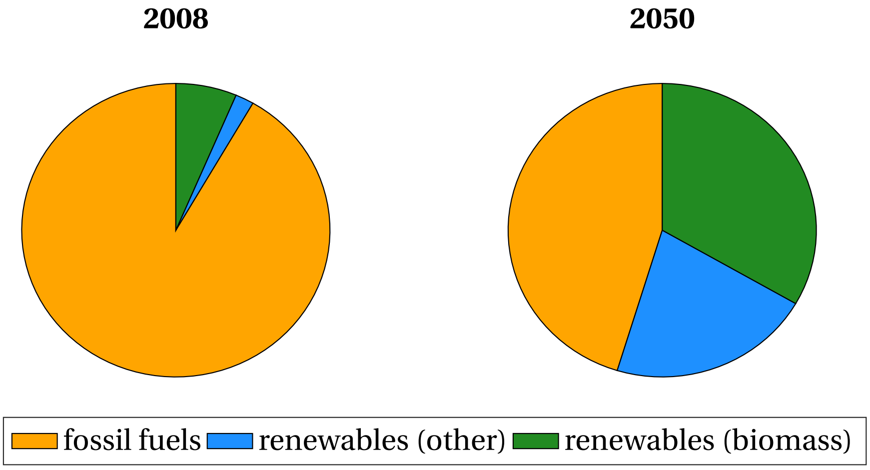

Figure 1.1: Changing shares of renewable power production between 2008 and 2050. Adapted from [23].

cal grid. As the power production infrastructure in many industrialized countries is based on fossil power production, the quick introduction of renewable power producers puts stress on the existing power production systems. Due to the stochastic nature of many renewable energy sources like wind or sun, these power producers show a strongly fluctuating power output. As shown in Fig. 1.2 this development is going to intensify with rising shares of renew-

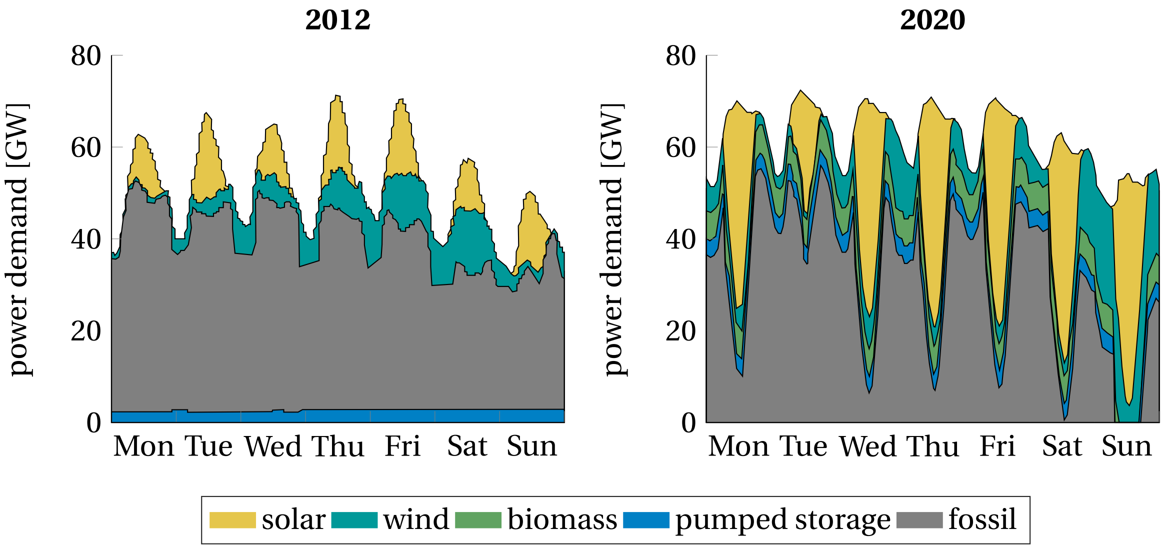

Figure 1.2: Changes in the fluctuations of the power output of renewables between 2012 and 2020. Adapted from [54].

able power production. Nevertheless, conventional power producers are required to compensate the output fluctuations of the renewables in order to guarantee the security of power supply. Due to a low level of pollutant emissions as well as short start up times, gas turbines are a key technology during this transition from fossil to renewable power production. However, in order to deal with the rising output fluctuations of the renewables, further development of the gas turbine technology is necessary. Shorter engine start up times as well as an increased range of operation are of particular importance. This thesis investigates the enhancement of the flexibility with an increase of the operational range to higher loads. As the load fluctuations of the renewables are limited in time, research focuses on the short-time power augmentation of gas turbines. In order to comply with the strict environmental legislation, this power augmentation should be reached without increasing the pollutant concentration in the exhaust gas. The new technology should feature a simple operating principle as well as a setup similar to modern gas turbine burners, thereby allowing a retrofit to existing machines in the ideal case. After an assessment of the possible power augmentation technologies, water injection in the combustion chamber has been identified as the most promising approach. In the following, water injection in gas turbine combustors is introduced briefly, before the structure of this thesis is described.

1.2 Water Injection in Gas Turbine Combustors

The application of water injection is not new in the context of gas turbines. In gas turbine history, water and steam injection have already found multiple applications as a measure to increase the power output [12] or to control nitrogen oxide emissions [32]. In the 1960s, water injection has first been used in aero-engines for thrust augmentation at take-off. In this context, Daggett shows detailed sketches of the water injection systems in Pratt and Whitney engines of Boeing 707 and 747 airplanes [17]. It was possible to increase power output of the engines by 35 % on a hot day [17]. Besides the use in aircraft engines, water and steam injection also found application to stationary gas turbines. Although the benefits of steam injection were already known since the early 20th century [32], the interest in this technology did not start to rise until the 1970s. Companies like GE or Rolls-Royce tried to use the huge potential of steam injection in industrial gas turbines with non-premixed combustion and developed steam injected combustion systems which are still in operation. Well known systems with water and steam injection are the GE Sprint technology [5] and the Cheng cycle [14]. With the search for rising efficiencies and increasing power output, the number of gas turbine cycles with water and steam injection increased over the years. The StIG-cycle (Steam Injected Gas turbine) and the HAT cycle (Humid Air Turbine) are among the well known examples for steam injected cycles. As the high amounts of water used for NO_x control of stationary gas turbines started to generate problems with the carbon monoxide emissions, better technologies for the NO_x control were developed [69]. In the early 1990s, the introduction of premixed combustion [32] allowed to control the pollutant emissions without water injection and quickly led to the decline of water injected turbomachinery.

However, with the new challenges in the power production market, water and steam injection in gas turbines have become a focus in gas turbine research again. Strict emission regulations as well as a rising demand for power led to efforts to exploit the huge potential of water injection for premixed gas turbine engines, too. Besides the typical problems of water or steam injected gas turbines, the lower flame stability in premixed combustors leads to additional challenges. Nevertheless, recently the feasibility of steam injection in premixed gas turbine combustors was shown for a wide range of operating conditions at TU Berlin [27]. Due to the lower complexity of water injected systems compared to steam injection, the capital cost (CAPEX) for a water injected gas turbine is lower. This gives additional incentives for the use of water injected premixed combustion systems. Therefore, this thesis investigates the influence of water injection on the combustion process in a gas turbine combustor. More specifically, the addition of water droplets in premixed natural gas flames is investigated under typical operating conditions of modern gas turbines. The aim of this work is to achieve power augmentation in a gas turbine burner at a constant level of pollutant emissions.

1.3 Goals and Structure of This Thesis

This section briefly outlines the structure of this thesis and gives an overview over the different chapters. In chapter 2, the fundamentals of fluid mechanics and thermodynamics are introduced.

In order to foster the understanding of the effect of water injection in gas turbines, a global thermodynamic study is conducted in chapter 3. The potential of water injection for power augmentation is clarified using this global analysis. Operating characteristics of typical modern heavy duty gas turbines are analyzed and the potential for a retrofit of a water injection system is determined. Furthermore, the influence of water injection on the reactivity of fuel air mixtures as well as the effects on pollutant formation are discussed.

The stable operation of water injected premixed combustion is shown in a lab scale combustor under typical gas turbine operating conditions. In Chapter 4, a water injection system is introduced and combined with a generic gas turbine burner. The water injection system is retrofitted to an existing single burner test rig to preserve the positive features of the burner configuration. Similar to the other parts of the test rig, the water injection system is designed with a high level of flexibility and multiple degrees of freedom. This allows the operation within a wide range of operating conditions.

The results of the experimental investigations are presented in chapters 5 and 6. In order to characterize the combustion chamber performance with water injection, the heat release distribution is determined in chapter 5 for a wide range of water mass flow rates and flame temperatures. Subsequently, global flame parameters like flame position and flame length are extracted to allow a quantitative correlation with the turbulent flame speed of the reactant mixtures. Furthermore, the spatial distribution of the liquid water in the combustor is determined in Mie scattering investigations to identify inhomogeneous water distributions in the test rig. In order to understand the water influence on pollutant formation, global CO and NO_x concentrations are investigated in chapter 6 for different equivalence ratios and different water to fuel ratios. The experimental CO results are linked to reaction kinetic simulations in Cantera in order to separate CO from equilibrium reactions and CO originating from quenching reactions. In the second step, spatially resolved species concentration measurements are conducted for a smaller range of operating points to get a deeper insight into pollutant formation at water injected conditions. Finally, the dominating influence of the water droplet size on the pollutant formation is shown for CO as well as NO_x formation.

The thesis concludes with a summary of the key findings. Furthermore, the results are used to give an outlook on the possible future of water injected combustion in gas turbines.

2 Theoretical Background

This chapter presents the theoretical background required in this work. The first part outlines the underlying fluid mechanic principles of turbulent and multiphase flows. Furthermore, the atomization of water in different nozzle types is discussed. Subsequently, this chapter presents the fundamentals of turbulent premixed combustion systems. Besides the modeling of laminar and turbulent flames, the focus of the combustion section lies on pollutant formation.

2.1 Basics of Fluid Mechanics

2.1.1 Turbulence in Fluid Flows

In technical flows, the laminar and turbulent flow regimes are separated by the critical Reynolds number. This Reynolds number relates the inertial forces in a flow to the viscous forces:

$$\mathrm{Re} = \frac{\text{inertial forces}}{\text{viscous forces}} = \frac{uL}{\nu} \tag{2.1}$$

In contrast to laminar flows, turbulent flows are characterized by temporal and spatial fluctuations of all flow variables which occur stochastically and can not be predicted. Typically, these variables fluctuate around a mean value which allows a mathematical description of turbulent flows. If the flow properties are averaged over time, an average value $\overline{(\,)}$ and a fluctuating value $(\,)'$ are obtained. While the mean value is solely dependent on the spatial location, the turbulent fluctuations show a dependency on time and location. For the turbulent velocity, this relation can be described with

$$u(x,t) = \overline{u(x)} + u'(x,t)\ . \tag{2.2}$$

The turbulent fluctuations $u'(x,t)$ in the flow are related to vortices (eddies) of different sizes. These vortices perturbate the mean flow $\overline{u(x)}$ and create a turbulent three dimensional flow field. Typically, the size of the largest eddies in a flow is determined from a characteristic length scale. For a turbulent flow in a cylindrical tube of diameter D_{tu} the size of the largest eddies can be determined according to

$$l_{\mathrm{t}} = 0.07 D_{\mathrm{tu}}. \tag{2.3}$$

Analogous to the turbulent length scale, a turbulent time scale τ_{t} is introduced:

$$\tau_{\mathrm{t}} = \frac{l_{\mathrm{t}}}{u'}. \tag{2.4}$$

Experimental investigations from Richardson [61] have shown that these large eddies are unstable and collapse, forming smaller vortices. Subsequently, these smaller eddies break down until the smallest eddies are dissipated in the viscous subrange. Similar to l_{t}, a measure for the smallest eddies in a turbulent flow can be determined. This Kolmogorov scale η_{k} can directly be calculated with the kinematic viscosity ν of the fluid and the volumetric dissipation rate ϵ of the flow:

$$\eta_{\mathrm{k}} = \left(\frac{\nu^3}{\epsilon}\right)^{\frac{1}{4}} \tag{2.5}$$

Similar to τ_{t} a timescale of the smallest turbulent eddies is introduced:

$$\tau_{\mathrm{k}} = \left(\frac{\nu}{\epsilon}\right)^{\frac{1}{2}}. \tag{2.6}$$

The energy content of the different vortices is directly related to their size. Bigger eddies have a higher content of turbulent kinetic energy, whereas the energy content of small vortices is low. Generally, turbulent kinetic energy is produced at the largest turbulent scales in the flow. Subsequently, energy is transferred from the large vortices to the smaller ones in the turbulent energy cascade (see Fig. 2.1) before dissipation of the turbulent kinetic energy occurs at scales smaller than the Kolmogorov scale.

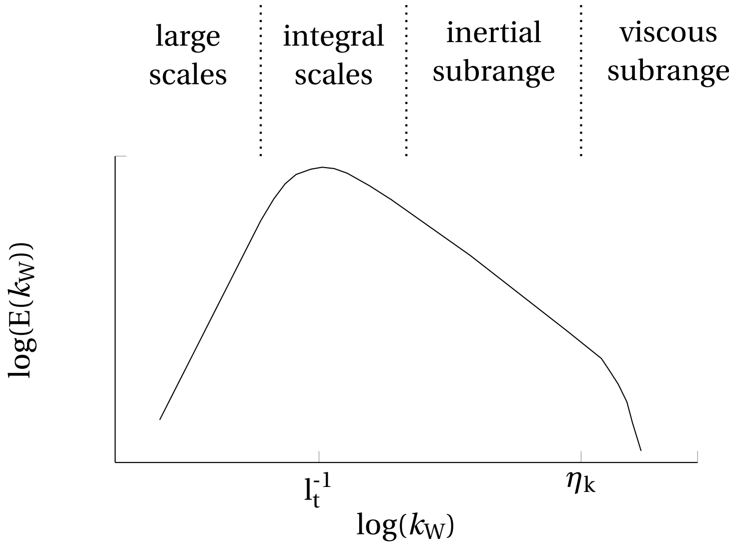

Figure 2.1: Energy cascade in turbulent flows. Adapted from [58].

2.1.2 Spray Dynamics

In order to describe fluid droplets in a gas flow, basic modeling approaches of multiphase flows have to be considered. For the modeling of sprays usually the Euler-Lagrange approach is employed. In this approach, the conservation equations are only solved for the gas phase. The interactions with the dispersed phase are modeled through balance equations applied to each particle or droplet. Assuming low particle concentration, the interaction of particles with each other can be neglected. Starting from the velocity field of the continuous phase, the forces on a particle with constant mass are described with a momentum balance:

$$m_P \frac{d\, u_P}{dt} = \sum F_i = F_D + F_P + F_G + \ldots \, . \tag{2.7}$$

The momentum of a particle can be determined with the particle mass m_P and its velocity u_P, whereas major contributions to the momentum balance come from the drag force F_D, pressure gradients in the main flow F_P and forces of gravity and buoyancy F_G. Typically the influences of pressure gradients, gravity and buoyancy on particle motion are of minor importance compared to the drag force.

Influences on the drag force are the size and shape of the particle, the viscosity of the surrounding fluid as well as the relative velocity between droplet and fluid. At steady state conditions (without accelerating or decelerating forces acting on the droplet) the drag force at a single particle is described by

$$F_{\mathrm{D}} = \frac{1}{2}\rho c_{\mathrm{D}} A_{\mathrm{P}} \left(u - u_{\mathrm{P}}\right)^2 \ . \tag{2.8}$$

In this formula c_{D} is the drag coefficient of the particle whereas A_{P} stands for the projected surface of the particle in flow direction. As this formula is based on the steady state assumption the effects of turbulence in the continuous flow are not considered. However, in order to show the effects of flow turbulence on droplet motion, turbulent droplet dispersion is discussed at the end of this section.

The drag coefficient is a dimensionless number that describes the multiple dependencies of the particle drag on particle properties as well as the flow state of the continuous flow [3]. As shown in section 2.1.1, the flow state of the continuous phase is often described by the Reynolds number. In order to describe processes involving relative motion between a particle and the main flow Re_{P} is calculated from the relative velocity between particle and fluid:

$$\mathrm{Re}_{\mathrm{P}} = \frac{d_{\mathrm{P}} \left|u - u_{\mathrm{P}}\right|}{\nu} = \frac{d_{\mathrm{P}} u_{\mathrm{r}}}{\nu} \tag{2.9}$$

Figure 2.2 shows the dependency of the drag coefficient of a spherical particle on the particle Reynolds number at steady state conditions. Three different regimes can be identified in Fig. 2.2. For $\mathrm{Re}_{\mathrm{P}}<1$ a linear dependence of c_{D} on the Reynolds number is found. This regimes is called the Stokes flow regime. Neglecting the inertial terms in the Navier-Stokes equations Stokes was able to derive an analytic solution for the flow around a spherical particle. In this regime the drag coefficient is described by

$$\mathrm{c}_{\mathrm{D}} = \frac{24}{\mathrm{Re}_{\mathrm{P}}} \ . \tag{2.10}$$

With increasing Reynolds numbers the flow behind the droplet forms vortices and begins to separate. The deviations from the Stokes drag law rise and an analytical solution of the Navier Stokes equations does not exist anymore. Nevertheless, multiple numerical as well as empirical solutions are given in literature [38, 62]. In order to calculate c_{D} over a wide range of Re_{P}, Lefebvre [42]

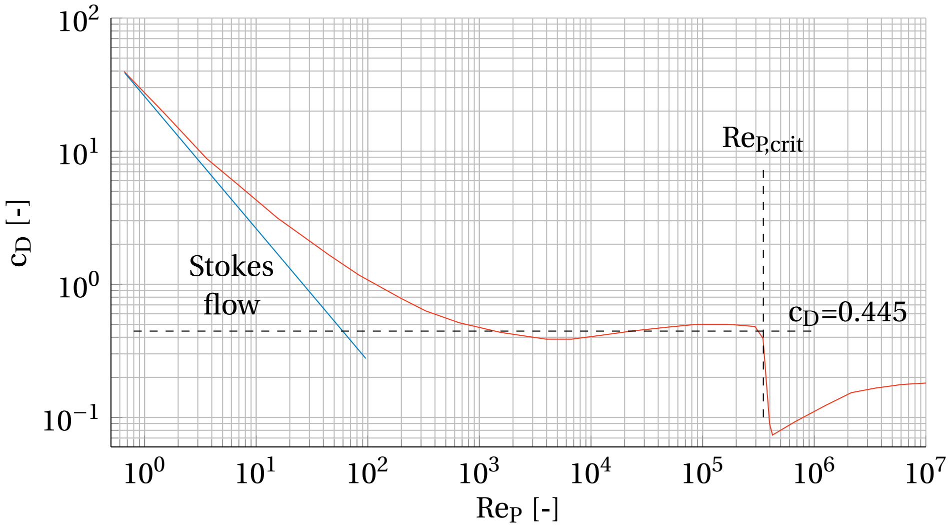

Figure 2.2: Dependency of the drag coefficient of a spherical droplet on the Reynolds number. Adapted from [16].

suggests to use the empirical correlation of Putnam [64]:

$$c_D = \frac{24}{Re_P}\left(1 + \frac{1}{6}Re_P^{2/3}\right) . \tag{2.11}$$

This correlation is valid for $Re_P<1000$. If the Reynolds number is even higher, the laminar boundary layer around the particle separates and c_D takes an almost stable value of 0.445 over a wide range of Re_P ($1000 < Re_P < 3.5 \cdot 10^5$). According to Crowe [16], this regime is called the regime of Newton's drag law. For Reynolds numbers above $Re_{P,crit}$ the boundary layer of the droplet becomes turbulent and the flow behind the droplet suddenly reattaches which leads to a strong reduction of c_D. According to [9] the exact value of $Re_{P,crit}$ depends on the surface quality of the particle. For rough surfaces the critical Reynolds number is shifted to lower values whereas higher $Re_{P,crit}$ are found for smooth particle surfaces.

In order to calculate the drag force of a particle as realistic as possible, further influences on c_D have to be taken into account. These influences include unsteady flow around the particle, non-spherical particles, droplet evaporation as well as interactions between different particles. As the focus of this thesis lies on combustion phenomena, the different effects on c_D are not described here. Nevertheless, further information on these effects can be found in [16]

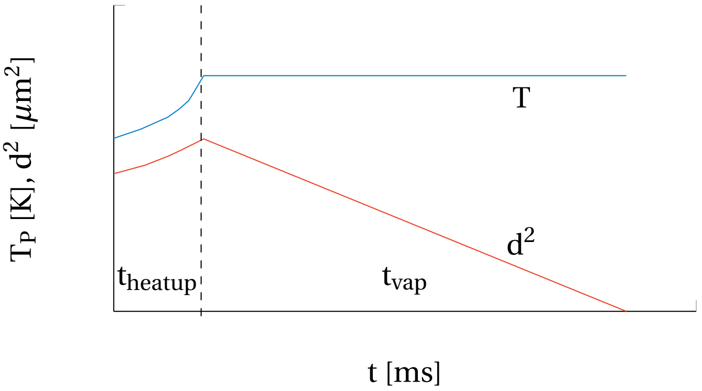

Figure 2.3: Droplet diameter and droplet temperature of an evaporating droplet over time. Adapted from [74].

and [42].

In order to consider heat transfer processes between the particles and the continuous phase, an energy balance for the particles is employed. Similar to momentum conservation, the energy conservation equation is solved only for the continuous phase. The energy balance at the droplet is described by

$$m_P c_P \frac{dT_P}{dt} = \sum \dot{Q}_i = \dot{Q}_{cond} + \dot{Q}_{conv} + \dot{Q}_{radi} + \dot{Q}_{vap} + \ldots \quad (2.12)$$

In this equation the enthalpy of the particle is calculated from the particle mass m_P, the heat capacity of the particle c_P as well as its temperature T_P. Relevant heat fluxes for particles are conductive heat transfer $\dot{Q}_{cond}$, convective heat transfer $\dot{Q}_{conv}$ as well as heat transfer due to radiation $\dot{Q}_{radi}$. For droplets in hot environments, the influence of vaporization $\dot{Q}_{vap}$ has to be considered additionally. In the case of vaporization, energy is transferred from the continuous phase to the droplet while mass transfer occurs in the opposite direction. While the heat transfer to the droplet is described by Eq. 2.12, the mass balance at the droplet is calculated with

$$\frac{dm_P}{dt} = -\dot{m}_{vap} \; . \quad (2.13)$$

Given certain simplifications, evaporation of a droplet can be described analytically [1]. This allows to determine the evaporation time of a given droplet.

---

[1] Among others, the temperature profile in the droplet is assumed to be one-dimensional.

As shown in Fig. 2.3, the evaporation of a droplet consists of 2 different stages: A heating phase and an evaporation phase. After the generation of a droplet from a continuous liquid phase the temperature of the droplet is low. Consequently, the evaporation rate $\dot{m}_{\mathrm{vap}}$ is small. If the temperature of the surrounding gas phase lies above the droplet temperature, heat is transferred to the droplet, thereby raising the droplet temperature. Due to the lower density of the droplet at higher temperatures the diameter of the droplet increases slightly. At higher droplet temperatures the evaporation rate rises. For droplets consisting of only one substance the temperature of the droplet rises until the wet-bulb temperature[2] is reached. From this point on all heat that is transferred to the droplet is used for the evaporation of the droplet instead of inert heating of the droplet. Given certain simplifications, the processes occurring during this stage of droplet evaporation can approximately be described with the d^2-law:

$$d^2(t_0) - d^2(t) = K \cdot (t - t_0)\ . \tag{2.14}$$

The d^2-law is derived for a single, spherical droplet with a homogeneous droplet temperature that is equal to the boiling temperature of the liquid. The droplet consists of a pure substance and transfer processes to and from the droplet occur solely by heat and mass diffusion, respectively. Furthermore, steady state evaporation as well as a constant Sherwood number are assumed. A complete list of the simplifications as well as a detailed derivation of the d^2-law are shown by Turns [79]. As described by Eq. 2.14, the quadratic diameter of a droplet (d^2) linearly depends on time via the evaporation constant K. For equal diffusivities of heat and mass (Lewis number Le=1) K can be calculated according to

$$K = 8\frac{\lambda_{\mathrm{g}}}{c_{\mathrm{p,g}}\rho_{\mathrm{P}}}\ln(1+B)\ . \tag{2.15}$$

In this equation λ_{g} stands for the mean thermal conductivity of the surrounding gas while $c_{\mathrm{p,g}}$ denotes the mean specific heat capacity of the gas phase. Lefebvre [42] points out that the temperature dependent values of λ_{g} and $c_{\mathrm{p,g}}$ strongly influence the exact value of K. Therefore, the temperature at which these values are determined is of great interest. Besides this, B denotes the transfer number, a measure for the driving force during evaporation. Depend-

---

[2] Note that this temperature lies below the boiling temperature of the liquid.

ing on the driving force for the evaporation process, either a heat transfer number or a mass transfer number are used [42]. If the driving force of the evaporation process is the heat transfer to the droplet a heat transfer number is used for the calculation of K:

$$B_{\mathrm{T}} = \frac{c_{\mathrm{p,g}}(T_\infty - T_{\mathrm{S}})}{\Delta h_{\mathrm{vap}}} \tag{2.16}$$

T_∞ stands for the temperature of the continuous phase at an infinity distance from the droplet, T_{S} denotes the temperature at the droplet surface and Δh_{vap} is the heat of vaporization of the liquid at ambient pressure. If the driving force of the evaporation process is the mass transfer to the continuous phase a mass transfer number is used instead:

$$B_{\mathrm{M}} = \frac{Y_{\mathrm{D,S}}}{1 - Y_{\mathrm{D,S}}} \tag{2.17}$$

The only influencing parameter of the mass transfer number is the mass fraction of the evaporating species in the gas phase at the surface of the droplet ($Y_{\mathrm{D,S}}$). Additional information on the determination of $Y_{\mathrm{D,S}}$ can be found in the work of Lefebvre [42]. Given the assumption of steady state evaporation, B_{T} is identical to B_{M} and either of the two transfer numbers can be used to calculate the evaporation constant K.

Although the d^2-law is based on many assumptions, it serves as a good approximation of the complex processes occurring during droplet evaporation. However, in technical applications heat transfer to the droplet is typically not limited by diffusive heat transfer. In order to quantify the convective heat transfer to the droplet the Nußelt number is introduced:

$$\mathrm{Nu} = \frac{\alpha_{\mathrm{P}} d_{\mathrm{P}}}{\lambda_{\mathrm{g}}} \, . \tag{2.18}$$

The non-dimensional Nußelt number relates the heat transfer due to convection to the conductive heat transfer. Consequently, it quantifies the factor by which heat transfer to the droplet is enhanced due to convection. Depending on the geometry of the particle different relations are available that allow to calculate Nu from the Reynolds number of the flow and the Prandtl number of the fluid [3]. Multiple empirical correlations describe the Nußelt number for a flow around a spherical droplet. Often, the equation by Ranz and Marshall [65] is used:

$$\mathrm{Nu} = 2 + 0.6\mathrm{Re}_{\mathrm{P}}^{0.5}\mathrm{Pr}_{\mathrm{g}}^{0.33} \,. \tag{2.19}$$

If heat transfer to the droplet happens solely by heat conduction the Nußelt number assumes a value of 2, whereas higher values are found if convective heat transfer occurs. Introducing the correlation of Ranz and Marshall into Eq. 2.15 the influence of convection on the evaporation of a spherical droplet can be modeled:

$$K = 8\frac{\lambda_{\mathrm{g}}}{c_{\mathrm{p,g}}\rho_{\mathrm{P}}}\ln(1+B)\left(1 + 0.3\mathrm{Re}_{\mathrm{P}}^{0.5}\mathrm{Pr}_{\mathrm{g}}^{0.33}\right) \,. \tag{2.20}$$

Further information on the evaporation of droplets as well as additional correlations for the Nußelt number can be found in [16] and [42].

To conclude this section, the effects of turbulence in the continuous flow on the motion and evaporation of droplet are described briefly. As shown, droplet motion as well as heat and mass transfer between the droplet and the continuous phase are strongly influenced by the relative flow velocity between the droplet and its surroundings. However, as the flow field in gas turbine combustors is highly turbulent, strong fluctuations in u_{r} occur. According to Crowe [16] a relative turbulence intensity I_{r} is often used to describe the influences of flow turbulence on particles and droplets:

$$I_{\mathrm{r}} = \frac{\sqrt{u'^2}}{u_{\mathrm{r}}} \,. \tag{2.21}$$

This parameter relates the turbulent fluctuations in the gas phase (u') to the relative velocity between gas phase and particle (u_{r}). Generally it can be stated that turbulence in the main flow leads to an increase of the heat and mass transfer between the gas phase and the droplets [40]. A detailed analysis of the effects of turbulence on droplets can be found in literature [16, 33].

---

[3] $\mathrm{Pr}=(\eta_{\mathrm{g}} c_{\mathrm{p,g}})/\lambda_{\mathrm{g}}$.

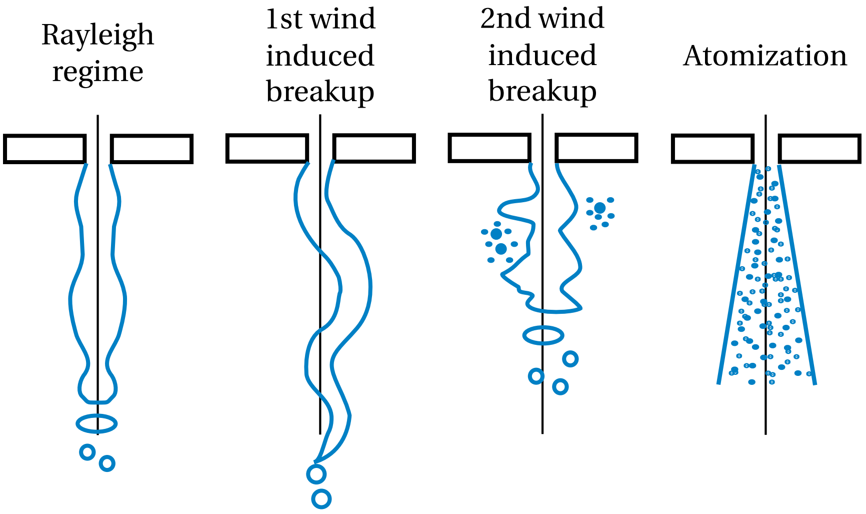

Figure 2.4: Primary atomization regimes of a single fluid nozzle according to Joos [33].

2.1.3 Atomization and Droplet Formation

In order to increase heat and mass transfer processes between liquid and gas phase, the surface to volume ratio of the liquid phase has to be increased by atomization. In technical applications a wide variety of different atomizer types exists. For combustion applications pressure atomizers and twin fluid atomizers are the two most common types. According to Lefebvre [42], the atomization process can be divided into two stages. In the primary atomization, large droplets are formed from a continuous liquid phase. Subsequently, these larger droplets are broken down into smaller droplets in the secondary atomization process.

For simple pressure atomizers, the primary atomization of the liquid is caused by turbulence in the liquid flow. Depending on pressure and the flow velocity of the liquid at the nozzle outlet $u_{\mathrm{l,out}}$, different regimes of jet breakup are found (see Fig. 2.4). At low liquid pressures the velocity of the liquid at the nozzle outlet $u_{\mathrm{l,out}}$ is small. Due to a low level of aerodynamic forces, the surface tension of the liquid jet is dominant in the Rayleigh regime. The surface tension has a stabilizing effect on the liquid jet and leads to the formation of big regularly sized droplets. At higher liquid pressures and higher jet velocities, breakup is influenced by instabilities of the liquid jet. These instabilites lead to a faster atomization. If the aerodynamic force on the jet is increased further, the influence of surface tension decreases and aerodynamic forces dominate the droplet formation. Due to the increasing turbulence in the jet, droplet size drops and jet breakup is moved closer to the outlet orifice. Finally, if the liquid pressure is even higher, the aerodynamic interaction of the liquid with the surrounding gas dominates the breakup process in the atomization regime. In this regime, jet breakup occurs directly at the nozzle outlet and the droplet sizes are significantly smaller than the diameter of the outlet orifice $d_{\mathrm{l,out}}$ [33]. Generally, atomization of liquid jets can be described with three non-dimensional parameters:

$$\text{Reynolds number: Re} = \frac{\text{inertial force}}{\text{viscous force}} = \frac{\rho_{\mathrm{l}} u_{\mathrm{l,out}} d_{\mathrm{l,out}}}{\eta_{\mathrm{l}}} = \frac{u_{\mathrm{l,out}} d_{\mathrm{l,out}}}{\nu_{\mathrm{l}}} \tag{2.22}$$

$$\text{Weber number: We} = \frac{\text{inertial force}}{\text{surface tension}} = \frac{\rho_{\mathrm{l}} u_{\mathrm{l,out}}^2 d_{\mathrm{l,out}}}{\sigma_{\mathrm{l}}} \tag{2.23}$$

$$\text{Ohnesorge number: Oh} = \frac{\eta_{\mathrm{l}}}{\sqrt{\sigma_{\mathrm{l}} \rho_{\mathrm{l}} d_{\mathrm{l,out}}}} \tag{2.24}$$

The Reynolds number describes the turbulence level in the flow while the Weber number relates the inertial forces in the fluid to the stabilizing forces in the droplet. In contrast to the Reynolds and Weber number the Ohnesorge number is solely dependent on material properties of the fluid as well as the geometry of the nozzle. Consequently, this number remains constant for a given combination of fluid and nozzle.

In contrast to pressure atomizers twin fluid atomizers do not require high liquid pressure for atomization and particularly exhibit technical advantages if liquid mass flow rates are low. These nozzles use the kinetic energy of a secondary air flow for the atomization process. Generally, two types of twin-fluid atomizers are know: air-assist and airblast atomizers [3]. While air-assist atomizers utilize a relatively low amount of high velocity air, airblast atomizers use a high amount of low velocity air for the atomization of the liquid. Due to the wide operational range of two-fluid atomizers a clear distinction between air-assist and airblast atomizers is often not possible. Nevertheless, depending on the exact nozzle configuration, empirical results for airblast atomizers can be transferred to air-assist atomizers and vice versa. As an air-assist noz-

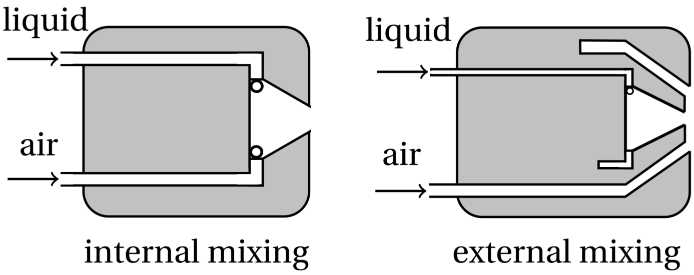

Figure 2.5: Different types of air-assist nozzles. Adapted from Lefebvre [43].

zle is used for the investigations in this thesis, the theoretical explanations are focused on this type of atomizer.

According to literature [42] two different types of air-assist atomizers exist: atomizers with internal mixing and atomizers with external mixing of the two fluids (see Fig. 2.5). In order to atomize high viscosity liquids internal mixing atomizers are used. In these atomizers complex interactions between fluid and air occur in an internal mixing chamber before the air-liquid mixture is released from the nozzle. For fluids with a relatively low viscosity like water, air-assist nozzles with external mixing are typically used. As shown in Fig. 2.5 high velocity air impinges at the liquid jet outside of the nozzle to achieve atomization. This mechanism of droplet formation relies mainly on the large velocity difference between the air and the liquid phase. Generally, the atomization process can be divided into 3 steps: At first, the large velocity difference between air and liquid flow induces aerodynamic forces at the surface of the liquid jet. Similar to the atomization process in pressure atomizers, instabilities in the liquid jet form. In a second step, strong shear forces at the surface of the liquid jet lead to the formation of small ligaments of the liquid. Finally, these ligaments are disintegrated via the Rayleigh mechanism, thereby forming droplets [47].

Many publications on air-assist nozzles focus on the prediction of the atomizer performance. As the aim of an atomizer is the production of droplets, the performance is typically determined in terms of droplet size. Various formulas are available to predict the Sauter mean diameter[4] produced by air-assist atomizers. Due to the complex interactions between air and liquid in air-assist

---

[4] The Sauter mean diameter will be explained later in this section (see Eq. 2.29).

nozzles, a derivation from first principles is often not possible. For this reason, various investigations focus on the determination of empirical formulas. Generally, the parameters influencing the performance of air-assist nozzles can be categorized into three different groups:

- Influences of the liquid properties ($\dot{m}_\mathrm{l}$, ν_l, σ_l, ...)
- Influences of the air properties ($\dot{m}_\mathrm{a}$, u_a, ...)
- Influences of the nozzle geometry ($d_\mathrm{l,out}$, $A_\mathrm{g,out}$[5], ...).

Similar to pressure nozzles, the surface tension σ_l and the viscosity ν_l of the liquid strongly influence the size of the droplets formed during the atomization. Additionally, Suyari and Lefebvre [77] report a strong influence of the relative velocity u_r between the air and the liquid flow on the Sauter mean diameter. Furthermore, several publications state the dominating influence of the gas to liquid ratio GLR on the atomizer performance [66, 84]:

$$\mathrm{GLR} = \frac{\dot{m}_\mathrm{g}}{\dot{m}_\mathrm{l}}. \tag{2.25}$$

In order to get an overview over the different parameters influencing the atomization in air-assist nozzles Lefebvre [42] and Liu [47] list multiple correlations for the Sauter mean diameter. Similar to pressure atomization, correlations based on non-dimensional numbers can be found [22]:

$$d_\mathrm{V,32} = 51 d_\mathrm{l,out} \mathrm{Re}^{-0.39} \mathrm{We}^{-0.18} \left(\frac{1}{GLR}\right)^{0.29} \tag{2.26}$$

In contrast to pressure atomization, the non-dimensional numbers in this formula are calculated using the relative velocity u_r instead of the liquid jet velocity u_l. However, the application of these different correlations is often limited to certain atomizers geometries or atomizing fluids. In order to find a correlation valid for the nozzle type used in this thesis, Waim [81] conducted an experimental study. He applied different empirical correlations to calculate the performance of the atomizer and compared the results to experimental measurements of the droplet size distributions. According to his investigations,

---

[5] $A_\mathrm{g,out}$ marks the outlet area of the atomizing air.

the correlation from Kim and Marshall [35] shows the most promising results in predicting the atomizer performance:

$$d_{\mathrm{V,32}} = 4.4488 \cdot 10^{-3} \frac{\sigma_{\mathrm{l}}^{0.41} \nu_{\mathrm{l}}^{0.32}}{(u_{\mathrm{r}}^{2} \rho_{\mathrm{g}})^{0.57} A_{\mathrm{g}}^{0.36} \rho_{\mathrm{l}}^{0.16}} + 2.8552 \cdot 10^{-3} \left(\frac{\nu_{\mathrm{l}}^{2}}{\rho_{\mathrm{l}} \sigma_{\mathrm{l}}} \right)^{0.17} \frac{1}{u_{\mathrm{r}}^{0.54}} \frac{1}{\mathrm{GLR}} \quad (2.27)$$

After the generation of droplets in the primary atomization regime, secondary atomization occurs. In the regime of the secondary atomization, droplets are broken down into smaller droplets and coalescence between droplets occurs. The mechanism of secondary atomization is dominated by different aerodynamic forces. Generally, the shape of a droplet depends on the forces acting on its surface. Aerodynamic forces have a disruptive influence on the droplet, while surface tension and viscous forces in the fluid have a stabilizing effect. In order to determine whether a droplet is stable or not, a force balance is set up for a droplet at rest [33].

$$F_{\mu} + F_{\sigma} = F_{\mathrm{A}}. \quad (2.28)$$

In this equation, F_{μ} describes the viscous forces in the fluid, F_{A} stands for the external aerodynamic forces and F_{σ} denotes the forces due to surface tension. While the aerodynamic forces depend on the properties of the surrounding flow and the relative flow speed between the droplet and the surrounding fluid, the stabilizing forces solely depend on the droplet diameter as well as material properties of the fluid. If the aerodynamic forces at a droplet exceed the stabilizing forces, the droplet is deformed and secondary atomization occurs. This process repeats until the droplets are small enough and the stabilizing forces are capable of balancing the destructive forces. Similar to the primary breakup, different regimes can be identified according to nondimensional parameters. In the secondary regime a Reynolds number $\mathrm{Re}_{\mathrm{gas}}$, a Weber number $\mathrm{We}_{\mathrm{gas}}$ and an Ohnesorge number $\mathrm{Oh}_{\mathrm{gas}}$ are introduced analogue to the primary regime. Due to the dominating influence of the aerodynamic forces, the relative velocity $u_{\mathrm{r}} = u_{\mathrm{g}} - u_{\mathrm{l}}$ between liquid and gas flow becomes the significant parameter when modeling secondary atomization. Consequently, u_{r} is used for the calculation of the nondimensional parameters. Additional information on the different mechanisms of secondary atomization can be found in literature [33].

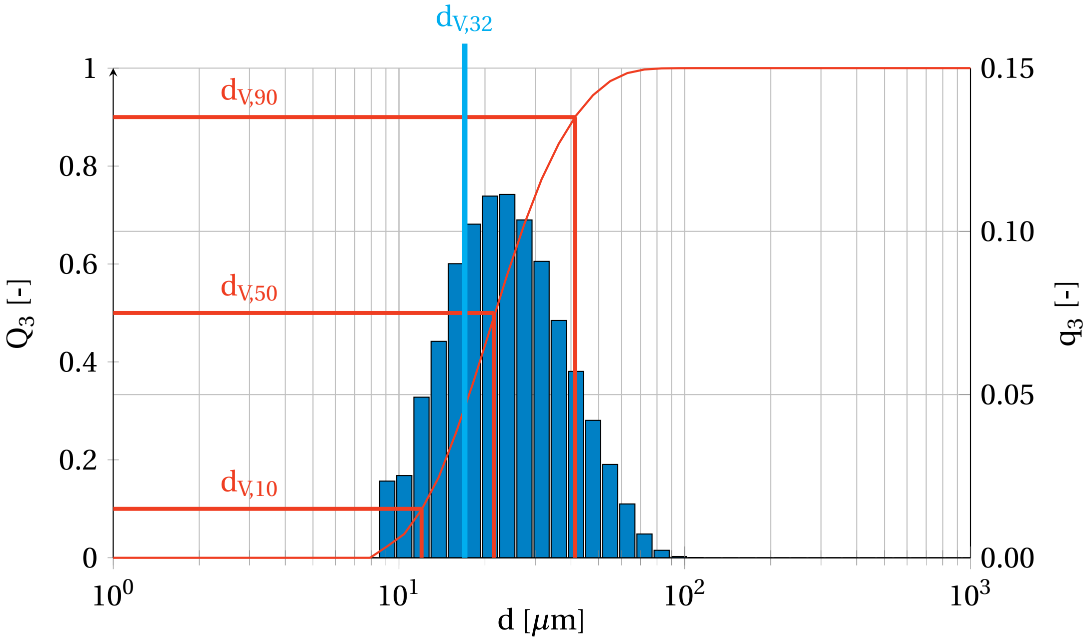

Figure 2.6: Example of a droplet size distribution with different representative diameters.

In general, technical sprays consist of droplets of different sizes. In order to describe these polydisperse sprays, droplet size distributions are introduced. Droplets are grouped into bins of a histogram according to their diameters.

Figure 2.6 shows an example of a typical droplet size distribution with discrete diameter ranges. The blue bars describe the volume fraction of the droplets over the droplet diameter, whereas the red line represents the cumulative droplet distribution. Furthermore, typical representative diameters are introduced in Fig. 2.6. These representative diameters can be used to quickly compare different droplet size distributions. The Sauter mean diameter (SMD) $\mathrm{d}_{\mathrm{V,32}}$ describes an equivalent diameter of a droplet with the same surface to volume ratio as the entire spray. It is therefore often used to characterize heat and mass transfer processes in particle flows. For spherical droplets the Sauter mean diameter can easily be calculated with the following formula [75]:

$$\mathrm{d}_{\mathrm{V,32}} = \frac{1}{\sum_{\mathrm{i}=1}^{\mathrm{N}} \frac{q_3(d_\mathrm{i})}{d_\mathrm{i}}}. \tag{2.29}$$

In this formula $\mathrm{q}_3(\mathrm{d}_\mathrm{i})$ describes the volumetric particle fraction of droplets grouped within the bin *i*.

The second representative diameter is equally important to describe the droplet size distribution. The $d_{V,90}$ is defined as the diameter that is larger than the diameter of 90 % of the droplets in the particle size distribution. It is therefore a good measure of the size of the biggest droplets in the size distribution. Similar to the Sauter diameter, it is often used in particle flows to characterize heat and mass transfer processes. In experimental investigations $d_{V,90}$ is extracted from the curve of the cumulative volume distribution where Q_3 equals 0.9.

2.2 Combustion

Starting from thermodynamics basics, this section presents fundamentals of premixed combustion processes. The concept of laminar premixed combustion is introduced followed by turbulent premixed combustion. Subsequently, turbulent premixed combustion in gas turbines is presented. Due to the high importance of pollutant formation in gas turbines, relevant pollutant formation pathways are discussed. The analysis focuses on the formation of CO and NO_x in premixed natural gas flames.

2.2.1 Classification of Combustion Processes

An exothermic redox reaction between fuel and oxidizer[6] molecules at high temperatures is called combustion. If the distribution of fuel and oxidizer in the reactant mixture is homogeneous, this combustion reaction is called premixed combustion [58]. An important parameter in combustion is the equivalence ratio Φ which describes the ratio of fuel and air in the reactant mixture (FAR) compared to a stoichiometric mixture (FAR_{st}):

---

[6] In technical applications oxygen is often used as oxidizer.

$$\Phi = \frac{\mathrm{FAR}}{\mathrm{FAR}_{\mathrm{st}}} = \frac{\frac{\dot{m}_{\mathrm{f}}}{\dot{m}_{\mathrm{a}}}}{\left(\frac{\dot{m}_{\mathrm{f}}}{\dot{m}_{\mathrm{a}}}\right)_{\mathrm{st}}} = \left(\frac{\dot{m}_{\mathrm{a,st}}}{\dot{m}_{\mathrm{a}}}\right)_{\dot{\mathrm{m}}_{\mathrm{f=const}}} \tag{2.30}$$

In combustion Φ is used to categorize different combustion regimes. This categorization is important as it allows to draw conclusions on flame temperatures as well as pollutant formation. Generally, three different regimes can be identified:

- Φ>1: This regime describes **rich** mixtures with a surplus of fuel. Due to the lack of oxidizer, complete combustion of the fuel is not possible.
- Φ=1: In **stoichiometric** mixtures, the amount of oxidizer in the reactant mixture is equal to the amount of oxidizer that is theoretically necessary for complete combustion.
- Φ<1: Mixtures with excess air are called **lean** mixtures. Due to the excess air in the reactant mixture the local flame temperatures drop which reduces the formation of nitrogen oxides in the flame.

Gas turbines are typically operated in the lean regime. Therefore, the following discussion focuses on the combustion of lean premixed mixtures of air and hydrocarbons. Although a multitude of different elementary reactions participate in this exothermic conversion, a global chemical reaction equation exists. For the complete combustion of hydrocarbon fuels this reaction equation reads as follows:

$$\begin{aligned} \mathrm{C_nH_m} + \left(n+\frac{m}{4}\right)\frac{1}{\Phi}\,\mathrm{O_2} + \frac{\gamma_{\mathrm{N2,a}}}{\gamma_{\mathrm{O2,a}}}\left(n+\frac{m}{4}\right)\frac{1}{\Phi}\,\mathrm{N_2} \\ \rightarrow n\,\mathrm{CO_2} + \frac{m}{2}\,\mathrm{H_2O} + \left(n+\frac{m}{4}\right)\left(\frac{1}{\Phi}-1\right)\,\mathrm{O_2} + \frac{\gamma_{\mathrm{N2,a}}}{\gamma_{\mathrm{O2,a}}}\left(n+\frac{m}{4}\right)\frac{1}{\Phi}\,\mathrm{N_2}. \end{aligned} \tag{2.31}$$

In this equation, $\gamma_{\mathrm{O2,a}}$ and $\gamma_{\mathrm{N2,a}}$ denote the volume fractions of oxygen and nitrogen in the combustion air. Typically, the volume fractions take values of $\gamma_{\mathrm{O2,a}}$=0.21 and $\gamma_{\mathrm{N2,a}}$=0.79.

2.2.2 Reaction Kinetics

In this section, the development of the species concentrations during the combustion reaction is described kinetically. Based on the chemical equations of the elementary reactions, the development of species concentrations over time can be calculated. The following chemical equation shows a typical bimolecular elementary reaction:

$$\mathrm{A} + \mathrm{B} \overset{k_{\mathrm{RR}}}{\rightarrow} \mathrm{C}\,. \tag{2.32}$$

In this reaction equation A, B and C denote chemical species while k_{RR} stands for the reaction rate constant. During the elementary reaction one molecule of species A reacts with one molecule of species B forming one molecule of species C. As two reactant molecules are involved in this reaction the molecularity of the reaction is two. Assuming a closed system with constant volume where only one chemical reaction takes place, the reaction rate is described by the following formula [33]:

$$v = -\frac{\mathrm{d}[A]}{\mathrm{d}t} = -\frac{\mathrm{d}[B]}{\mathrm{d}t} = k_{\mathrm{RR}} \cdot [A][B]\,. \tag{2.33}$$

The speed of this elementary reaction is dependent on the concentration of the molecules A and B as well as the reaction rate constant k. This reaction rate constant describes the influence of activation energy and reactant temperature on the reaction rate. Typically, an Arrhenius approach is chosen for the calculation [60]:

$$k_{\mathrm{RR}} = A \cdot T^{\beta} e^{\frac{-E_{\mathrm{A}}}{RT}} \tag{2.34}$$

Information about the collision frequency of the participating molecules is included in the pre-exponential factor A, while the dependency of the reaction rate on the mixture temperature is mainly described by the factor T^{β} and an exponential function [82]. According to collision theory, a chemical reaction takes place if two suitable molecules collide at a sufficiently high collision energy. The pre-exponential factor A calculates the frequency of successful molecule collisions in dependence of the size and weight of the molecules [55]. Information on the temperature dependence of the reaction rate is included in the exponential factor, which allows important conclusions on the reaction rate. Generally, an increase of the activation energy of the reaction slows down the reaction, while higher mixture temperatures lead to increasing reaction rates.

As combustion reactions typically consist of multiple elementary reactions, a global chemical reaction equation is introduced:

$$a\,\mathrm{A} + b\,\mathrm{B} \overset{k_\mathrm{glob}}{\rightarrow} p\,\mathrm{P} + q\,\mathrm{Q}\,. \tag{2.35}$$

The capital letters (A, B, P and Q) again denote chemical species, while the lowercase letters (a, b, p and q) stand for stoichiometric coefficients. k_glob stands for the reaction rate constant of the global reaction. According to Joos [33], the global reaction rate can be calculated with

$$v_\mathrm{glob} = -\frac{1}{a}\frac{\mathrm{d}[A]}{\mathrm{d}t} = -\frac{1}{b}\frac{\mathrm{d}[B]}{\mathrm{d}t} = k_\mathrm{glob}\cdot[A]^m[B]^n. \tag{2.36}$$

In this formula [A] and [B] denote concentrations of the reactants while m and n stand for experimentally determined exponents. k_glob marks the reaction rate constant of the global reaction. As the global reaction rate describes the behavior of the complete reaction system consisting of multiple elementary reactions, the exponents of the species concentrations do not match the stoichiometric coefficients shown in the global reaction equation[7] [33]. Similar to elementary reactions the reaction rate constant is calculated with an Arrhenius approach:

$$k_\mathrm{glob} = k_0\cdot e^{\frac{-E_\mathrm{A}}{RT}}\,. \tag{2.37}$$

However, in contrast to elementary reactions the pre-exponential factor as well as the activation energy are determined experimentally rather than through tabulated values. Nevertheless, similar to elementary reactions the global reaction rate shows a strong dependency on temperature. In order to describe the reaction speed of combustion reactions with hundreds of elementary reactions, the reaction speeds of all reactions have to be considered. This can be done with reaction mechanisms which include kinetic data for the elementary reactions [82]. With the help of an algebraic solver, it is possible to calculate the progress of combustion reactions. The accuracy of simulations strongly depends on the chosen reaction mechanism.

---

[7] This is an important difference to elementary reactions.

Besides the temporal development of the species concentrations, also the thermodynamic equilibrium of a reaction can be determined. This, in turn, allows to calculate the temperature of the reaction products. Assuming reaction at adiabatic conditions as well as chemical equilibrium of the reacting system, the temperature of the mixture is called adiabatic flame temperature $\mathrm{T_{ad}}$. Neglecting intermediate species of the chemical reaction[8] the adiabatic flame temperature can be calculated. According to the first law of thermodynamics, $\mathrm{T_{ad}}$ is determined with a stationary energy balance at the combustion chamber [40]:

$$\dot{Q} = \dot{H}_{\mathrm{Prod}} - \dot{H}_{\mathrm{Reac}} = \left(\dot{H} - \dot{H}^0\right)_{\mathrm{Prod}} + \Delta H_{\mathrm{R}}^0 - \left(\dot{H} - \dot{H}^0\right)_{\mathrm{Reac}} = 0 \tag{2.38}$$

ΔH_{R}^0 describes the enthalpy of reaction at reference conditions. It marks the difference in the chemically stored energy content between reactants and products. For a given composition of the reactant as well as the product mixture it can be calculated from tabulated values for the standard enthalpies of formation:

$$\Delta H_{\mathrm{R}}^0 = \dot{H}_{\mathrm{Prod}}^0 - \dot{H}_{\mathrm{Reac}}^0 = \left(\sum_{\mathrm{i=1}}^{\mathrm{Prod}} \dot{n}_{\mathrm{i}} h_{\mathrm{f,i}}^0\right) - \left(\sum_{\mathrm{i=1}}^{\mathrm{Reac}} \dot{n}_{\mathrm{i}} h_{\mathrm{f,i}}^0\right) \tag{2.39}$$

Assuming ideal gas behavior of the reactant and the product mixture, the missing terms in Eq. 2.38 can be calculated:

$$\left(\dot{H} - \dot{H}^0\right)_{\mathrm{Prod}} = \sum_{\mathrm{i=1}}^{\mathrm{Prod}} \dot{n}_{\mathrm{i}} \overline{c}_{\mathrm{p,i}}\big|_{\mathrm{T_{ref}}}^{\mathrm{T_i}} \cdot (T_{\mathrm{i}} - T_{\mathrm{ref}}) \tag{2.40}$$

$$\left(\dot{H} - \dot{H}^0\right)_{\mathrm{Reac}} = \sum_{\mathrm{i=1}}^{\mathrm{Reac}} \dot{n}_{\mathrm{i}} \overline{c}_{\mathrm{p,i}}\big|_{\mathrm{T_{ref}}}^{\mathrm{T_i}} \cdot (T_{\mathrm{i}} - T_{\mathrm{ref}}) \tag{2.41}$$

In these equations, $\overline{c}_{\mathrm{p,i}}|_{\mathrm{T_{ref}}}^{\mathrm{T_i}}$ describe the molar heat capacites of the components averaged over a given temperature range. These values are accessible via polynomials [49]. If the compositions of the reactants as well as the products are known, $\mathrm{T_{ad}}$ can be calculated with the following mathematical relation:

$$T_{\mathrm{ad}} = \frac{\sum_{\mathrm{i=1}}^{\mathrm{Reac}} \dot{n}_{\mathrm{i}} \overline{c}_{\mathrm{p,i}}\big|_{\mathrm{T_{ref}}}^{\mathrm{T_i}} (T_{\mathrm{i}} - T_{\mathrm{ref}}) - \Delta H_{\mathrm{R}}^0}{\sum_{\mathrm{i=1}}^{\mathrm{Prod}} \dot{n}_{\mathrm{i}} \overline{c}_{\mathrm{p,i}}\big|_{\mathrm{T_{ref}}}^{\mathrm{T_{ad}}}} + T_{\mathrm{ref}}. \tag{2.42}$$

---

[8] This assumption is justified at moderate flame temperatures.

A detailed derivation of Eq. 2.42 as well as an energy balance at operating conditions with water injection can be found in [40].

2.2.3 One-dimensional Laminar Premixed Flames

In the following, the concept of laminar premixed flames is introduced. Laminar flames have a characteristic structure shown in Fig. 2.7. Fresh gases enter from the left at a constant velocity u_u and a constant density ρ_u. The temperature of the reactants remains constant for a certain length, until it rises steeply at higher axial distances. Finally, products are leaving the domain on the right at an increased temperature. If the combustion reaction occurs in absence of heat losses, the temperature of the products equals the adiabatic flame temperature. As the temperature of the products is higher compared to the reactants, the density is reduced and the flow velocity increases according to mass conservation:

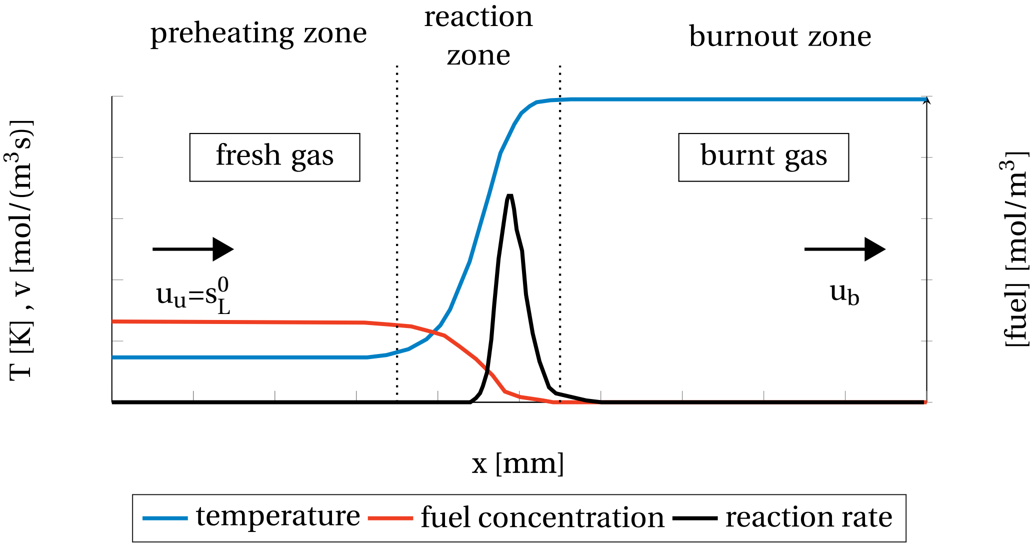

Figure 2.7: Typical structure of a laminar premixed flame. Adapted from [60].

$$\dot{m}_u = \rho_u A u_u = \rho_u A s_L^0 = \rho_b A u_b = \dot{m}_b. \tag{2.43}$$

The subscripts u and b describe properties of the unburnt and burnt mixture, respectively. An important measure for the reactivity of a reactant mixture is the laminar flame speed. The laminar flame speed s_L^0 equals the flow speed of the unburned mixture at the inlet of the domain if the flame is stabilized at a fixed position. Generally, s_L^0 describes the speed at which fresh gases are consumed in the laminar flame. It therefore is a measure of the reactivity of the reactants and, consequently, strongly influences macroscopic flame properties like lean blowout characteristics and flame stabilization.

As shown in Fig. 2.7, a laminar flame can be divided into three zones. The preheat zone, the reaction zone and the post flame zone [60]. In the preheat zone, the temperature of the reactants increases slowly due to thermal diffusion. As the temperature is low, chemical reaction rates are negligible. Subsequently, the fuel molecules are consumed in the reaction zone. The structure of this reaction zone can again be subdivided. At first, the temperature of the reactants rises due to heat conduction from the product zone. This, in turn, enhances the reaction rate in the reactant mixture which increases the temperature. In the inner layer of the reaction zone a self-enhancing mechanism leads to a fast consumption of the fuel molecules. The important chain branching reactions of the combustion process take place here [58]. The fuel consumption in the reaction zone is accompanied by a steep rise of temperature. More general, steep gradients of species concentrations as well as temperature are found. After the reaction zone, the product mixture flows into the post flame zone (also referred to as burnout zone). Intermediate products of the reaction are consumed and the chemical equilibrium is reached.

Besides the laminar flame speed, the thickness of the reaction zone (δ_f^0) is an important parameter to determine the reactivity of the reactant mixture. Compared to the preheating zone and the post flame zone, the thickness of the reaction zone is small. According to Poinsot [60], there are several definitions for δ_f^0. In this thesis the thermal thickness is used. Based on a temperature profile from one-dimensional calculations the flame thickness of premixed flames can be calculated according to the formula

$$\delta_\mathrm{f}^0 = \frac{T_\mathrm{b} - T_\mathrm{u}}{\left|\frac{\partial T}{\partial x}\right|_\mathrm{max}}. \tag{2.44}$$

In this equation, the temperature difference between products and fresh gases is divided by the maximum temperature gradient in the reaction zone. Addi-

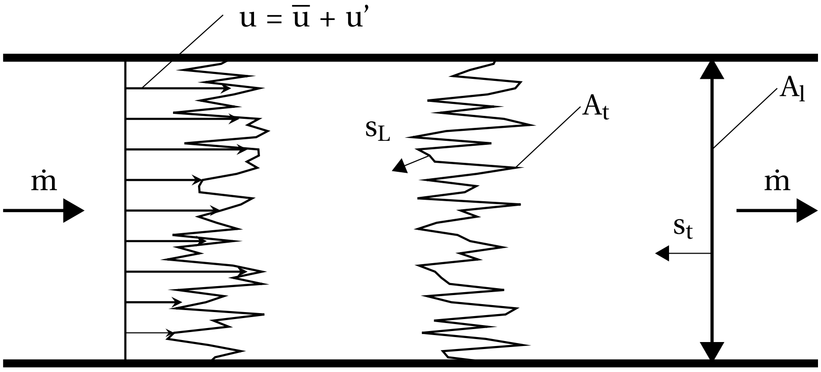

Figure 2.8: Typical structure of a turbulent premixed flame. Adapted from [58].

tionally, a chemical timescale τ_c for the reaction is introduced:

$$\tau_c = \frac{\delta_f^0}{s_L} \tag{2.45}$$

While 1-D laminar flames are a first step to describe premixed flames, they are not sufficient for the modeling of turbulent premixed combustion processes. Therefore, the modeling of turbulent premixed flames is described in the next section.

2.2.4 Modeling of Turbulent Premixed Flames

Based on the fundamentals of laminar flames, turbulent premixed flames are discussed in this section. If a combustion reaction takes place in a turbulent premixed flow, vortices in the reactant flow interact with the flame front and a turbulent flame front is generated. As both, combustion as well as turbulent flows exhibit a large range of different time and length scales, complex interactions of turbulence and combustion exist. Generally, the turbulence in the flow influences the laminar character of the flame front. As shown in Fig. 2.8, the turbulent eddies deform the planar flame front which leads to flame wrinkling and an increased flame surface A_t compared to the laminar case. As the surface of the flame front is increased, the speed of the combustion reaction is enhanced. In comparison to laminar flames, the use of turbulent flames allows to increase the power density in a given combustion chamber.

Consequently, the application of turbulent flames is widespread in technical combustion systems.

Similar to laminar flames, three different flame zones can be identified in a turbulent flame [60]. Ahead of the flame front fresh gases are flowing towards the flame. Subsequently, this preheating zone is followed by the reacting zone. Unlike for laminar flames, the flame is not stabilized at a certain location. Stochastically distributed turbulent eddies enter the reaction zone and lead to a thickening of the reaction zone. A turbulent flame brush with a turbulent flame thickness δ_t develops in time-averaged observation. The turbulent fluctuations of the flame front position lead to a probability distribution of the reaction dependent variables (reaction progress, temperature, species concentrations). Nevertheless, after the reaction is completed, convection transports the hot combustion products away from the flame front into the post-flame zone. Due to the reduced density of the post-flame mixture, the flow velocity increases.

In order to allow for easy calculation of turbulent premixed flames, the turbulent flame speed s_t is introduced. As shown in Fig. 2.8, this essential parameter of turbulent flames can be calculated based on the laminar flame speed s_L^0 and the flame surface at laminar conditions A_l

$$\frac{s_\mathrm{t}}{s_\mathrm{L}^0} = \frac{A_\mathrm{t}}{A_\mathrm{l}}. \tag{2.46}$$

In addition, multiple models are available to calculate s_t from s_L^0 and turbulence parameters. Based on the work of Damköhler, Peters [58] identified two different regimes of turbulent premixed combustion: the small scale and the large scale turbulence regime[9]. In the regime of large scale turbulence the interaction of the flame front and turbulence is purely kinematic [58]. Consequently, if the turbulent velocity fluctuations in the flow are small, the turbulent flow speed is proportional to u':

$$s_\mathrm{t} \approx u' \tag{2.47}$$

For higher velocity fluctuations the assumption of pure kinematic interaction

---

[9] Instead of small scale and large scale turbulence Damköhler identified the regimes of coarse-body turbulence and fine-body turbulence [18].

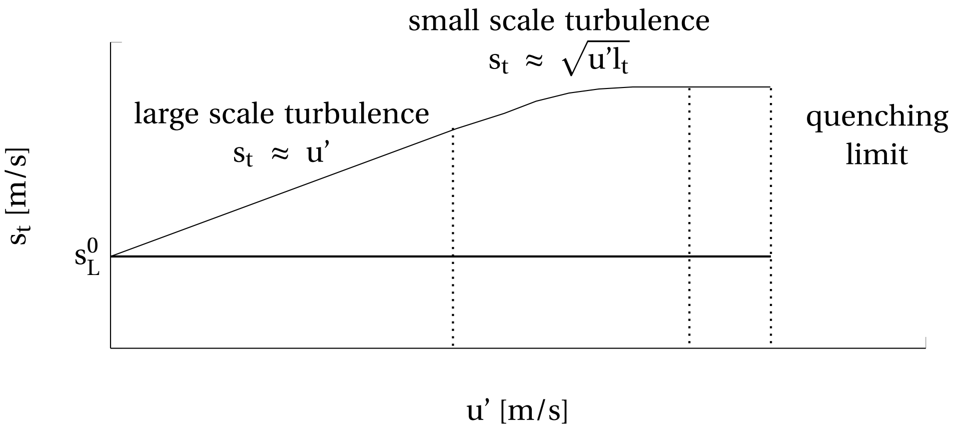

Figure 2.9: Influence of turbulence on the turbulent flame speed according to [60].

is not valid anymore. According to Damköhler the turbulent velocity fluctuations modify the transport between the reaction zone and the unburned gas [18]. In order to describe the influence of turbulence on the flame he introduced in the small scale regime he introduced a second proportionality:

$$s_t \approx \sqrt{u' l_t} \tag{2.48}$$

Figure 2.9 shows a typical development of s_t over u'. At low values of u' s_t increases linearly with the turbulent velocity fluctuations. This linear dependency of s_t on u' is known from the regime of large scale turbulence. However, as described by Damköhler the large scale turbulence regime is limited to low values of u'. In the regime of small scale turbulence at higher values of u' the curve in Fig. 2.9 starts to bend. At even higher values of u', s_t remains constant with rising velocity fluctuations. Finally, at very high turbulence levels, the quenching limit of the flame is reached and quenching occurs. For the calculation of the turbulent flame speed in this thesis, a correlation proposed by Peters [57] is chosen. In this correlation, the laminar flame speed is related to the turbulent flame speed using turbulence parameters as well as the flame thickness δ_f^0. Additionally, the formula of Peters combines the empirically determined proportionalities of the large scale as well as the small scale turbulence regime. Consequently, the formula can be used to calculate turbulent flame speeds for both combustion regimes as well as a wide range of u':

$$\frac{s_\mathrm{t}}{s_\mathrm{L}^0} = 1 - \alpha \frac{l_\mathrm{t}}{\delta_\mathrm{f}^0} + \sqrt{\left(\alpha \frac{l_\mathrm{t}}{\delta_\mathrm{f}^0}\right)^2 + 4\alpha \frac{u'}{s_\mathrm{L}^0} \frac{l_\mathrm{t}}{\delta_\mathrm{f}^0}}. \tag{2.49}$$

In this equation, α is an empirically determined coefficient with a value of 0.195. Detailed information on other correlations for the turbulent flame speed can be found in the work of Poinsot [60].

In order to model turbulent premixed combustion phenomena, detailed knowledge on time and length scales of turbulence and combustion reaction is required. Based on this information, non-dimensional numbers are determined and different combustion regimes can be identified. At first, the Schmidt number is introduced:

$$\mathrm{Sc} = \frac{\nu}{D}. \tag{2.50}$$

It describes the ratio of momentum diffusion and mass diffusion and is often used to describe phenomena with simultaneous mass and momentum transport processes. Furthermore, the flame thickness is described by:

$$\delta_\mathrm{f}^0 = \frac{D}{s_\mathrm{L}^0} \tag{2.51}$$

In order to classify the different flow regimes a turbulent Reynolds number is introduced. With the assumption of equal diffusivities (Schmidt number Sc=1) as well as the definition of the flame thickness, Re_t is based solely on properties of the turbulent flow:

$$\mathrm{Re}_\mathrm{t} = \frac{u' l_\mathrm{t}}{\nu} \overset{\mathrm{Sc}=1}{=} \frac{u' l_\mathrm{t}}{D} \overset{\delta_\mathrm{f}^0}{=} \left(\frac{u'}{s_\mathrm{L}^0}\right)\left(\frac{l_\mathrm{t}}{\delta_\mathrm{f}^0}\right). \tag{2.52}$$

Furthermore, Peters [58] introduced two non-dimensional numbers to identify the dominating processes in the reacting flow. The Damköhler number Da correlates the chemical timescale of the reaction to the turbulent timescale of the biggest eddies in the turbulent flow. It is defined according to

$$\mathrm{Da} = \mathrm{Da}(l_\mathrm{t}) = \frac{\tau_\mathrm{t}}{\tau_\mathrm{c}} = \frac{l_\mathrm{t}/u'(l_\mathrm{t})}{\delta_\mathrm{f}^0/s_\mathrm{L}^0}. \tag{2.53}$$

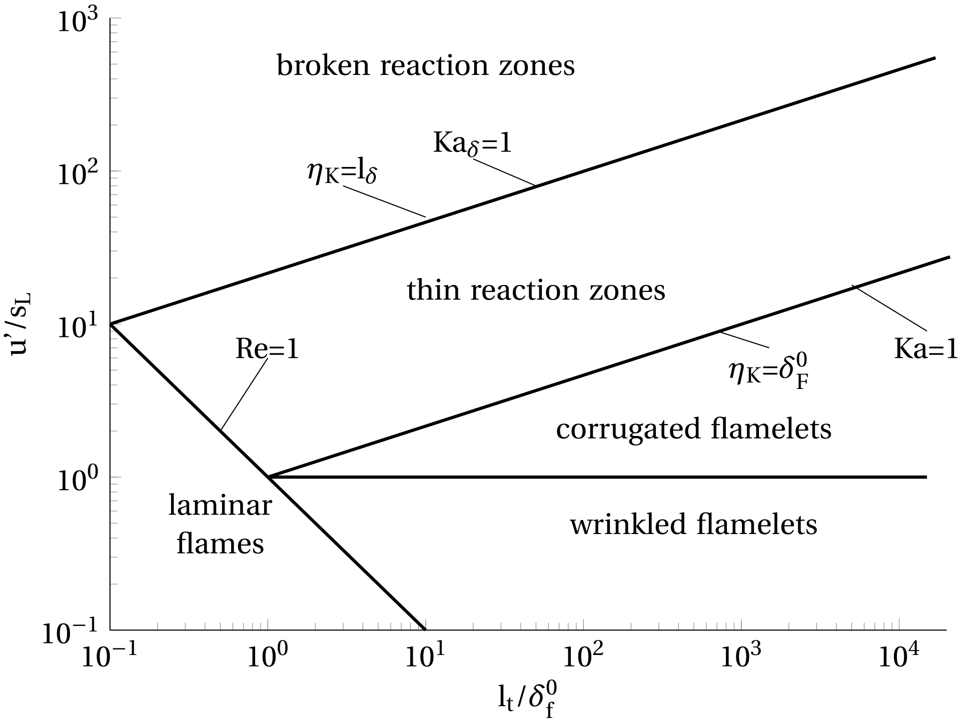

Figure 2.10: Borghi diagramm for the classification of turbulent flames according to Peters [58].

In an analogue manner, a non-dimensional Karlovitz number is introduced for the smallest (Kolmogorov) scales in the flow:

$$\mathrm{Ka} = \frac{1}{\mathrm{Da}(\eta_\mathrm{k})} = \frac{\tau_\mathrm{c}}{\tau_\mathrm{k}} = \frac{u'(\eta_\mathrm{k})/\eta_\mathrm{k}}{s_\mathrm{L}^0/\delta_\mathrm{f}^0}. \tag{2.54}$$

According to Borghi [8], these non-dimensional numbers can be used to classify turbulent premixed flames in a Borghi diagram (Fig. 2.10). Five different regimes of turbulent premixed flames can be identified:

- **Laminar flames**: In this regime, the flow is laminar and the turbulent Reynolds number is below unity. As described in section 2.2.3, a laminar flame develops. The flame speed equals s_L^0.
- **Wrinkled flamelets**: The turbulent fluctuations in the flow are small compared to s_L^0. In this regime, the characteristic time scale of the reaction lies below the time scale of the smallest eddies in the flow. As the

result, the complete flame structure is embedded within the smallest eddies of the Kolmogorov scale η_k [58] and the Karlovitz number is below unity. Consequently, turbulent eddies can't enter the reaction zone of the flame and the influence of turbulence on the flame is limited to wrinkling of the flame surface. According to the diagram in Fig. 2.9, the flame speed increases linearly with u' in this regime.

- **Corrugated flamelets**: If the turbulent velocity fluctuations u' exceed s_L^0, the influence of turbulence on the flame front rises. Due to the higher level of turbulence, the wrinkling of the flame front increases. Nevertheless, turbulent eddies can't enter the reaction zone and a quasi-laminar flame structure persists. Due to the intense deformation of the flame front, pockets of fresh gas or burnt gas are formed and interactions between the different flame fronts become possible. In the theory of Damköhler [18], this regime corresponds to the regime of coarse-body turbulence (large scale turbulence). Similar to the wrinkled flame regime, s_t increases linearly with u'.

- **Thin reaction zones**: The regime of thin reaction zones lies between the border of Ka = 1 and Ka = 100. In the theory of Damköhler [18], this regime corresponds to the regime of fine-body turbulence (small scale turbulence). This means, that small turbulent eddies can enter the reaction zone, however, the size of the eddies is too big to enter the inner layer where the important chain branching reactions take place [58]. This leads to intense interactions of turbulence with the flame front, however, local quenching of the flame due to turbulent fluctuations is prevented. Consequently, this regime is suitable for the application in technical combustion systems. In terms of flame speed, the linear dependency of s_t on u' breaks down. Due to the smaller scales of the turbulent fluctuations compared to the other regimes, the flamelet structure of the flame front is disturbed. In Fig. 2.9 this leads to a reduction of the slope of the curve towards zero.

- **Broken reaction zones**: If the Karlovitz number rises above 100, the smallest turbulent eddies can enter the inner layer of the reaction zone. Consequently, the flamelet structure of the flame front is disrupted which results in local extinguishing phenomena and broken reaction zones. This, in turn, allows fresh gases to diffuse to the product side. In the regime of broken reaction zones, s_t remains constant with rising u’ until the quenching limit is reached (see Fig. 2.9).

For many technical applications requiring high power density, the regime of thin reaction zones is favorable: Due to the strong influence of turbulence, the flame speed is much higher than in a laminar flame. At the same time the flamelet structure of the flame front is still present and local quenching phenomena are prevented which safeguards stable operation of the flame.

2.2.5 Pollutant Formation in Premixed Flames

Due to stringent environmental regulations, pollutant formation is a key issue in technical combustion systems. This section gives basic information on NO_x and CO formation.

2.2.5.1 NO_x Formation

Nitrogen oxides are a main source of air pollution and acid rain [79]. Due to its various negative influences on the environment, the emission of nitrogen oxides is limited by stringent boundaries. Unfortunately, nitrogen oxides are formed from oxygen and nitrogen in the combustion air during combustion. Apart from NO_x produced from fuel-bound nitrogen, four mechanisms of NO_x formation are known:

- Thermal NO mechanism (Zeldovich)
- Prompt NO mechanism (Fenimore)
- N_2O-mechanism
- NNH-mechanism

The contributions of NO formed via each mechanism strongly depend on the operating conditions of the combustor. Furthermore, the different timescales of the reactions have to be taken into account when analyzing the NO_x formation in combustors. Gas turbine combustor residence times are at least by one order of magnitude smaller than the time required for reaching equilibrium of NO_x formation. This means, that the equilibrium concentration is not reached in technical combustion systems. Therefore, NO_x formation is strongly influenced by reaction kinetics in the flame and in the post-flame zone. In the following, the reaction kinetics of different NO_x formation mechanisms are presented and influencing parameters are discussed:

- **Thermal NO mechanism**: The thermal mechanism, discovered by Zeldovich [85], consists of 3 elementary reactions:

  $$O + N_2 \rightleftharpoons NO + N \tag{2.55}$$

  $$N + O_2 \rightleftharpoons NO + O \tag{2.56}$$

  $$N + OH \rightleftharpoons NO + H. \tag{2.57}$$

  In the first elementary reaction the triple-bond of a nitrogen molecule is split using high amounts of energy. Consequently, a high activation energy of 318 kJ/mol is required which makes this step rate determining for the whole mechanism. Besides the mixture temperature, the reaction rate of NO formation is dependent on the concentrations of the oxygen radical as well as nitrogen [33]. While nitrogen is readily available throughout the flame, the concentration of the O radical strongly depends on the position in the flame. In the post flame zone the concentration of the oxygen radical takes a stable equilibrium value. However, in the reaction zone the concentration of the O radical is significantly higher compared to the equilibrium value which leads to considerably enhanced NO formation rates there. Generally, thermal NO is formed predominantely in the lean and near-stoichometric combustion regime [43] at high residence times and temperatures above 1700 K [82].

- **Prompt NO mechanism**: The mechanism of prompt NO is closely linked to the occurrence of CH radicals and therefore to the combustion of hydrocarbon fuels. Under fuel rich conditions, the concentration of CH radicals in the flame rises which promotes the NO formation via this mechanism. Consequently, prompt NO dominates at fuel-rich operating conditions [82]. The mechanism consists of various elementary reactions while the rate determining step originates from the elementary reaction [33]:

$$\mathrm{CH} + \mathrm{N_2} \rightleftharpoons \mathrm{HCN} + \mathrm{N}. \tag{2.58}$$

In this first step, HCN is formed from CH radicals and nitrogen molecules. Subsequently, multiple steps form NO from these intermediate products. As high concentrations of the CH radicals are found only in the reaction zone, NO formation via the prompt mechanism takes place there. Unlike in the Zeldovich mechanism, the typical reaction times of the NO formation are low and only a minor influence of the residence time is found.

- **N_2O-mechanism**: The N_2O-mechanism occurs at very lean operating conditions and low temperatures [33]. As the NO formation from other mechanisms is low at these conditions, the N_2O-mechanism is dominating. Similar to NO formation over the thermal route, the N_2O mechanism produces NO from oxygen radicals and nitrogen in the combustion air. However, as a difference, a third reaction partner is needed for the first elementary reaction (third body reaction).

$$\mathrm{O} + \mathrm{N_2} + \mathrm{M} \rightleftharpoons \mathrm{N_2O} + \mathrm{M} \tag{2.59}$$
$$\mathrm{H} + \mathrm{N_2O} \rightleftharpoons \mathrm{NO} + \mathrm{NH} \tag{2.60}$$
$$\mathrm{O} + \mathrm{N_2O} \rightleftharpoons \mathrm{NO} + \mathrm{NO} \tag{2.61}$$

In the first step, N_2O is formed as an intermediate product. The following two elementary reactions form NO from N_2O and radicals present in the flame. Due to the dependence on a collision partner in the first reaction, the NO production from the N_2O-mechanism rises with pressure.

- **NNH-mechanism**: The contribution of the NNH mechanism to NO production is usually small under technical relevant conditions. Similar to the N_2O-mechanism, an intermediate product (NNH) is formed first from nitrogen molecules and radicals in the flame. In a second oxidation step, NNH is then transformed to NO molecules.

$$NNH + O \rightleftharpoons NO + NH \tag{2.62}$$

Under certain conditions also nitrogen dioxide (NO_2) can be generated in flames. While NO is mainly found at high temperature conditions, a significant amount of NO is converted to NO_2 at lower temperatures. At ambient conditions, an equilibrium between NO and NO_2 forms. NO_2 is formed from NO in the following elementary reaction:

$$NO + HO_2 \rightleftharpoons NO_2 + OH \tag{2.63}$$

At typical operating conditions of gas turbines with premixed combustion, NO_2 emissions are low or even negligible, because NO concentrations are low. In addition, the flame temperatures are too high for the shift reaction from NO to NO_2 at higher loads.

In order to eliminate the influence of dilution, the NO_x concentrations are typically normalized to 15 vol-% oxygen in the exhaust gas. This normalization of the data allows to compare emission levels of measured an calculated NO_x values. A calculation rule for normalization of NO and NO_2 measurements is described by Ahrens [1].

2.2.5.2 CO Formation

Another pollutant with detrimental influence on the environment is carbon monoxide. CO is formed as an intermediate during the combustion of hydrocarbons. However, significant amounts are released mainly due to incomplete combustion. The combustion of hydrocarbons can be divided into two separate steps. In the first step, the hydrocarbon molecules are broken down and CO forms. As fuel consumption occurs very fast within the flame, high concentrations of CO are found in the reaction zone. Subsequently, CO is oxidized to carbon dioxide in the CO burnout zone which typically reduces the CO concentration by several orders of magnitude. The CO burnout is a mechanism

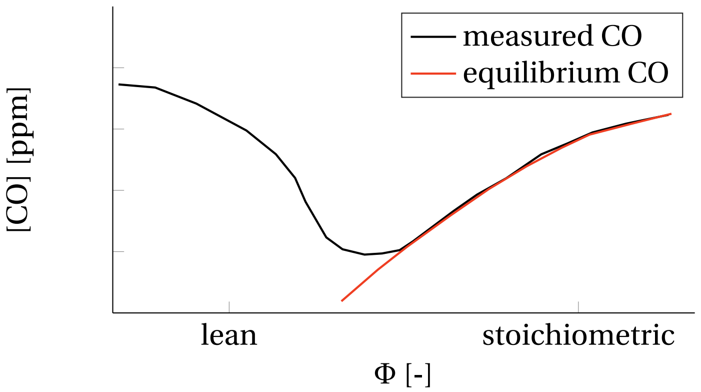

Figure 2.11: CO emissions of a gas turbine at different operating conditions. Adapted from [33].

based on radicals. Although multiple elementary reactions participate in the reaction chain, CO is only consumed in the reaction [79]

$$CO + OH \rightleftharpoons CO_2 + H\,. \tag{2.64}$$

In this reaction, the concentrations of CO and the OH radical as well as the temperature of the mixture play an important role. Besides CO formation and oxidation at adiabatic premixed conditions further aspects have to be considered in real gas turbine engines. Figure 2.11 shows the CO emissions of a gas turbine over the equivalence ratio. Above a certain threshold value in the lean regime the measured CO values match the calculated equilibrium CO values. Due to the high flame temperatures CO is effectively oxidized. With decreasing Φ and decreasing temperature, the equilibrium CO value drops and the measurements follow this trend. However, if the equivalence ratio is decreased further, the measured CO concentrations begin to deviate from the equilibrium values. Due to the lower temperatures, the reaction rate of the burnout reaction becomes too low and the timescales of the CO burnout increase above typical combustor residence times. Consequently, the equilibrium value can not be reached within the combustion chamber and higher values are measured. Further deviations of the measured values from the CO equilibrium arise from quenching phenomena in the combustor. Quenching describes local extinction phenomena in the flame due to various influences. Typical reasons for quenching in industrial combustion chambers are flame stretch, heat losses at cold combustor walls or the introduction of cold gases. If chemical reaction is disturbed by these effects, CO burnout breaks down which results in higher CO emissions at the combustor outlet.

Like NO_x concentrations, the CO values are normalized to 15 vol-% oxygen in the exhaust gas according to the procedure presented in [1].

3 Basics of Water Injection in Gas Turbines

This chapter describes the effects of water injection on gas turbine combustion. First, the effects of water injection on the power output of modern gas turbines are clarified with the help of a generic gas turbine simulation tool. Literature data is used to support these findings and help to identify possible problems of water injection in turbomachinery. Subsequently, the influence of water injection on the flame behavior and the mixture reactivity is discussed. Finally, the influence of water addition on the pollutant formation is shown.

3.1 Water Injection for Power Augmentation

From early examples in the field of aircraft propulsion [17] up to modern gas turbine processes like the Cheng cycle [14], water and steam injection have been used to increase the power output of gas turbine engines. Many different gas turbine cycles with water or steam injection are known (see [32]). In all cycles, the effects of water injection on the power output are similar. According to Kail [34], the influence of water addition on the power output of the engine can be attributed to two phenomena. On the one hand, the mass flow in the turbine increases due to water addition. Assuming a constant power demand of the compressor section and a negligible power consumption for the compression of the liquid water, the net power output of the gas turbine can be increased. On the other hand, the temperature as well as the heat capacity of the burnt gas at the turbine inlet are changed. This, in turn, also influences the power output of the engine [40]. Depending on the exact operating conditions of the machine, either of the two effects is dominating. To exploit the full potential of power augmentation due to water injection, additional fuel can be added compared to dry operation. This is done in order to compensate the temperature drop related to the water addition (see section 3.2) and to maintain a stable level of T_{ad}.

This section seeks to clarify the influence of water addition on the power output of gas turbines. A Matlab tool, based on analytical equations as well as gas turbine performance maps, is used to estimate the power output and the engine efficiency for a wide range of different operating conditions. In order to determine the effects of water or steam injection on the power output, a basic water and steam injection system is implemented. At first, an overview over the investigated gas turbine system is given. In a second step, the calculation procedure for the performance data is shown.

3.1.1 Setup and Calculation Procedure of the Gas Turbine Simulator

In the thermodynamic analysis, a standalone gas turbine system with water or steam injection is investigated. Figure 3.1 shows a simplified schematic drawing of the system.

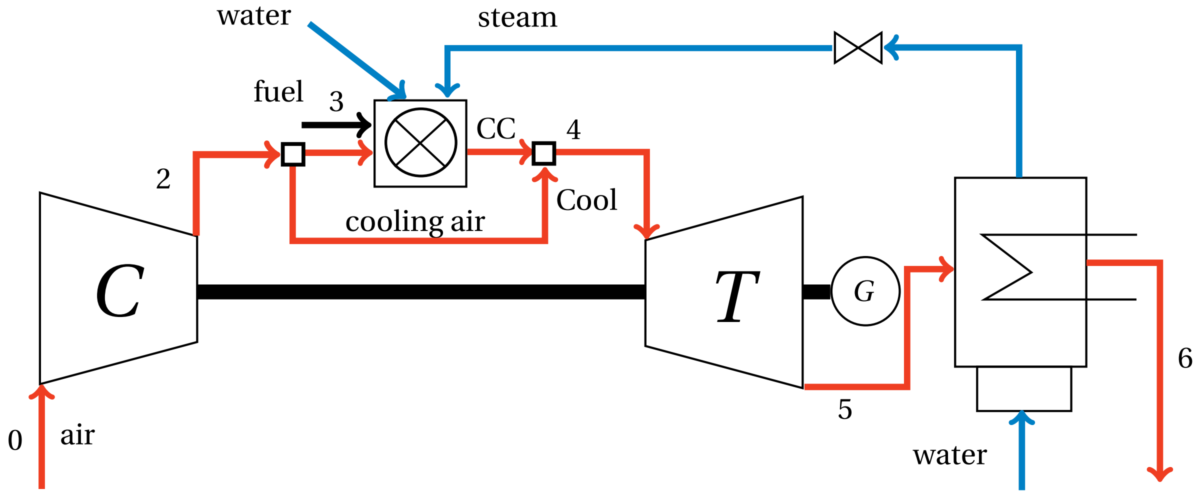

Figure 3.1: Schematic of the investigated standalone gas turbine configuration.

At first, ambient air is compressed in a polytropic compressor (C). The main air flow enters the combustion chamber whereas a small share of compressed air is used for the cooling of the combustion liner as well as the high pressure turbine. In the combustion chamber natural gas is burned with air and liquid water or steam according to the given input values. This raises the temperature of the product mixture. Subsequently, the hot exhaust gas mixture is expanded in the turbine section (T) before heat is extracted in the heat recovery steam generator (HRSG). The power from the turbine is extracted with an electrical generator (G). In the HRSG, liquid water is preheated, evaporated and super-heated at high pressures. For operating points with steam injection, a throttle valve reduces the pressure in the super-heated steam before it enters the combustion chamber.

Generally, water or steam addition in the combustion chamber increases the mass flow rate in the turbine section. As the result, the pressure at the turbine inlet rises [83]. Since the pressure level at the turbine inlet is higher compared to dry operation, the pressure in the combustion chamber and at the compressor outlet has to be higher as well. This strongly affects the operation of the compressor. Due to the increased backpressure, the air flow in the compressor drops and a new stable operating point establishes [10]. However, because of the complexity of modern turbomachinery the envelope of possible stable operating points is limited. According to Wasicek [83], the limiting scenario for the addition of water is the exceeding of the compressor's surge limit. If the pressure at the compressor outlet is too high, compressor surge occurs. The flow direction in the compressor reverses and stable operation of the compressor is not possible anymore.

In order to model the different effects of water injection on the performance of gas turbines, an iterative calculation process is implemented in the simulation tool. A flowchart describing the calculation process is shown in Fig. 3.2. In order to assess the influence of water addition on the performance on the different components of the gas turbine, all calculations are related to a fixed reference point at dry operating conditions (index *dry*). Starting from this operating point, water is injected and its impact on the performance of the system is determined.

Based on the thermodynamic state of the ambient air the state of the compressed air is calculated. The mass flow rate of ambient air is taken as initial

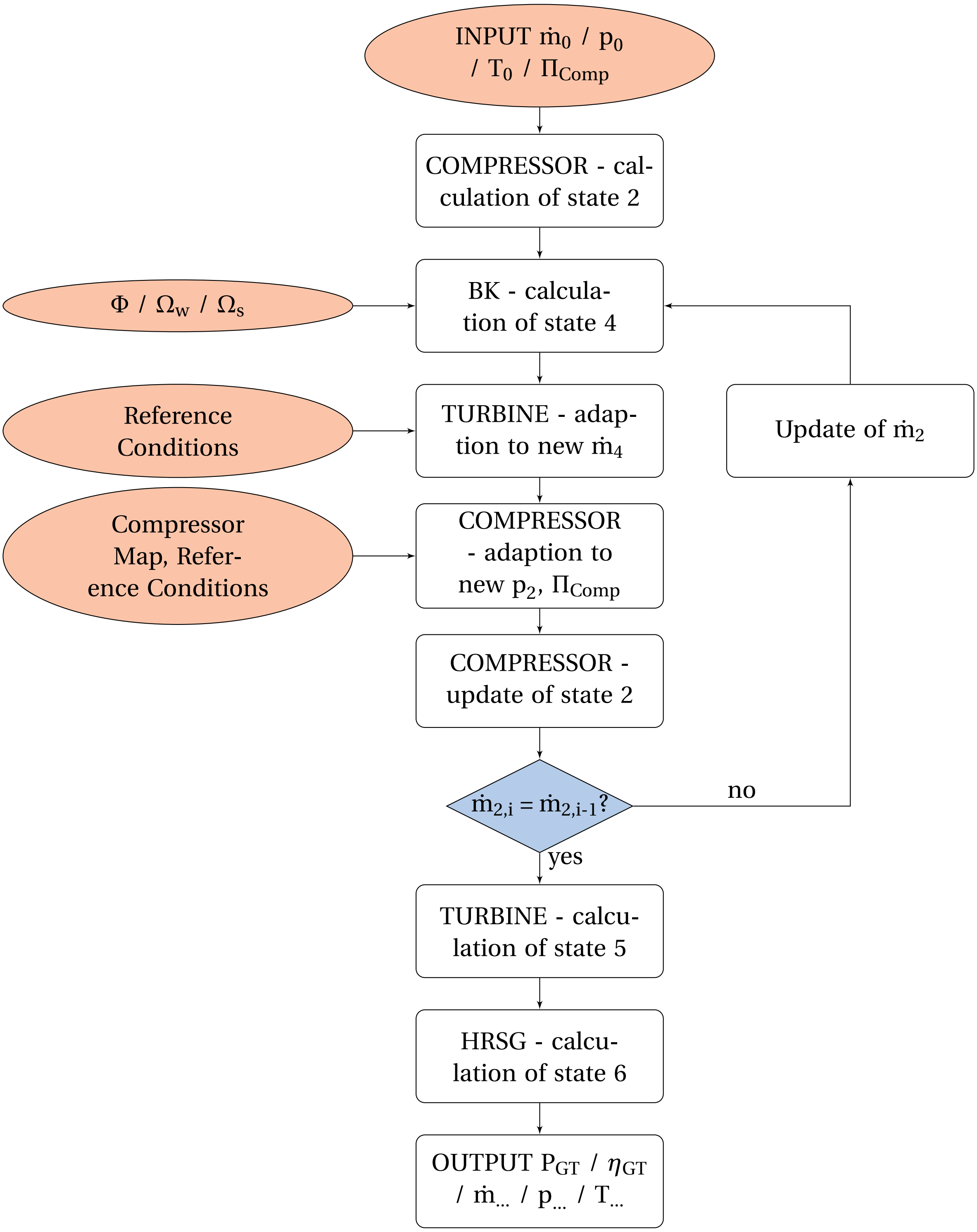

Figure 3.2: Flowchart of the gas turbine performance simulation.

value for the calculation of the combustion process. Afterwards, the condition at the outlet of the combustion chamber is determined based on equivalence ratio and water to fuel ratio. Due to the increased mass flow rate in the turbine at water injected conditions, a new operating point of the turbine establishes. The changing operating point of the turbine alters the pressure in the combustion chamber and the operating point of the compressor as well. Therefore, an updated operating point of the compressor is calculated in the next step. Due to the update of the compressor operating point, the mass flow rate in the engine changes. As a consequence, the new operating point of the gas turbine has to be determined iteratively. Once a new stable operating point is found, power output and efficiency of the gas turbine are calculated. In the following sections, the modeling of the components of the gas turbine simulator are described in more detail.

3.1.1.1 Modeling of the Compressor

In order to keep the simulation as realistic as possible, experimentally determined compressor performance maps are utilized. The compressor performance map used for the simulations in this thesis originates from a GT13E2 gas turbine from Alstom Power [83]. Figure 3.3 shows the performance map in non-dimensional notation. Lines for different reduced rotation speeds are shown in red, while the surge limit is marked with a black line. Furthermore, the design point of the compressor is highlighted in the non-dimensional graph. Due to the universal design of the gas turbine simulator, it is possible to use different performance maps, too. With the use of different performance maps, the operational characteristics of the compressor can easily be adapted to different machine characteristics. Besides this, the non-dimensional specification of the compressor map has another advantage. Multiplication of the performance maps with reference conditions for different mass flow rates allows to scale the operating range of the compressor to different mass flow rates. Therefore, in order to calculate the updated operating point of the compressor, reference conditions ($m_{0,\mathrm{dry}}$, $R_{0,\mathrm{dry}}$, $T_{0,\mathrm{dry}}$ and $p_{0,\mathrm{dry}}$) have to be specified first. For all calculations in this thesis, a design point at dry conditions is chosen as reference.

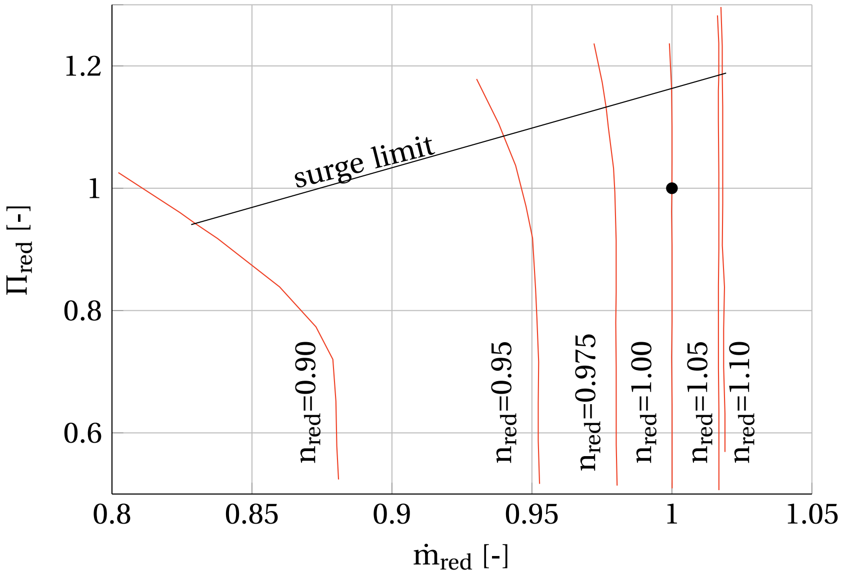

Figure 3.3: Compressor map used in the gas turbine simulator. Adapted from Wasicek [83].

For the calculation of a new operating point, the following steps are taken. Due to the water injection in the combustor, the pressure p_2 at the compressor outlet changes. Given constant ambient conditions, this changes Π_{red}:

$$\Pi_{red} = \frac{p_2/p_0}{p_{2,dry}/p_{0,dry}} \tag{3.1}$$

Furthermore, depending on the updated operating point as well as the reference conditions, the reduced rotation speed of the compressor changes according to the following formula:

$$n_{red} = \frac{n}{n_{dry}} \sqrt{\frac{R_{0,dry}\,T_{0,dry}}{R_0\,T_0}}. \tag{3.2}$$

However, due to the constant grid frequency, the absolute rotation speed of the engine can not change. This value is fixed to 50 Hz. In the next step, the new value of the reduced mass flow rate in the compressor is extracted from the scaled compressor performance map. As Π_{red} and n_{red} are known, $\dot{m}_{red}$ can be extracted from Fig. 3.3.

In order to prevent compressor surge, the compressor surge margin is evaluated for all operating points. The surge margin describes the distance of an operating point to the surge line in the compressor map. According to Lechner [40] the surge margin of a compressor can be calculated with

$$\mathrm{SM}_{\mathrm{Comp}} = \left| \frac{\Pi_{\mathrm{Comp,Surge}} - \Pi_{\mathrm{Comp}}}{\Pi_{\mathrm{Comp}}} \right|_{\mathrm{n_{red}=const.}} . \tag{3.3}$$

At constant reduced rotational speed of the compressor, this equation compares the pressure ratio at a given operating point (Π_{Comp}) to the pressure ratio at an operating point where compressor surge occurs ($\Pi_{\mathrm{Comp,Surge}}$). In order to obtain a relative measure for the compressor stability the difference of these two values is normalized with Π_{Comp}. For typical compressors used in modern gas turbines the surge margin at the design point of the engine lies at around 20%. However, depending on the exact operating point, the surge margin can be significantly lower. If the surge margin of the compressor falls below a critical value $\mathrm{SM}_{\mathrm{Comp,crit}}$, stable operation of the compressor is not possible with sufficient reliability. Consequently, operation of the compressor at these operating points is not allowed. Similar to industrial gas turbines a critical compressor surge margin of 5% is used for the calculations in this thesis. If the surge margin of the new operating point is larger than the critical surge margin, a new stable operating point is found. Finally, the updated mass flow rate $\dot{m}_0$ in the compressor can be calculated with the following formula:

$$\dot{m}_{\mathrm{red}} = \frac{\dot{m}_0}{\dot{m}_{0,\mathrm{dry}}} \sqrt{\frac{R_0 T_0}{R_{0,\mathrm{dry}} T_{0,\mathrm{dry}}}} \frac{p_{0,\mathrm{dry}}}{p_0} . \tag{3.4}$$

In this equation, the subscript *dry* denotes values at dry reference conditions.

In order to consider losses in the compressor, a polytropic efficiency of the compression is introduced. As the changes in the operating point of the compressor are relatively small, a constant value of $\eta_{\mathrm{Comp,pol}}$=0.92 is used for all calculations in this thesis [71]. Finally, the power consumption of the compressor can be calculated:

$$P_{\text{Comp}} = \dot{m}_2 \int_0^2 c_\text{p}(T)dT \tag{3.5}$$

$$= \dot{m}_2 \left(\overline{c}_\text{p}|_{\text{T}_\text{ref}}^{\text{T}_2} (T_2 - T_\text{ref}) - \overline{c}_\text{p}|_{\text{T}_\text{ref}}^{\text{T}_0} (T_0 - T_\text{ref}) \right), \tag{3.6}$$

$$T_2 = T_0 \Pi_{\text{Comp}}^{\frac{n-1}{n}}, \tag{3.7}$$

$$\frac{n-1}{n} = \frac{\kappa - 1}{\kappa} \frac{1}{\eta_{\text{Comp,pol}}}. \tag{3.8}$$

3.1.1.2 Modeling of the Combustion Chamber

This section describes the modeling of the combustion chamber as well as the determination of the operating conditions at the turbine inlet. As described above, the air mass flow at the compressor outlet is divided into two parts: combustion air and cooling air used for the cooling of the high pressure turbine and the combustion liner. In order to allow realistic estimations of the gas turbine performance, the shares of cooling air and combustion air should be similar to values in typical modern gas turbines. According to considerations from Seydel [71], the mass flow ratio between the cooling air and the air flow in the compressor is set to

$$\frac{\dot{m}_{\text{Cool}}}{\dot{m}_2} = 0.23 \,. \tag{3.9}$$

This cooling air ratio is used for all calculations presented in this thesis.

While the main part of the high pressure air from the compressor enters the combustion chamber, cooling air does not participate in the combustion reaction. Consequently, only 77% of the compressor air mass flow rate can be used for fuel oxidation in the combustion chamber. The modeling of the combustion chamber is based on a stationary energy balance at the combustor. For all simulations in this thesis, adiabatic operation of the combustion chamber is assumed. The formulas for the calculation are presented in section 2.2.2. The implemented model is capable of calculating different combustion reactions with natural gas, air, water and steam. Based on Φ, Ω_S and Ω_W[1] as well as

---

[1] Ω_S and Ω_W denote the steam to fuel ratio and the water to fuel ratio, respectively. Ω is defined according to section 4.1.3.

the inlet conditions of the compressed air, the mass flow rate at the outlet as well as the adiabatic flame temperature are calculated. The calculation of the adiabatic flame temperature is an iterative process, as the heat capacities of the products are dependent on the temperature of the products. This iterative dependency is taken into account in the calculation.

In order to consider the cooling air flows in the combustion chamber and the turbine section, the conditions at the turbine inlet are calculated according to ISO standard 2314 [31]. This ISO standard defines a hypothetic turbine inlet temperature where the complete amount of cooling air (subscript *Cool*) in the gas turbine engine is mixed with the exhaust gas from the combustion chamber (subscript *CC*) prior to the turbine section. The mixing of the exhaust gas from the combustion chamber with the cooling air is also shown in the schematic in Fig. 3.1. According to Seydel [71] the turbine inlet temperature according to ISO 2314 can be calculated with a stationary energy balance:

$$T_4 = \mathrm{TIT}_{\mathrm{ISO}} = \frac{\dot{m}_{\mathrm{CC}} \overline{c}_{\mathrm{p}}\big|_{\mathrm{T_{ref}}}^{\mathrm{T_{CC}}} (T_{\mathrm{CC}} - T_{\mathrm{ref}}) + \dot{m}_{\mathrm{Cool}} \overline{c}_{\mathrm{p}}\big|_{\mathrm{T_{ref}}}^{\mathrm{T_{Cool}}} (T_{\mathrm{Cool}} - T_{\mathrm{ref}})}{\dot{m}_4 \overline{c}_{\mathrm{p}}\big|_{\mathrm{T_{ref}}}^{\mathrm{T_4}}} + T_{\mathrm{ref}}\,. \qquad (3.10)$$

This turbine inlet temperature has to be determined iteratively. Although this definition of the turbine inlet temperature is often used to determine the performance of the gas turbine, it does not correspond to the real temperature of the hot gas at the turbine inlet. The true thermodynamic state of the hot gas at the turbine inlet shows a higher temperature, a lower mass flow rate as well as a different mixture composition. Nevertheless, for thermodynamic calculations in gas turbines the turbine inlet temperature is typically used.

In order to exploit the full potential of the engine, additional fuel is added at wet operating conditions to compensate the temperature drop due to water addition. For all calculations in this thesis the turbine inlet temperature (ISO 2314) at wet operation is held constant compared to the temperature at dry conditions. Investigations are carried out for turbine inlet temperatures between 1500 K and 1700 K and different water to fuel ratios.

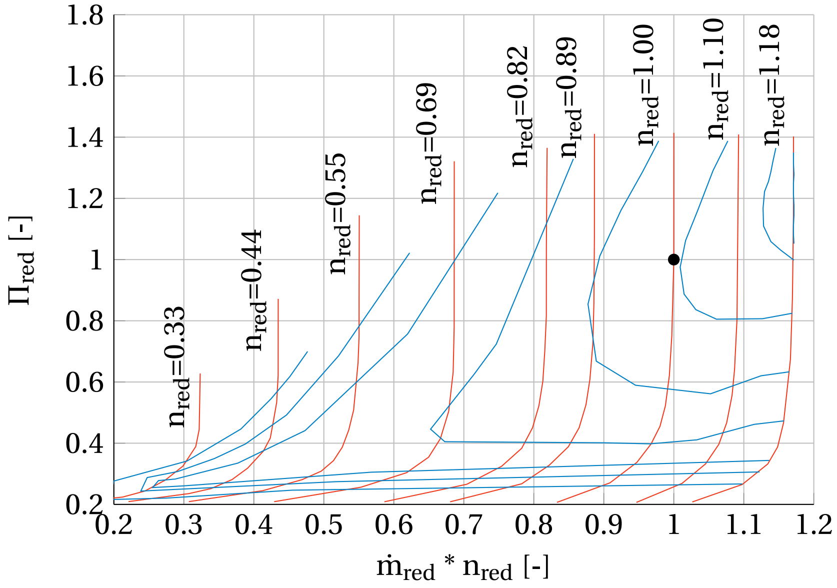

Figure 3.4: Typical turbine map for an axial turbine. Adapted from Seydel [71].

3.1.1.3 Modeling of the Turbine

Similar to the modeling of the compressor, a turbine performance map is often used to describe the performance of the turbine apart from the design point. A typical turbine performance map for an axial turbine is shown in Fig. 3.4. Red lines are symbolizing lines of constant reduced rotational speed, whereas blue lines mark different isentropic efficiencies of the expansion. Due to the fixed grid frequency, the reduced rotational speed of the turbine is constant. Furthermore, as the mass flow rate in the turbine is increasing with rising water content, operation of the turbine is limited to reduced pressure ratios of 1 and higher. As shown in Fig. 3.4, a linear relation between Π_{red} and $\dot{m}_{red} * n_{red}$ is found under the given constraints. Consequently, the determination of the turbine operating point at wet conditions can be simplified significantly. Given a pressure of 1 bar at the turbine outlet the relation between pressure at the turbine inlet and mass flow rate through the turbine is described according to Stodola's Cone Law[2] [76]. According to this law, the pressure at the turbine inlet (p_4) increases compared to dry reference conditions

---

[2] This equation was originally designed for the calculation of steam turbines. As shown by Traupel [78], it is also valid for the calculation turbines working with ideal gases.

(index *dry*) if water is injected into the gas turbine:

$$\frac{p_4}{p_{4,\mathrm{dry}}} = \frac{\dot{m}_4}{\dot{m}_{4,\mathrm{dry}}} \sqrt{\frac{R_4 T_4}{R_{4,\mathrm{dry}} T_{4,\mathrm{dry}}}} \sqrt{\frac{1-\left(\frac{p_{5,\mathrm{dry}}}{p_{4,\mathrm{dry}}}\right)^2}{1-\left(\frac{p_5}{p_4}\right)^2}} \; . \tag{3.11}$$

In order to calculate an updated operating point of the turbine, Stodola's equation is used for all operating points in this thesis. As the mass flow rate through the turbine is known from combustion chamber calculations (see section 3.1.1.2), an updated pressure at the turbine inlet is determined. The reference conditions for this calculation are set to dry operation at a similar turbine inlet temperature ($m_{4,\mathrm{dry}}$, $R_{4,\mathrm{dry}}$, $T_{4,\mathrm{dry}}$ and $p_{4,\mathrm{dry}}$).

In order to calculate the power output of the turbine section an isentropic efficiency has to be determined. As shown in Fig. 3.4 the isentropic efficiency of the turbine is almost constant under the given constraints. Consequently, a constant value of $\eta_{\mathrm{Turb,is}}$=0.92 is used for all calculations in this thesis. According to the work of Seydel [71] similar values of $\eta_{\mathrm{Turb,is}}$ are found in typical modern gas turbines. Finally, the power output of the turbine is calculated according to the following formulas:

$$P_{\mathrm{Turb}} = \dot{m}_4 \int_4^5 c_{\mathrm{p}}(T)\,dT \tag{3.12}$$

$$= \dot{m}_4 \left(\overline{c}_{\mathrm{p}}\big|_{\mathrm{T_{ref}}}^{\mathrm{T_5}} (T_5 - T_{\mathrm{ref}}) - \overline{c}_{\mathrm{p}}\big|_{\mathrm{T_{ref}}}^{\mathrm{T_4}} (T_4 - T_{\mathrm{ref}}) \right), \tag{3.13}$$

$$T_5 = T_4 - \eta_{\mathrm{Turb,is}} \left(T_4 - T_{5,\mathrm{is}} \right) \;, \tag{3.14}$$

$$T_{5,\mathrm{is}} = T_4 \Pi_{\mathrm{Turb}}^{\frac{\kappa-1}{\kappa}} \; . \tag{3.15}$$

3.1.1.4 Modeling of the Heat Recovery Steam Generator

As shown in Fig. 3.1, heat is extracted from the hot exhaust gas to produce steam for operation at steam injected conditions. This is done in a heat recovery steam generator (HRSG). As the amounts of injected steam are small compared to the exhaust gas mass flow rate, a sufficient amount of waste heat is available in the gas turbine. The generation of a sufficient amount of steam can be guaranteed at any realistic mode of operation. Therefore, no calculation of the HRSG is included in this calculation model.

3.1.1.5 Calculation of Power Output and Efficiency

Finally, the power output of the gas turbine at a given operating point is calculated:

$$P_{\mathrm{GT}} = P_{\mathrm{Comp}} + P_{\mathrm{Turb}}. \tag{3.16}$$

The efficiency of the cycle is calculated using the lower heating value of natural gas (H_{LHV}=50.245 MJ/kg):

$$\eta_{GT} = \frac{P_{\mathrm{GT}}}{\dot{m}_3 H_{\mathrm{LHV}}}. \tag{3.17}$$

3.1.2 Results of the Gas Turbine Performance Simulation

Based on the configuration described above, the gas turbine performance is analyzed for typical gas turbine operating conditions. In this study, the gas turbine performance is analyzed for different turbine inlet temperatures (T_4) and variable water to fuel ratios Ω_{W} or steam to fuel ratios Ω_{S}. In order to keep the turbine inlet temperature constant, additional fuel is added at wet operating conditions. An overview over the inlet conditions of the gas turbine performance simulator is given in Tab. 3.1.

Figure 3.5 gives an overview over the power output as well as the efficiencies at water and steam injected conditions. In the figure, curves for operation at constant turbine inlet temperature are marked in red while lines of constant Ω are shown in blue color. Independent of the turbine inlet temperature, the power output increases significantly with rising water content. This is true for water as well as steam injection. However, at constant T_4, Fig. 3.5 clearly shows increasing thermal efficiencies for steam injection, whereas η_{GT} slightly falls if water is added. Kail [34] states that the increased thermal efficiency for steam injection comes from the recuperation of thermal energy from the exhaust gas which is used for the steam generation. Nevertheless, the drop of the thermal

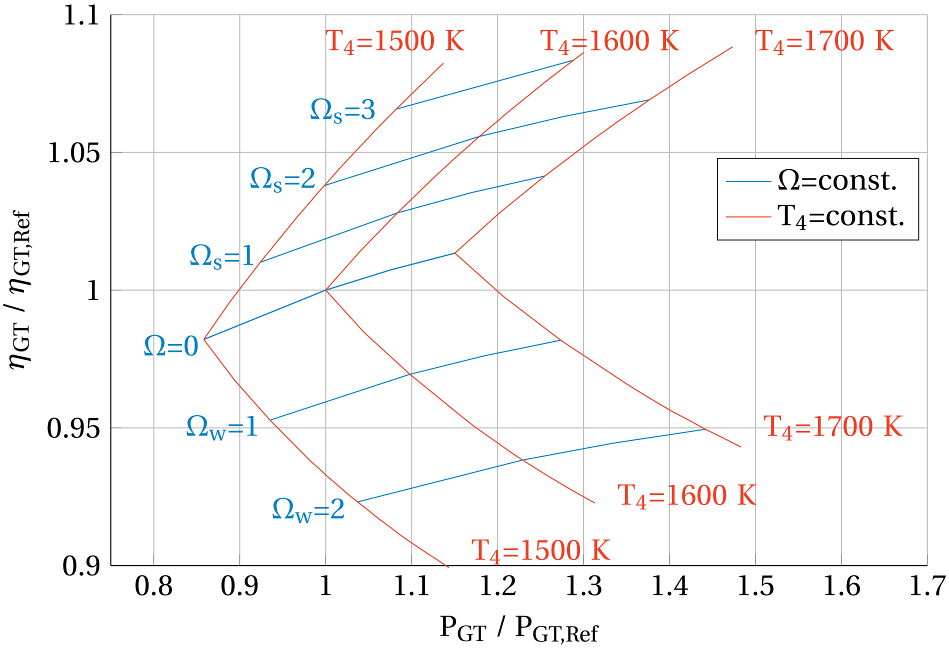

Figure 3.5: Simulated operating map of a gas turbine with water or steam injection at $\Pi_{\text{Comp,dry}}$=20 .

efficiency of the gas turbine is low for water injection. This still allows sufficiently efficient operation of gas turbines with water injection. Furthermore, the complexity as well as the investment costs of the system can be significantly reduced for water injection compared to steam injection. Due to the

Table 3.1: Inlet conditions of the gas turbine simulation tool.

T_0	288.15	K	$\Pi_{\text{Comp,dry}}$	20	-
T_3	288.15	K	$\Pi_{\text{Turb,dry}}$	20	-
$T_{\text{W,in}}$	288.15	K	$\eta_{\text{Comp,pol}}$	0.92	-
$T_{\text{S,in}}$	573.15	K	$\eta_{\text{Turb,is}}$	0.92	-
p_0	1	bar	$\dot{m}_{\text{Cool}}/\dot{m}_2$	0.23	-
p_3	30	bar	$\text{SM}_{\text{Comp,crit}}$	5	%
$p_{\text{W,in}}$	30	bar			
$p_{\text{S,in}}$	30	bar			
$\gamma_{\text{O}_2,0}$	0.21	-			
$\gamma_{\text{N}_2,0}$	0.79	-			
$\gamma_{\text{CH}_4,3}$	1	-			

simple setup of the water injection system a retrofit of a water injection system seems to be possible.

A closer look at Fig. 3.5 reveals further differences between steam and water injection: At similar Ω values the power increase due to water injection is larger compared to steam injection. At $\Omega = 2$ and a turbine inlet temperature of 1600 K a power increase of 23 % is found for water injection whereas only 17 % increase is found for steam injection. Due to the lower specific enthalpy of liquid water compared to steam, a similar amount of liquid water causes a stronger temperature reduction compared to the injection of steam. Consequently, a higher amount of additional fuel is needed to compensate the temperature drop, leading to a stronger increase of the mass flow rate in the turbine as well as a higher power output compared to steam injection.

Besides this, the operating range of the gas turbine changes if water or steam is injected. Figure 3.6 shows a comparison of the maximum Ω values for water and steam injection at similar operating conditions as described in Fig. 3.5. For all operating points in these two figures the amount of water in the combustor is limited by the critical surge margin of the compressor. Therefore, stable operation of the gas turbine is not possible for Ω values higher than Ω_{max}. According to Fig. 3.6 the maximum amount of liquid water that can be added is lower compared to the maximum amount of steam. This ef-

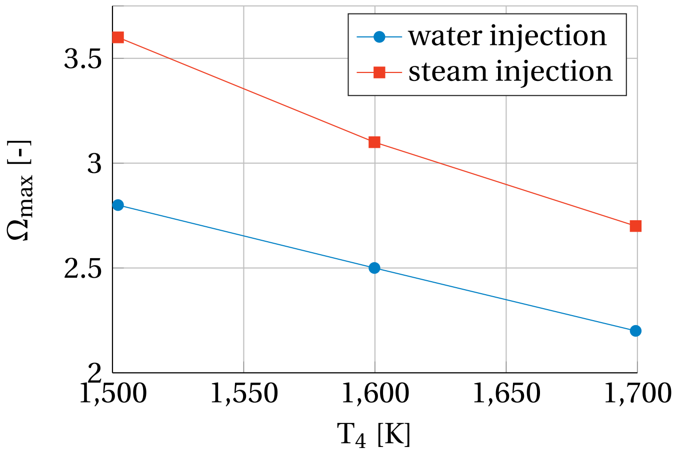

Figure 3.6: Ω_{max} for gas turbine operation with water or steam injection at $\Pi_{\text{Comp,dry}}$=20 .

fect can be attributed to the higher fuel mass flow at operation with water injection compared to steam injection. As more fuel is needed to compensate the temperature drop, less water can be injected before the surge margin of the compressor is exceeded. However, the maximum amount of water is not only influenced by the physical state of the water. Especially the design of the compressor strongly influences $\Omega_{\max}$. If the surge margin of a compressor at its design point is high, a high amount of water or steam can be added before the surge margin is exceeded. Consequently, $\Omega_{\max}$ is shifted to higher values. In contrast, if the compressor surge margin at the design point is low, the maximum amount of water in the gas turbine is smaller. Besides the design of the compressor, the temperatures of water and ambient air strongly influence $\Omega_{\max}$. Further information on the influence of these parameters on the operating range of wet gas turbines can be found in the work of Wasicek [83].

Independent of the exact operating conditions, the thermodynamic analysis shows that the power output of a gas turbine can be increased significantly by water injection. Therefore, the operational window can be extended to higher power outputs. Besides these positive influences of water or steam injection, literature also lists some drawbacks of the technology: Many authors point out that water or steam injection raises the dynamic pressure activity in the combustor [43, 53, 56] which might lead to thermoacoustic instabilities. According to experimental investigations by Pavri [56], water injection has a higher influence on the level of the oscillations compared to steam injection. Recent experimental investigations in a premixed lab scale combustor with water injection by Stadlmair [73] confirm the increase of the dynamic pressure amplitudes, especially for low frequency oscillations. Besides these thermoacoustic problems, Lefebvre [43] points out that combustion systems with water injection require a high level of water purity to prevent deposits and to reduce hot gas corrosion at the components downstream of the combustor. Due to the high costs for the generation of purified water, this requirement raises the operational costs and directly influences the economic efficiency of the machine.

Additional problems may arise if water is injected in gas turbines which originally were not designed for this mode of operation. Higher pressure and heat loads might lead to a faster wear of the machine [43]. Due to the higher heat capacity of the exhaust gas at wet operating conditions, heat transfer to structural components increases, leading to higher material temperatures and higher stresses [40]. In order to keep the material temperatures at a reasonable level, additional cooling air is required. This reduces the engine efficiency. Similarly, the higher mass flow rates increase the structural loads in the turbine section. Alltogether, this might lead to a reduction of the engine lifetime as well a decrease of the maintenance intervals [43, 56].

3.2 Effects of Water Injection on Combustion

Apart from the effects of water injection on power output, influences on the flame behavior are observed. In the following, the reasons of this influence of water on the flame are clarified. In a second step, the effects of water injection on technical flames are presented based on literature data.

Water or steam injection in flames lead to a reduction of the flame temperature and have an influence on chemical kinetics (NO_x, CO) [6, 21, 36]. Similar to other diluents, the addition of water changes the specific heat capacity of the gaseous mixture. For rising water contents this leads to increasing heat capacities and, considering a constant amount of fuel, to lower flame temperatures. Water injection also causes a reduction of the fuel concentration in the fresh gas mixture which leads to a further drop of the flame temperature [20]. According to simulations of Dlugogorski [20], this effect is solely related to the physical effect of water addition and can be found even if water is treated as an inert diluent. In comparison to the addition of other diluents, a larger temperature drop is found for water addition. Due to the different heat capacities of various diluents, different temperature drops are found for similar diluent amounts [24]. Generally, the temperature reduction increases with the heat capacity of the diluent. Due to the high heat capacity of water, the effects of dilution are strong compared to other diluents [20]. This is true especially for the injection of liquid water. As additional energy is needed for the evaporation of the water droplets, a higher temperature drop is observed in flames with water injection compared to steam injection [56].

Besides this thermal effect, a second influence of water on the flame exists. As often stated in literature, water addition may impact reaction pathways. This chemical effect is mainly related to the change of important radical concentrations in the flame. According to several publications, water addition changes the concentration of radicals in the reaction zone [48, 86]. Especially the concentrations of O, H, and OH-radicals are influenced [48]. As these radicals are participating in many elementary reactions of the combustion process, reaction rates are strongly influenced by the changed concentrations. Many authors state that this also influences the pollutant concentrations in the burnt mixture [86]. Apart from the changed radical concentrations, some authors describe the important influence of water on third body reactions[36]. Due to its high efficiency in third body reactions, water can participate as a non-reacting molecule, thereby influencing reaction rates. Reaction kinetic simulations from Seiser [70] confirm this third body effect of water molecules.

Nevertheless, disagreement about the importance of the chemical effect is found in the scientific community. Controversial results about the existence of a chemical effect of water addition have been published over the past years. While Mazas, Seiser and Zhao [48, 70, 86] found an influence of the water addition apart from the thermal effect, the chemical effect is said to be negligible in the publications of Galmiche and LeCong [24, 41]. Recent detailed investigations in the context of premixed steam injected flames clarified this matter. According to Göke [27] the controversial results exist due to the fact that the thermal effect is dominating for typical operating conditions. It is widely accepted that the temperature reduction effect exceeds the chemical effect on the combustion process. This makes it difficult to separate both effects and to determine the chemical influence of water in experimental investigations. Göckeler [25] states that the chemical effect is strongly influenced by the choice of operating conditions which further explains the inconsistency of the results in this field. As the present study does not focus on the determination of the chemical effect, a detailed discussion about the mentioned controversy will not be provided. Additional information can be found in extensive literature reviews by Göke [27] and Göckeler [25].

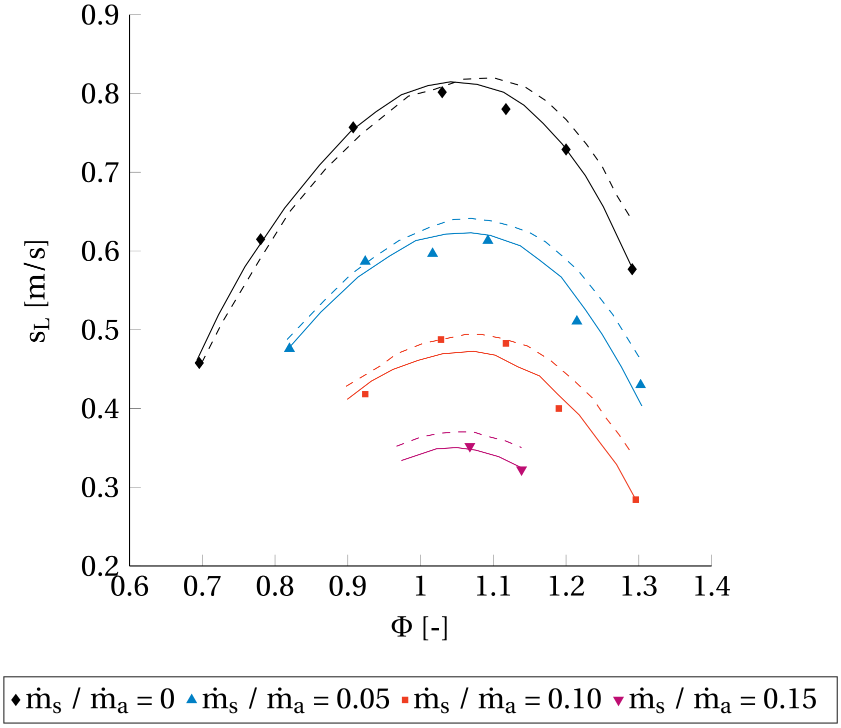

Figure 3.7: Flame speeds of steam injected, premixed flames at different steam-air and equivalence ratios. Comparison of experimental data (symbols) and simulations with GRI Mech 3.0 (–) and Aramco Mech 1.1 (- -). Adapted from [26].

Besides these theoretical investigations, influences of water injection on macroscopic flame properties are described in literature. Generally, the findings on steam injected flames outweigh the research results for water injection. The reason is the more homogeneous mixture composition in the combustion process for steam injected operation. As steam can easily be distributed, effects of inhomogeneous mixture composition can be neglected. Still, the results of water and steam injection should be comparable on a qualitative level. As described by Schetter [68], the effect of water injection should exceed the effect of steam injection.

In order to analyze the effect of steam injection on the mixture reactivity, investigations on the laminar flame speed s_L are presented in literature. As mentioned by Göckeler, the experimental investigations on flame speeds of water and steam injected flames are relatively scarce. Nevertheless, various experimental and numerical investigations agree that steam addition leads to a significant decrease of the laminar flame speed [4, 24, 48]. According to Göckeler [25], the results of these different investigations are highly similar to each other. Unfortunately, these investigations cover only a small region of the operational range of steam injected premixed flames and no general conclusions about the influence of steam addition on the mixture reactivity can be drawn.

To overcome this deficiency, Albin [2] and Goeckeler [26] conducted a comprehensive study on flame speeds at steam diluted conditions. Figure 3.7 shows the results of this study for different equivalence ratios and different steam-air mass flow ratios. The experimental results for s_L show a bell shaped curve for variable equivalence ratios. Independent of Φ, the reactivity of the mixture decreases with increasing humidity which leads to a shift of the bell curve to lower absolute flame speeds. Alongside the experiments, numerical results are shown in Fig. 3.7. The numerical results originate from reaction kinetic simulations with the GRI 3.0 reaction mechanism [72] as well as the Aramco 1.1 reaction mechanism [50]. As experimental and numerical results are in good agreement over the complete equivalence ratio range, numerical simulations can be used to assess the influence of steam on the reactivity of a mixture. Numerical data by Göke [27] extends the experimentally determined data to higher adiabatic flame temperatures and lower equivalence ratios (shown in Fig. 3.8). Decreasing flame speeds are determined for increasing water contents at constant Φ as well as for increasing water contents at constant flame temperatures. The reduction of the mixture reactivity is lower for operation at constant flame temperature compared to operation at constant Φ. However, the influence of steam injection can not be compensated completely by adding additional fuel.

According to Krüger [37], the reduction of the mixture reactivity might also influence the combustion regime. As shown above, water or steam injection reduces the laminar flame speed s_L and leads to an increase of the thermal thickness of the flame δ_f^0. This increases the chemical timescale τ_c of the reaction compared to dry operation (see Eq. 2.45). Given a constant level of turbulent fluctuations, the Damköhler number decreases and the Karlovitz number rises, leading to a shift of the operating point in the Borghi diagram. Figure

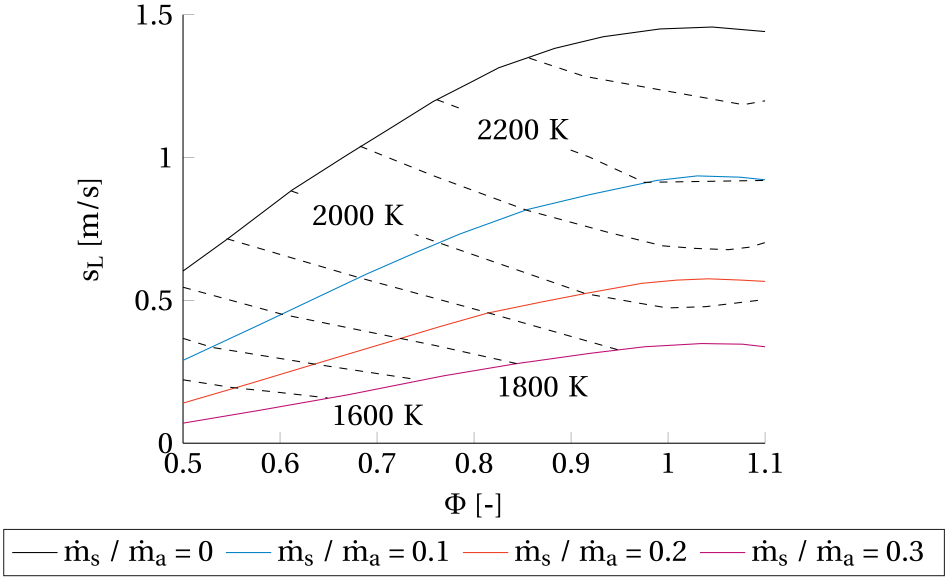

Figure 3.8: Calculated laminar flame speeds of steam injected, premixed flames at different steam-air ratios and different Φ according to Göke [27].

3.9 shows this shift for typical operating conditions of an atmospheric combustion test rig at TUM (blue line) as well as an industrial gas turbine (red line) [37]. Point A symbolizes dry operation whereas point B shows operation at a water to fuel ratio of 5. Both operating characteristics are determined from typical assumptions for the turbulence parameters[3] as well as one-dimensional free flame calculations in Cantera [29] with the GRI 3.0 mechanism [72]. While the calculations for the test rig operation were conducted at atmospheric pressure, a pressure of 20 bar is assumed for gas turbine operation. Depending on the local water concentration, the combustion regime might change from the regime of thin reaction zones to the regime of broken reaction zones, especially for operation at elevated pressures. In the thin reaction zones regime the turbulent eddies in the flow can only deform the flame front. However, in the regime of broken reaction zones, turbulent eddies are able to perturbate the inner layer of the reaction zone. This might transport important chain branching radicals away from the flame front, thereby promoting local extinction phenomena. These local extinctions of the flame can affect flame stability, flame noise and might even lead to global extinction of

---

[3] Isotropic turbulence, turbulence intensity Tu=15%, $\overline{u}$=40 m/s, u'= 6 m/s.

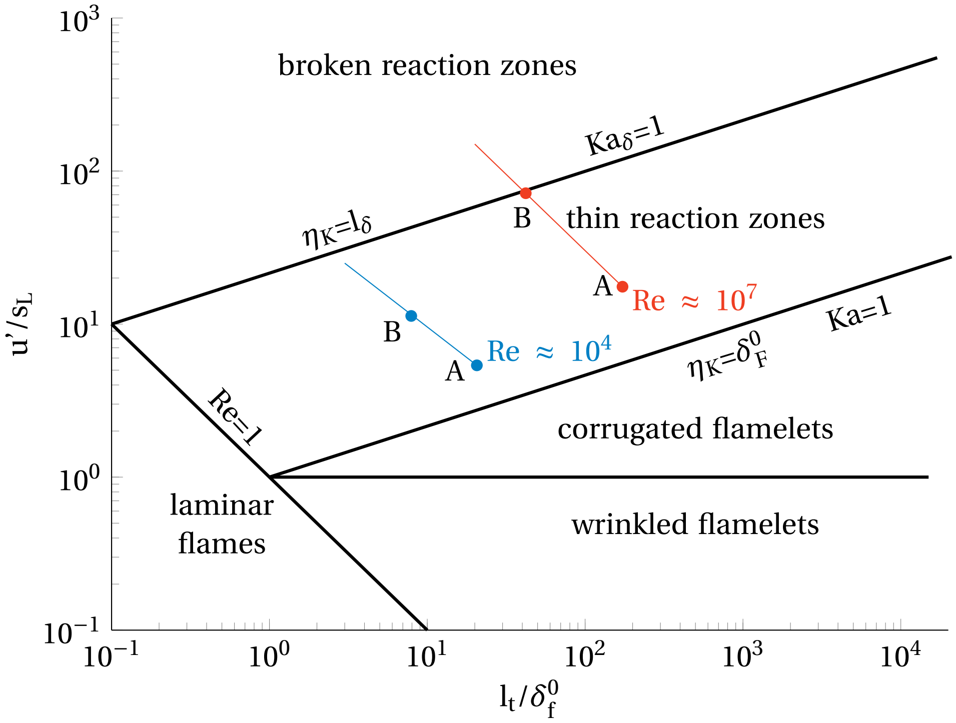

Figure 3.9: Classification of dry and steam injected flames in a Borghi diagram. Comparison of typical atmospheric labscale operating conditions (blue line) and gas turbine operating conditions (red line). Adapted from Krüger [37].

the flame [59]. Still, Fig. 3.9 shows that wet operation in the atmospheric test rig takes place in the regime of thin reaction zones. However, similar to gas turbine operating conditions, the flame regime moves closer to the regime of broken reaction zones with increasing water content. Generally, no maximum water content for stable operation of the gas turbine can be specified as the different combustion regimes are not separated by strict boundaries in the Borghi diagram.

3.3 Influence of Water Injection on Pollutant Formation

Apart from the steam influence on mixture reactivity and flame speed, many sources in literature mention an impact of steam addition on pollutant formation. Consequently, the following literature review focuses on the formation of CO as well as NO_x under steam injected operating conditions.

The moderating influence of water and steam injection on the NO_x emissions of gas turbines is widely known. Consequently, multiple investigations on the influence of water or steam injection on the NO_x formation are found. However, as this technology was mainly used in the era of non-premixed combustion, these investigations focus on the emission behavior of non-premixed engines [12, 32, 80, 86] or the combustion of liquid fuel [13, 80]. Still, recent investigations describe the influence of steam on NO_x formation in premixed gas turbine engines burning natural gas. Among others, Guo and Moore [30, 56] report decreasing NO_x emissions due to steam injection in numerical as well as experimental investigations. Due to the lowering flame temperatures, most of the reduction is attributed to the thermal effect. Besides this, Miyauchi [52] also found a drop of NO_x concentrations with increasing steam content at constant maximum flame temperatures. In his experimental studies, a steam-injected one-dimensional methane-air flame was characterized using spatial measurements of temperature and species concentrations. He concludes that the NO_x reduction in steam injected flames is influenced by another effect apart from the temperature reduction, e.g. a chemical effect. In order to expand these results to a broader range of operating conditions, Bhargava [6] experimentally investigated pollutant formation in premixed steam injected flames at different equivalence ratios and different pressure levels. He reports a strong reduction of the NO_x concentrations independent of Φ and the combustor pressure. Furthermore, a shift of the NO_x concentration curve to higher equivalence ratios was found at steam injected conditions. Recently, Göke [28] published an experimental and numerical investigation on NO_x formation in steam injected premixed flames for a wide range of equivalence ratios and different flame temperatures. Figure 3.10 summarizes the findings of his study and gives an overview on NO_x formation in steam injected industrial flames. According to his investigations, steam addition reduces NO_x emissions at decreasing as well as at constant temperatures.

Regarding CO emissions, less data is available in literature. Although many authors describe rising CO emissions at wet operating conditions [12, 43, 69],

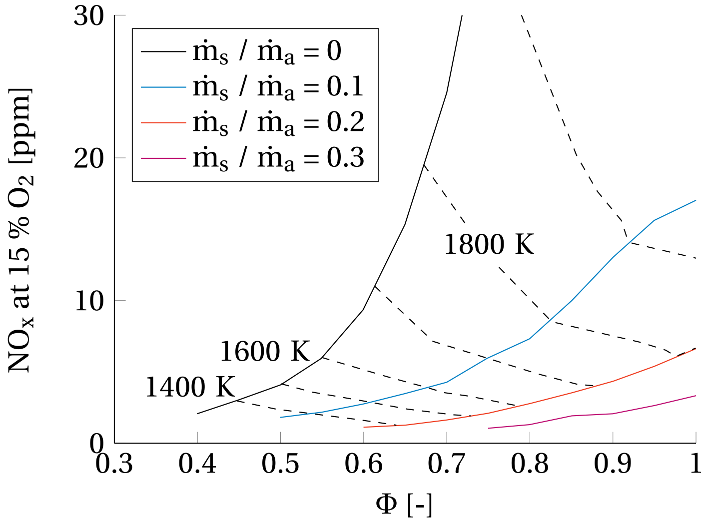

Figure 3.10: Measured NO$_x$ emissions at dry and steam injected operating conditions. Adapted from Göke [28].

detailed studies on the effect of water or steam injection on the CO emissions are scarce. Bhargava investigates this topic for an industrial premixed gas turbine burner and shows experimentally and numerically determined CO concentrations at different degrees of humidity and different pressure levels [7]. The numerical results in this investigations were determined using a network of perfectly stirred reactors resembling the performance of the investigated combustion test rig. Bhargava's results show a shift of the CO concentration curve to higher equivalence ratios at steam injected operating conditions (see Fig. 3.11). Due to the V shape of the curves, CO concentrations can either be increased or lowered by steam injection, depending on the operating point of the combustor. For low equivalence ratios, the shift of the CO concentration curve might lead to a strong increase of CO emissions. Consequently, many authors speak of increasing CO emissions due to decreasing flame stability at wet operating conditions [41, 82]. However, at higher equivalence ratios, steam injection leads to a significant decrease of the CO values. According to the data of Bhargava, this effect is closely related to the temperature drop due to steam injection. Göke [27] was able to extend these results up to higher amounts of water. His findings correlate closely with the results of Bhargava and show a shift of the CO curves to higher equivalence ratios at steam injected operating conditions. However, he points out that the CO formation in

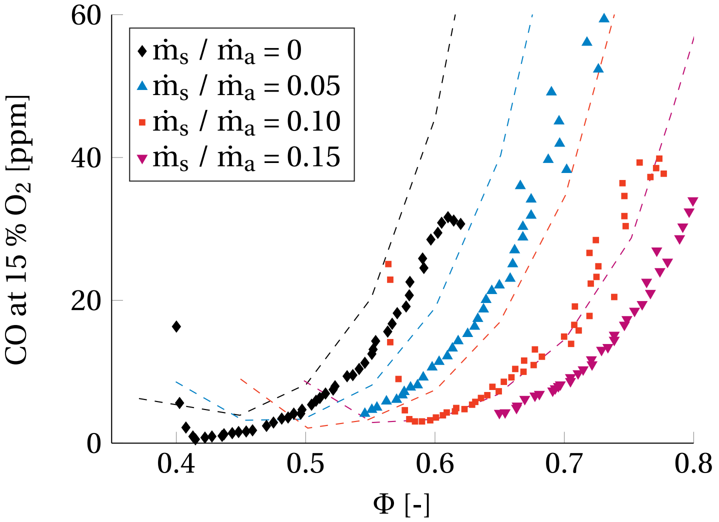

Figure 3.11: Measured (symbols) and simulated (- -) CO emissions at dry and steam injected operating conditions. Adapted from Day and Bhargava [19].

steam injected flames is strongly influenced by the configuration as well as the operating conditions of the system. Consequently, no universal statement on the CO emissions in wet flames can be given.

4 Experiment

In order to investigate water injection in premixed flames, an atmospheric experiment was employed. This section describes the design of the test rig as well as of the water injection system. Additionally, an overview of the applied measurement techniques is given.

4.1 Design of the Test Rig

4.1.1 Atmospheric Single Burner Test Rig

The experimental investigations in this thesis are conducted in an atmospheric single burner test rig equipped with a swirl burner. To utilize synergies with previous investigations, an existing combustion test rig was equipped with a water injection system. The applied burner as well as the water injection system are designed for a wide range of operating conditions. Figure 4.1 shows a sketch of the final setup. A radial compressor transports ambient air to the inlet of the test rig. This air is electrically preheated ① to typical compressor outlet temperatures of modern gas turbines. In the following, preheated air and natural gas are perfectly premixed in a mixing dome. Subsequently, the mixture flows through a cylindrical plenum ② and enters the A2EV swirler ③. This generic swirl burner has already been used in multiple combustion experiments and is described in detail in the work of Sangl [67]. The swirler is a thickwalled cone with four tangential openings at the sidewalls and one axial orifice at the head end. The fuel-air mixture flows through this geometrical structure and creates a swirling flow field. In the swirler, the ratio of the cross sectional areas of the tangential and the axial openings determine the swirl number in the flow. Downstream of the swirler the flow is guided through a conical mixing tube ④ of 140 mm length. The diameter of the mixing tube reduces from 100 mm at the inlet to 75 mm at the outlet. Due to the reduction of the cross-sectional area of the mixing tube the flow accelerates axially. At the end of the mixing tube the cross sectional area of the flow channel expands suddenly where the flow enters the cylindrical combustion chamber (⑥, diameter 156 mm). Due to the rapid area increase, the streamlines of the flow expand radially outward and vortex breakdown occurs. An inner and an outer recirculation zone form which stabilize the flame aerodynamically.

Due to the modular design of the test rig, two different combustion chambers can be employed. For optical investigations a cylindrical quartz glass tube with a length of 200 mm is used. For local species concentration measurements this glass chamber is replaced by a cylindrical steel tube with a similar inner diameter. In order to extend the measurement area farther downstream, the length of the steel chamber is increased to 500 mm. To allow local measurements in the flue gas, eleven measurement ports are positioned at different axial distances in the combustor. The detailed setup of the local measurements is described in section 4.2.1.

For investigations with water injection, an axial injection system ⑤ is used. The exact configuration of this water injection system is presented in the following section. Finally, the exhaust gas exits through a water cooled exhaust gas duct ⑦. In addition to the local species concentration measurements a sampling probe ⑧ is included for measuring global pollutant concentrations.

4.1.2 Design of the Water Injection System

For investigations at wet operating conditions, a water injection system was designed for the existing atmospheric test rig. Air-assisted nozzles are used in order to achieve a high atomization quality independent of the water mass flow rate. These nozzles use the kinetic energy of a secondary fluid for atomization. During all experimental investigations, ambient air was used as atomizing fluid. Unfortunately, the nozzles require a high pressure level of the atomizing air to guarantee good atomization. In industrial gas turbine engines

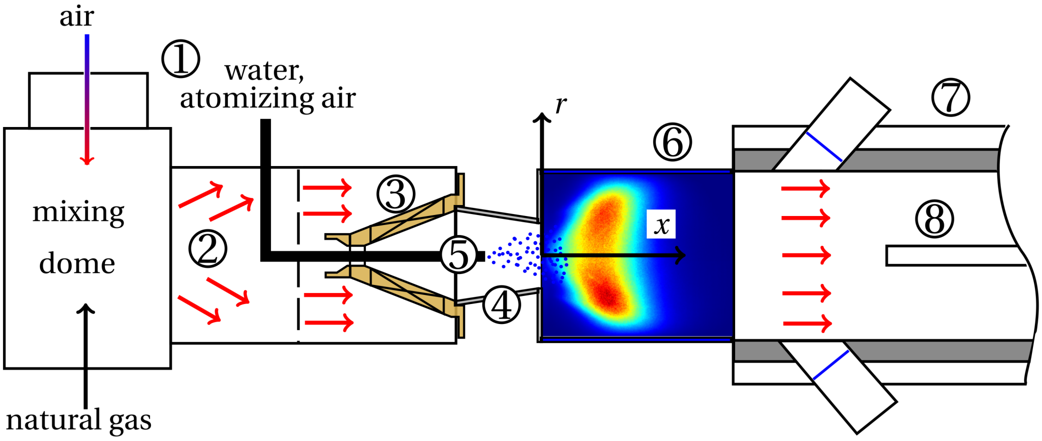

Figure 4.1: Setup of the atmospheric test rig for optical investigations.

excess air at a high pressure level is typically not available. The air-assisted nozzles used in this thesis are therefore not suitable for the use in industrial gas turbines. However, for the present experiment, the advantages of the air-assist nozzles outbalance this disadvantage: Firstly, the atomizing air mass flow provides an additional parameter to influence the atomization quality of the nozzle. This allows a variation of the water mass flow rate independent of the droplet size. Secondly, the operating range of the air-assisted nozzle is significantly wider compared to typical pressure-swirl atomizers used in industrial gas turbines. Due to the wide range of the water mass flows covered in this work, this aspect is of high importance. For industrial applications, the nozzle can easily be substituted with a standard pressure-swirl atomizer.

The water is filtered and deionized before entering the test rig to avoid depositions in the combustion chamber and in the injection system. In the test rig two concentric steel tubes transport the water and the atomizing air to the injection location where a nozzle atomizes the water. As the burner configuration shows a rotational symmetry, the water injection system was positioned concentrically to the other burner components. In order to reduce flow disturbances in the burner, the tubes enter the plenum far upstream of the swirler. Both tubes are positioned concentrically to the axial opening of the swirler. Due to the tube in tube arrangement, evaporation of the water is effectively prevented. As shown in Fig. 4.1, the water injection lance is positioned on the combustor centerline in the mixing tube 70 mm upstream of the combustion

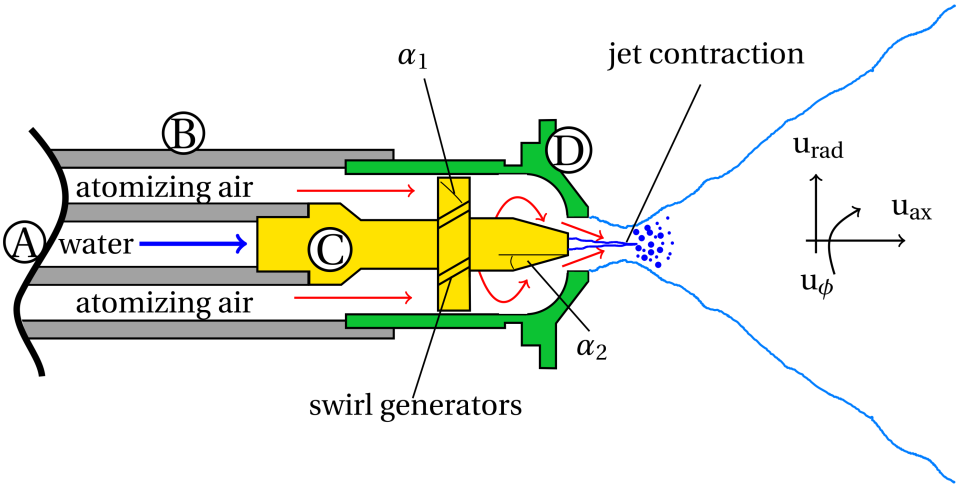

Figure 4.2: Detailed sketch of the water injection system.

chamber inlet. The axial position of the water injection system has been chosen empirically to distribute the water droplets evenly over the complete outlet area of the mixing tube.

Figure 4.2 shows the design of the water injection system in detail. Through an inner tube Ⓐ, water is guided to the water nozzle Ⓒ. This nozzle transports the water to the the outlet orifice and creates a homogeneous jet. Circumferential to the water lance an atomizing air lance Ⓑ is positioned. An air cap Ⓓ guides the atomizing air to the nozzle outlet. A centering ridge on the outside of the water nozzle guarantees that the outlet openings of both nozzles are positioned concentrically to each other. In order to improve the atomization of the liquid, the outlet plane of the water nozzle is retracted compared to the outlet plane of the atomizing air nozzle. Grooves on the outer contour of the water nozzles swirl the atomizing air flow. In the test rig, the swirl of the atomizing air flow and the main flow are directed in the same direction. At the outlet of the air nozzle the flow is guided through a small outlet orifice. As shown in Fig. 4.2, this creates a radial motion in the atomizing air flow. In Fig. 4.2 the flow direction of the atomizing air is indicated with red arrows. At the nozzle outlet the air-assist nozzle forms a complex flow field consisting of axial, radial as well as circumferential velocity components [66, 84].

In order to improve the flexibility of the test rig, different nozzles can be mounted in the water as well as in the air lance. In this thesis, two different nozzle configurations C1 and C2 are utilized to investigate the influence of the water droplet size on the combustion reaction. Both nozzle configurations differ only in the diameter of the water outlet orifice. For both nozzle configurations the overall geometry is identical and the outlet diameter of the air cap is fixed to 5 mm. The diameter of the water outlet is 1.8 mm in configuration C1 and 0.8 mm in configuration C2.

4.1.3 Typical Operating Conditions of the Test Rig

For all operating points analyzed in this thesis, a main air mass flow rate of 80 g/s is chosen. Air is preheated to 673 K to simulate typical conditions at the gas turbine compressor outlet. The test rig is operated on natural gas with a share of more than 97% of methane. The equivalence ratio is calculated with respect to the main air flow. Values between 0.555 and 1.000 are chosen for the experimental investigations. For the atomization of the liquid water, an additional air mass flow is introduced into the test rig. In order to change the atomization quality of the water nozzles, this atomizing air mass flow rate is varied between 2 and 4 g/s. To avoid evaporation of the water in the water tube, this secondary air mass flow is not preheated. The water mass flow rate is adjusted with a mass flow controller to values between 0 and 11.4 g/s. In order to quantify the amount of water in the test rig non-dimensionally, the water mass flow rate is related to the fuel mass flow rate at each operating point:

$$\Omega = \frac{\dot{m}_w}{\dot{m}_f}. \tag{4.1}$$

This water to fuel ratio Ω allows to compare operating points at different levels of thermal power. In this thesis Ω values are changed between 0.0 and 2.5 .

Due to the strong influence of the water injection on the heat capacity of the reactant mixture, changes of the flame temperature in the combustor are expected. In order to investigate this influence of water injection on the flame temperature, two different series of measurements are conducted:

Table 4.1: Operating conditions at constant T_{ad} for measurements at $\dot{m}_{a,at}$=4 g/s.

T_{pre} [K]	Φ [-]	Ω [-]	$\dot{m}_f$ [g/s]	$\dot{m}_w$ [g/s]	T_{ad} [K]
673	0.625	0.0	2.92	0.0	1940.0
673	0.673	0.5	3.14	1.57	1939.5
673	0.729	1.0	3.40	3.40	1939.4
673	0.795	1.5	3.71	5.57	1939.3
673	0.875	2.0	4.09	8.17	1939.5
673	0.921	2.25	4.30	9.68	1939.3

- Measurements at constant equivalence ratio.
- Measurements at constant adiabatic flame temperature.

For investigations at constant Φ, the adiabatic flame temperature decreases with rising water content. However, as known from literature [33], the flame temperature has a significant influence on combustion properties. In order to separate the influences of water addition and flame temperature reduction, the temperature drop due to water addition is compensated using additional fuel. In this second series of measurements, the adiabatic flame temperature, remains constant for rising Ω. As the calculation of the adiabatic flame temperature is not trivial, the operating conditions for the second measurement series are determined prior to the investigations using a Matlab routine. This is done employing a global energy balance around the combustion chamber (see section 2.2.2). The exact calculation procedure of the Matlab routine is presented in section 4.1.4. Table 4.1 shows typical operating conditions for a measurement series at constant adiabatic flame temperature and increasing amounts of water.

4.1.4 Calculation of Input Values at Constant T_{ad}

This section describes the calculation of the inputs for operating points at constant T_{ad}. The calculation is carried out in Matlab in advance of the test

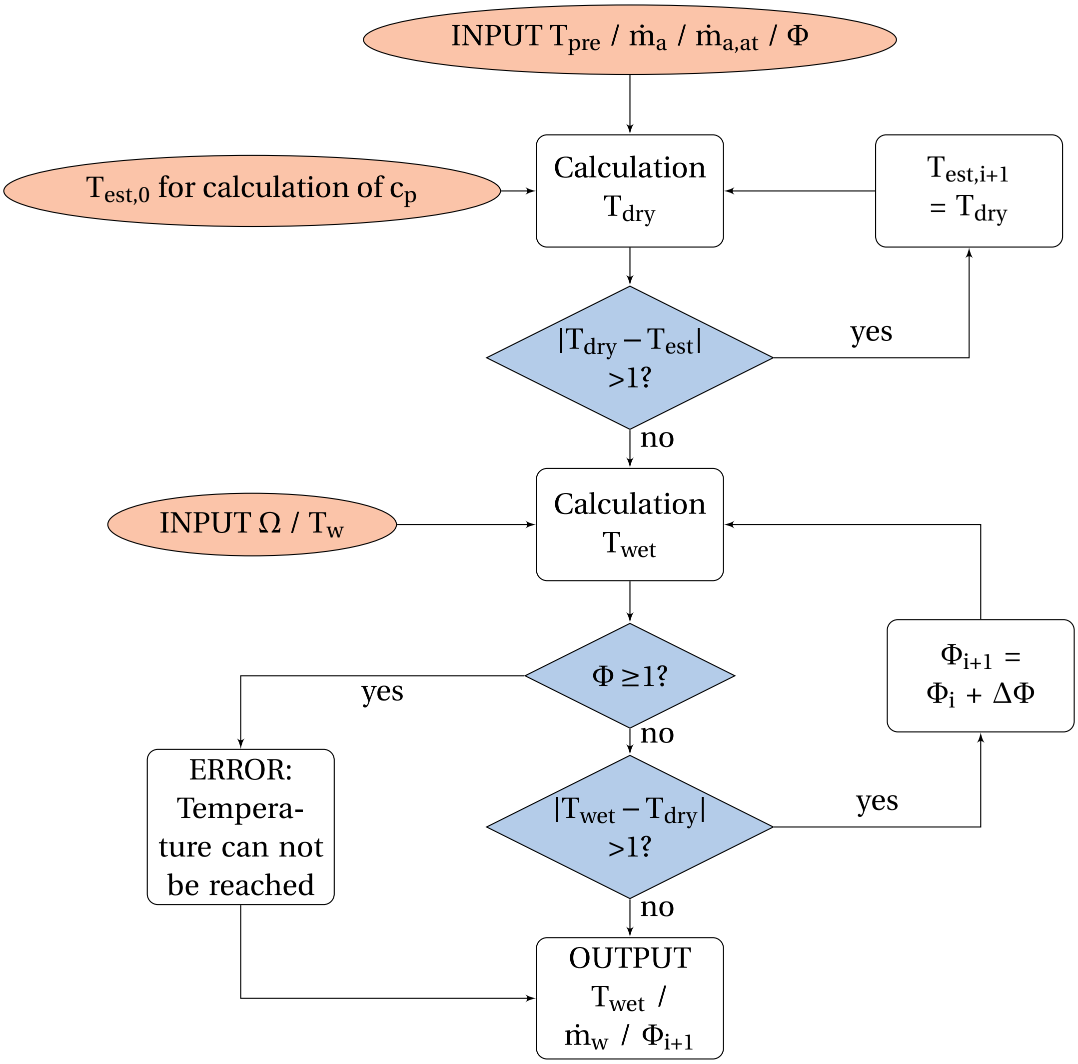

Figure 4.3: Flowchart of the Matlab algorithm to calculate input parameters for operation at constant T_{ad}.

rig experiments. Starting from inlet values from the test rig (T_{pre}, $\dot{m}_a$, $\dot{m}_{a,at}$ and Φ) the adiabatic flame temperature at dry operating conditions (T_{dry}) is determined with Eq. 2.42. The molar heat capacities of the different reactant species are determined with a polynomial approach [49] and an estimated temperature of the combustion products ($T_{est,0}$). Subsequently, the estimate for the product temperature is updated with the value of T_{dry}. The calculation of T_{dry} is reiterated until the product temperature is equivalent to the estimated product temperature.

For the calculation of the wet operating conditions at constant T_{ad}, the water to fuel ratio Ω and the water temperature T_w are used. At first, the flame temperature at wet operating conditions and constant Φ is calculated according to the procedure described for T_{dry}. If the equivalence ratio Φ of the mixture lies below unity and the adiabatic flame temperature of the wet mixture (T_{wet}) lies below the temperature of the dry mixture (T_{dry}), additional fuel is added to the mixture. This is done by changing the equivalence ratio ($\Phi_{i+1} = \Phi_i + \Delta\Phi$). The procedure is reiterated until either the equivalence ratio reaches unity or the temperature of the wet mixture (T_{wet}) equals T_{dry}.

If the equivalence ratio reaches unity, the flame temperature can not be increased further by adding fuel. Therefore, the calculation is stopped at this point. In contrast, if T_{wet} equals T_{dry} a new operating point is obtained.

4.2 Measurement Techniques

The experimental investigations in this thesis are divided into two categories: Measurements to characterize the combustion reaction and investigations to characterize the liquid phase. While the investigations in the gas phase determine the heat release distribution and the pollutant formation, the measurements of the liquid phase reveal the droplet size as well as the distribution of the water in the test rig.

4.2.1 Gas Phase

OH*-Chemiluminescence Measurements

The shape and position of the heat release distribution is determined qualitatively with OH* chemiluminescence measurements in the quartz glass combustion chamber. As known from Lauer [39] the locally measured OH* intensities cannot be related to the heat release distribution in the flame directly. Instead, a complex correction method is necessary to correct the influences of flow turbulence and quenching on the OH* intensity. However, it was shown by Lauer that the integral OH* intensity signal can be used to determine the global heat release rate in the flame [39]. As the changes between the different operating points are moderate, only minor variations in the flow structure as well as the turbulence level in the test rig are expected. Given this assumption, the influences of the flow turbulence is supposed to be similar for all cases investigated in this thesis. Therefore, the OH* measurements can be used to compare the heat release distributions at different operating conditions.

The OH* measurements are conducted with a Photron SAX high-speed camera, an UV image intensifier as well as quartz glass optics with a focal length of 105 mm. For the measurements, the camera is positioned at the side of the combustion chamber perpendicular to the central axis of the test rig. In order to separate the OH* chemiluminescence from broadband radiation of the flame, a UV bandpass filter with a wavelength of 307±5 nm is positioned in front of the camera. For each operating point 2000 images are captured at a framerate of 2000 images per second and a resolution of 180x180 mm(1024x1024 pixels).

The post-processing of the images is done in Matlab. First, all images from one operating point are averaged in order to compensate for the turbulent fluctuations of the flow. Due to the arrangement of the camera and the cylindrical shape of the combustion chamber, all OH* images are line of sight integrated. Consequently, no information about local intensity distributions can be drawn from the images. However, as all averaged images show a high level of symmetry, an Abel deconvolution of the images can be performed. Assuming rotational symmetry of the distribution, this mathematical operation allows to calculate the radial distribution of the OH* intensity in the combustor centerplane. In this thesis, a deconvolution algorithm based on inverse fourier transformation is used [63].

Additionally, the flame length as well as the center of intensity of the OH* distributions is determined. For the determination of the flame length an intensity threshold at 20 % of the maximum intensity in the image is chosen in order to identify the main heat release zone in the OH* images. In a second step, the axial positions in the images are determined where this threshold is exceeded.

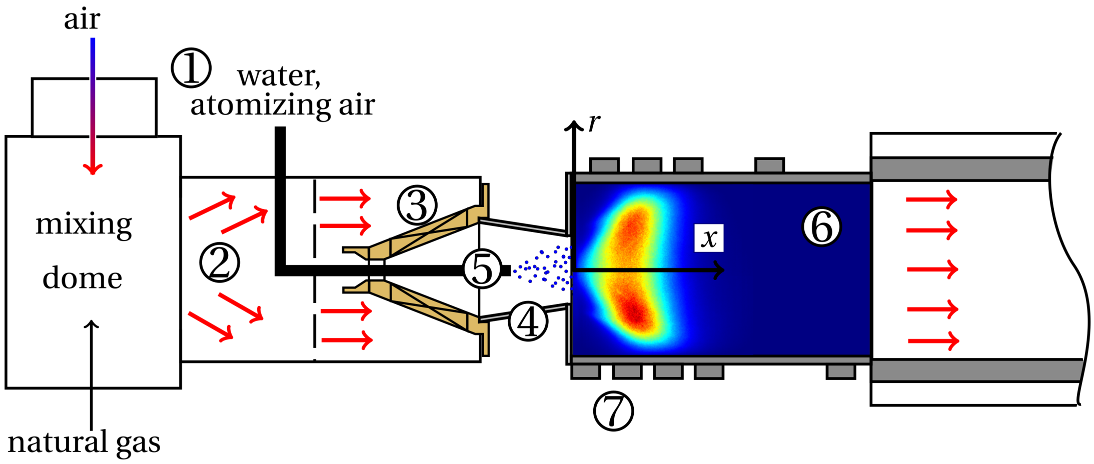

Figure 4.4: The atmospheric test rig for species concentration measurements.

Having determined the beginning as well as the end of the flame, the flame length can easily be calculated. Additionally, the center of intensity of the OH* distribution is calculated with the following formulas:

$$\mathrm{COI}_{\mathrm{x,OH^*}} = \frac{1}{\mathrm{I_{tot}}} \sum_{i,j} \mathrm{I}\left(x_\mathrm{i}, r_\mathrm{j}\right) * x_\mathrm{i}, \tag{4.2}$$

$$\mathrm{COI}_{\mathrm{r,OH^*}} = \frac{1}{\mathrm{I_{tot}}} \sum_{i,j} \mathrm{I}\left(x_\mathrm{i}, r_\mathrm{j}\right) * r_\mathrm{j}, \tag{4.3}$$

$$\mathrm{I_{tot}} = \sum_{i,j} \mathrm{I}\left(x_\mathrm{i}, r_\mathrm{j}\right). \tag{4.4}$$

In these equations, $I(x_\mathrm{i}, r_\mathrm{j})$ symbolizes the intensity of a Pixel at a given position, while x_i and r_j represent the position of the pixel according to the reference frame in Fig. 4.1.

Species Concentration Measurements

In order to analyze the influence of water injection on the pollutant formation in premixed flames, species concentrations are measured globally and locally. As said above, the configuration of the test rig is changed for the probe measurements. Figure 4.4 shows a sketch of the test rig used for species concentration measurements.

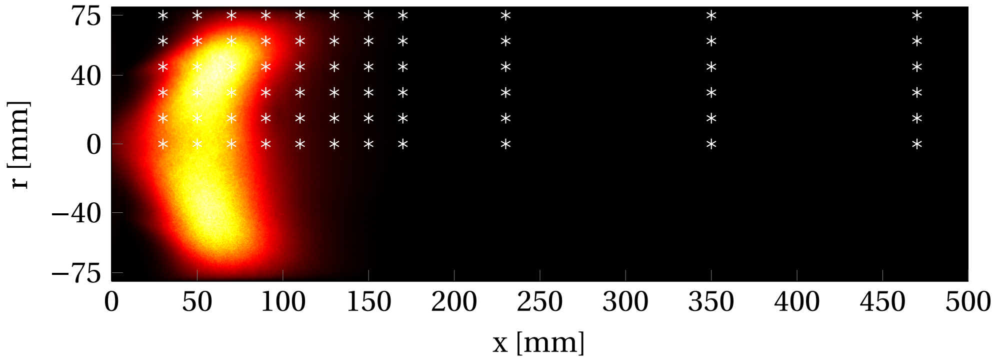

Figure 4.5: Probe positions for local species concentration measurements.

For the local measurements, the quartz glass combustion chamber is replaced by a cylindrical steel chamber of 500 mm length and 156 mm inner diameter. Eleven ports are distributed over the length of the combustion chamber with an unequal spacing. Due to the higher gradients in the upstream part of the combustion chamber, the measurement resolution is increased here. For dry operation, the combustor residence time at the last measurement port is at around 20 ms which is comparable to typical residence times in industrial combustors. Due to the increased volume flow, the residence time is lower at wet operating conditions. At each axial position, measurements are conducted at six different radii. Figure 4.5 shows the probe locations relative to an OH* chemiluminescence image of the flame at dry operation.

For local as well as global measurements, the exhaust gas sample is extracted from the combustion chamber with a water-cooled probe. This probe is made of alloy steel and has an outer diameter of 7 mm and an intake opening of 1.5 mm. The cooling water temperature at the inlet is regulated to 353 K in order to quench the combustion reaction quickly. As the cooling water temperature is well below the boiling point, evaporation of the cooling water in the probe can effectively be prevented. Furthermore, condensation of the water in the exhaust gas is effectively reduced due to the use of preheated cooling water. Via a heated tube a pump transports the exhaust gas sample to the analyzer. In the gas analyzer system the gas sample is divided into two identical parts. CO, CO_2 and O_2 are measured in the dry exhaust gas while the NO_x content is determined in the wet exhaust gas. The first three components are measured with a continuous ABB Advance Optima 2000 gas analyzer. A MAGNOS 206 detector measures the oxygen content in the gas sample with a measurement uncertainty of ±0.1 vol-%. An URAS 14 module determines the content of CO and CO_2. While the measurement uncertainty for CO_2 measurements is ±0.1 vol-%, an uncertainty between 0.5 ppm and 7.5 ppm is stated for local and global CO measurements. For the determination of nitrogen oxide concentrations an ECOphysics CLD700EL-ht analyzer module is used. This module measures NO concentrations in the humid exhaust gas with an accuracy of ±0.1 ppm. Furthermore, with the help of a catalytic conversion reactor, the concentration of NO_2 can be measured. For all measurements, data is collected electronically for a measurement time of 30 s. Afterwards, this measured data is post-processed using Matlab. First, the measured values are averaged over time to compensate turbulent fluctuations in the main flow. Area-averaged concentration values at an axial distance of 470 mm from the combustion chamber inlet are used as global species concentration values. In a second step, the global NO_x as well as CO values are normalized to 15 vol-% O_2 in the dry exhaust gas. Finally, the locally measured concentration values are used to calculate a distribution of the reaction progress variable in the combustor. This reaction progress variable is calculated using a balance of the C atoms in the gaseous mixture. In the reactant mixture all C atoms are bound in the fuel molecules. Assuming a complete conversion of the fuel molecules all C atoms are bound in CO and CO_2 molecules in the product mixture. At stationary operating conditions of the test rig the reaction progress variable is calculated from a ratio of the converted C atoms to the total amount of C atoms in the gas mixture:

$$c = \frac{[\mathrm{CO_2}]_{\mathrm{meas}} + [\mathrm{CO}]_{\mathrm{meas}}}{[\mathrm{CO_2}]_{\mathrm{eq}} + [\mathrm{CO}]_{\mathrm{eq}}} \tag{4.5}$$

In this equation, values with the subscript *meas* symbolize measured values, while values with the subscript *eq* denote equilibrium concentrations at the given operating condition. The equilibrium concentrations are calculated numerically using Cantera equilibrium calculations and the mass flow rates from the test rig. The Cantera simulations are introduced in section 4.3.

4.2.2 Liquid Phase

Besides the analysis of the gas phase, further investigations focus on the characterization of the liquid phase in the combustor. Especially the water distribution in the test rig as well as the droplet size distributions of the spray are of great interest.

Mie Scattering Investigations

Mie scattering investigations are employed to measure the qualitative distribution of the water droplets in the combustor centerplane. Due to the shape of the droplets, laser light is scattered which makes the droplets visible. As shown in Mie theory [51], a complex interaction of the incident light and the droplets forms. Amongst others, the intensity of the scattered light depends on the diameter of the droplets, the scattering angle as well as the wavelength of the laser light. As no exact calibration point for the droplet size is available in the measurements, the results are at a qualitative level only. Consequently, this method allows to extract differences in scattered laser intensity between various operating points of the test rig.

In order to determine the influence of the flame on the water distribution, all measurements are conducted for reacting operation of the test rig. The measurement configuration for the Mie scattering investigations consists of a thin laser sheet and a high-speed camera. For the generation of the laser sheet a Litron LDY304 Nd:Ylf laser system with two laser cavities is used. This laser has an output wavelength of 527 nm at high optical powers and high repetition rates. For the investigations in this thesis, the repetition rate is set to 10 kHz at a laser pulse length of 150 ns. Using laser mirrors, a concave lens (f=-25.4 mm) and a biconvex lens (f=500 mm) a lasersheet is formed. This lasersheet has a length of 100 mm and a thickness of 0.5 mm. In order to visualize the distribution of the water droplets in the combustor centerplane, the lasersheet is positioned accordingly. Similar to the OH* chemiluminescence measurements, a Photron SAX high-speed camera and a f=200 mm lens is used to capture the distribution of the Mie intensity. In order to separate the intensity of the scattered laser beam from the ambient light, an optical filter with a wavelength of 531±5 nm is positioned in front of the camera. For each operating point 4000 images are recorded at a frequency of 10000 frames per second.

In order to eliminate unwanted reflections originating from the lasersheet, a two step approach is used. On the one hand, the back part of the glass combustion chamber is coated with thermoresistant black color. This coating effectively reduces the intensity of most reflections. On the other hand, all images are post-processed in Matlab: First, a background image is subtracted from each image. In a second step, a high-pass filter is applied to reduce the image noise. Finally, the images at each operating point are averaged to compensate for turbulent fluctuations in the main flow. The resulting images illustrate the spatial distribution of the droplet Mie scattering in the combustion chamber.

Particle Sizing

In order to get insight into the microscopic parameters of the water spray, volumetric particle size distributions are measured with an industrial Malvern particle sizer. This device operates based on the principle of diffraction of parallel laser light [15]. In the measurement configuration, shown in Fig. 4.6, a beam of parallel laser light illuminates the spray at a certain measurement position. Depending on the size of the droplets as well as the refractive index of the medium, the parallel laser light is diffracted. A Fourier lens focuses the diffracted light onto a concentrically arranged array of detectors. The detectors measure the intensity of the diffracted light and an internal data processor calculates a particle size distribution of the spray. Advantages of this measurement technique are its easy applicability as well as its robustness. Due to the characteristics of the measurement technique, all particles along the beampath of the laser are taken into consideration for the calculation of the droplet size distribution. Consequently, the measurement technique delivers line-of-sight integrated results.

For simplicity, the measurements are conducted in an external spray test rig for a wide range of nozzle operating conditions. In order to separate the ef-

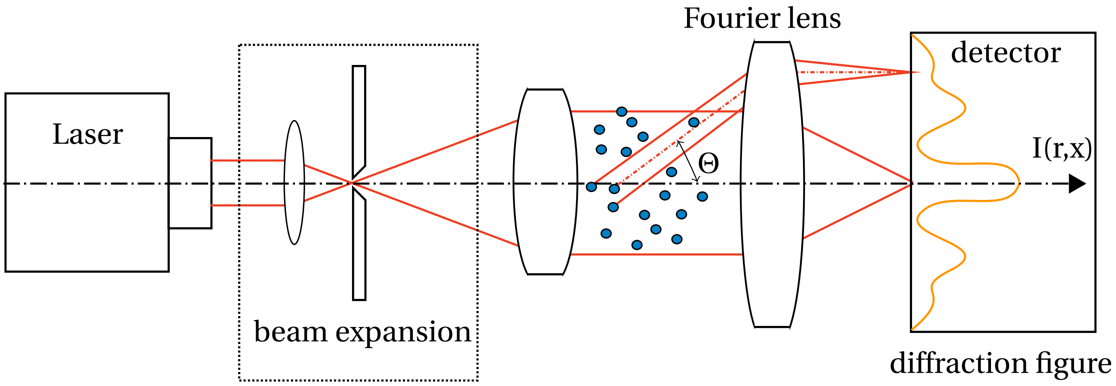

Figure 4.6: Schematic of a laser diffraction particle sizer [66].

fects of the nozzle from influences of the main flow in the test rig, the nozzle is investigated in quiescent ambient air. Identical nozzle geometries are used in the spray test rig and in the combustion test rig. In post-processing, measurement errors at very low particle sizes are corrected and the size distributions are averaged over a time of 30 s to eliminate instationary effects. In order to quickly analyze the quality of a droplet size distribution, two representative diameters are calculated according to the formulas in section 2.1.3. In this thesis, the Sauter mean diameter or $d_{V,32}$ and the $d_{V,90}$ are used to characterize the spray distribution.

4.3 Reaction Kinetic Simulations in Cantera

In order to gain deeper insight into the combustion phenomena at wet operation, reaction kinetic simulations were conducted in addition to the experimental investigations. These investigations were performed with the open source tool Cantera [29] and the GRI reaction mechanism version 3.0 [72]. The GRI mechanism has been validated for a wide range of gas turbine operating conditions. Additionally, as shown by Göke and Göckeler, this version of the GRI mechanism is well suited for reaction kinetic calculations at wet operating conditions [25, 27]. The simulations as well as the post-processing of the data is carried out in Python. Three different investigations are performed:

- Determination of the equilibrium concentration.

- Determination of the laminar flame speed.
- Calculation of CO concentrations at diabatic operating conditions.

For the calculation of the reaction progress from local species concentrations, equilibrium values of given fuel-air-water mixtures are necessary. These values are extracted from adiabatic Cantera equilibrium calculations. Additionally, laminar flame speeds at dry and wet operating conditions are required to correlate flame position data with the mixture reactivity (see section 5.1). To obtain this data, one dimensional free flame calculations are performed in Cantera. This one dimensional approach assumes a homogeneous mixture of fuel, air and water which represents a simplification of the situation in the combustion chamber. However, as the flame speed data is used for a global correlation, this simplification is justified. The composition of the reactants is chosen according to the mass flow values at the corresponding operating point in the test rig. In these simulations, the liquid water is treated as gaseous water. To account for the heat needed for the evaporation of the droplets, the inlet temperature of the reactants is reduced. The reduced inlet temperature is determined from an energy balance of the gaseous reactants as well as the liquid water. Finally, s_{L}^{0} can be determined for a wide range of dry and wet operating conditions.

In order to analyze the CO formation in the test rig, additional equilibrium calculations at diabatic operating conditions are performed. To adapt the numerically determined CO concentrations to the experimental data, different heat losses are introduced into the adiabatic Cantera simulations. For a better understanding, the calculation process and the different heat losses are presented in Fig. 4.7. Generally, the composition of the reactants is chosen according to the mass flow rates in the test rig at the given operating point. Liquid water is treated as steam. At first, the CO equilibrium concentrations are determined at adiabatic operation for different levels of steam injection. The results of these calculations are shown as a continuous blue line in Fig. 4.7. In a second step, the CO equilibrium concentrations at adiabatic operating conditions are calculated for points with water injection. Similar to the free flame calculations described above, the temperature of the reactants is adjusted to represent the enthalpy difference $\Delta \mathrm{h}_{\mathrm{vap}}$ due to the evaporation of

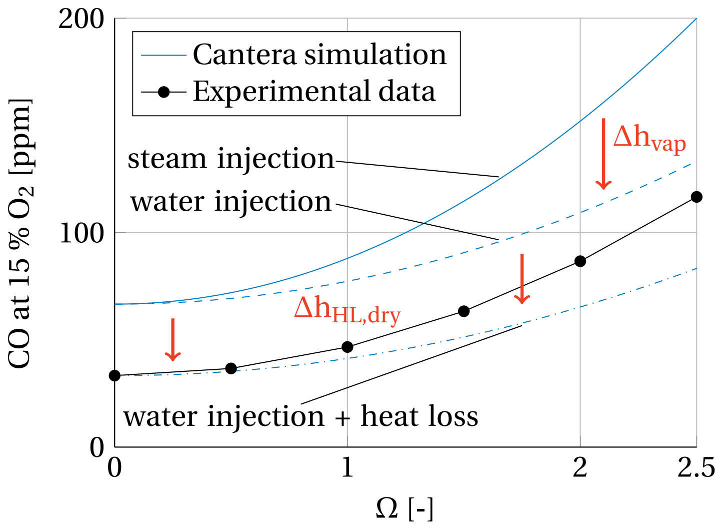

Figure 4.7: Schematic of the different enthalpy levels for the diabatic equilibrium calculations.

the water. In Fig. 4.7 the CO equilibrium values at changed reactant temperatures are shown by the dashed blue line. With increasing Ω the heat loss due to the evaporation of the water increases. Consequently, a higher value of Δh_{vap} is applied to the adiabatic simulation which lowers the CO equilibrium values. To account for the losses due to the non-adiabatic setup of the test rig, a second heat loss $\Delta h_{HL,dry}$ is added to the equilibrium calculations. This heat loss is determined iteratively. At first, the CO concentration in the dry exhaust gas is determined from a Cantera equilibrium calculation. In a second step, the CO concentration at dry operating conditions from the Cantera simulation is adjusted to the measured global CO concentration from the test rig measurements. This is done by adding an additional heat loss. Subsequently, this additional heat loss at dry operating conditions is transferred to measurements at wet operating conditions. It is assumed that the heat losses are constant within the measurement series. Finally, the equilibrium CO concentration at diabatic operating conditions is accessible. In the analysis of the gas composition measurements, this allows to separate CO concentrations related to the chemical equilibrium from CO originating from quenching processes. In Fig. 4.7 the diabatic CO concentrations at wet operation are shown by the blue dot-and-dashed line, while experimental CO values are marked with a solid black line. Differences between these two lines show the contribution of CO originating from quenching processes.

5 Global Characterization of Premixed Water Injected Flames

After the thermodynamic analysis in chapter 3 investigations now focus on the specific effects of water addition on the combustion reaction. Due to the novelty of water injection in premixed flames, a global characterization of the system is carried out first. In this context, dry and wet operating points are studied with optical measurement methods. At first, OH* chemiluminescence images are presented for a wide range of operating conditions. Water to fuel ratio, equivalence ratio and adiabatic flame temperature are changed in order to get an overview of the system's operating range. Thereby, the OH* images are used to visualize the influence of water addition on the heat release distribution of the flame. Using laminar flame speed data from Cantera calculations, a correlation for the flame position at wet conditions is derived. In a second step, the liquid phase is characterized with Mie scattering investigations to determine the distribution of water droplets in the combustor. Finally, a combination of the OH* data with the Mie scattering results reveals the interaction of the heat release with the water spray.

All experimental investigations in this chapter are carried out for a test rig setup with nozzle configuration C1[1] and an atomizing air mass flow rate of $\dot{m}_{\mathrm{a,at}}$=3.5 g/s.

5.1 Heat Release in the Combustion Chamber

Figure 5.1 shows OH* chemiluminescence images of the flame at typical operating conditions. Each row of images symbolizes a series of measurements

---

[1] See section 4.1.2 for further information on the different nozzle configurations.

at constant Φ. Additionally, the equivalence ratio is reduced from the top to the bottom row thereby decreasing the adiabatic flame temperature. Starting from dry operation at the left, the amount of water in the combustor is increased from left to right. To show the physical effect of water injection, the calculated adiabatic flame temperature at each operating point is given above the corresponding image.

For dry operation at $\Phi=0.714$, a compact, well stabilized flame is found. The flame is positioned close to the inlet of the combustion chamber and the main intensity of the OH* distribution is located at around 60 mm. The combustion reaction takes place mainly in the inner shear layer whereas no significant OH* intensity can be found in the outer recirculation zone. For images at increasing equivalence ratio, an extension as well as a downstream shift of the reaction zone is found. Due to the lower flame temperature, the reactivity of the fuel air mixture is decreased which influences the position of the reaction zone in the combustor. Similar effects as for a decrease in Φ can also be found for cases with water addition. Starting from an OH* image on the left, the adiabatic flame temperature and the reactivity of the mixture decrease leading to an extension as well as a downstream shift of the heat release zone. Furthermore, a rising asymmetry of the flame images can be found for increasing water contents which might be caused by an inhomogeneity of the droplet distribution in the combustor.

The dominant effect of the adiabatic flame temperature on the position and shape of the heat release zone can be found when comparing measurements at different equivalence ratios. As long as the flame temperature is high enough, the effects of water addition on the flame are moderate. This can be seen especially for the measurements series at $\Phi=0.714$. The flame shape remains compact even for an Ω value of unity and the position of the flame stays within a range of 80 mm downstream of the burner outlet. However, a stronger effect of water addition is found for lower values of Φ. Especially for adiabatic flame temperatures of 1800 K and below, the volume of the reaction zone increases significantly indicating that the reaction zone is not compact anymore. A widely distributed reaction zone forms in which the main OH* intensity is located at axial distances of 100 mm and above.

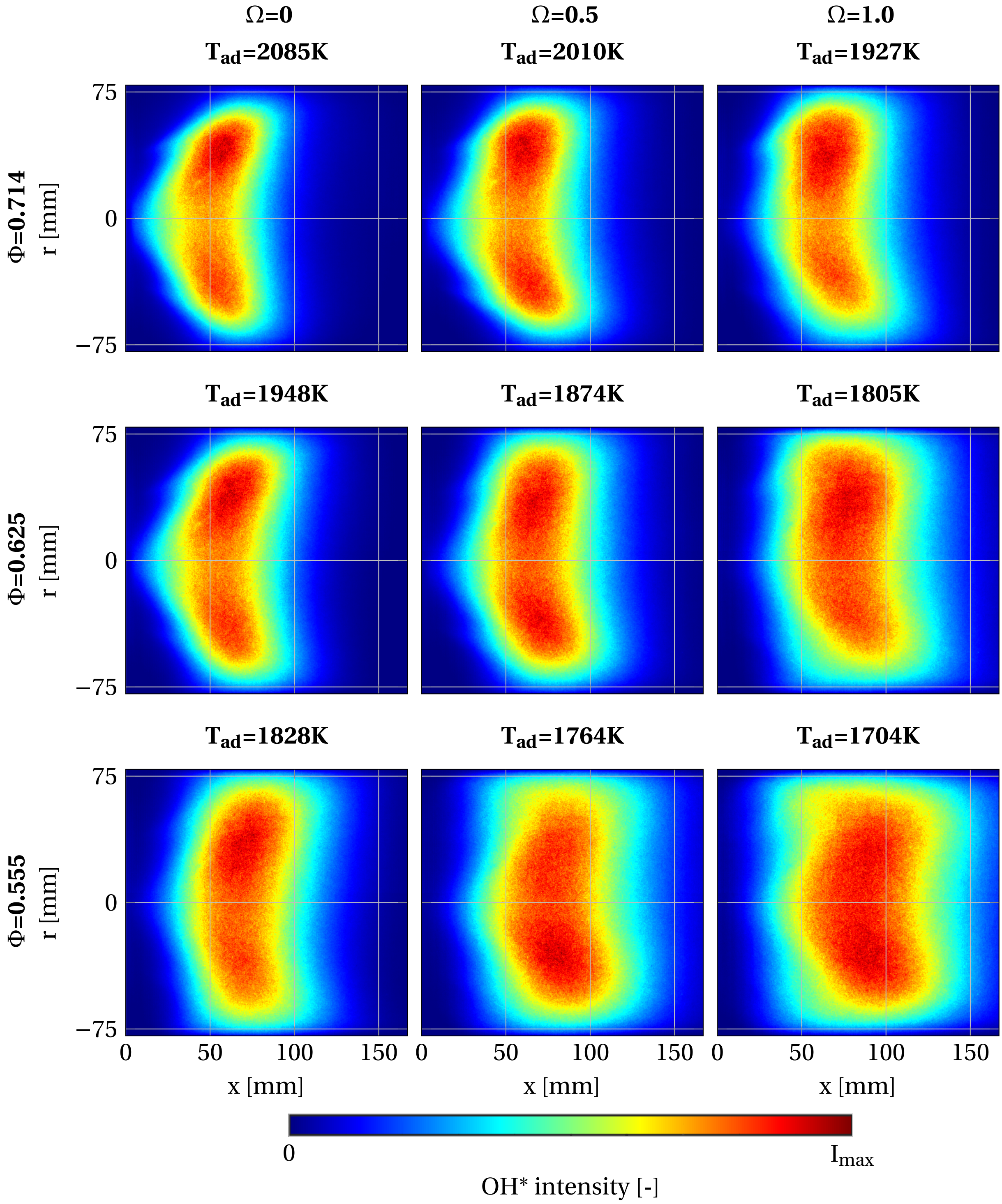

Figure 5.1: OH* chemiluminescence images for nozzle configuration C1 at constant equivalence ratio.

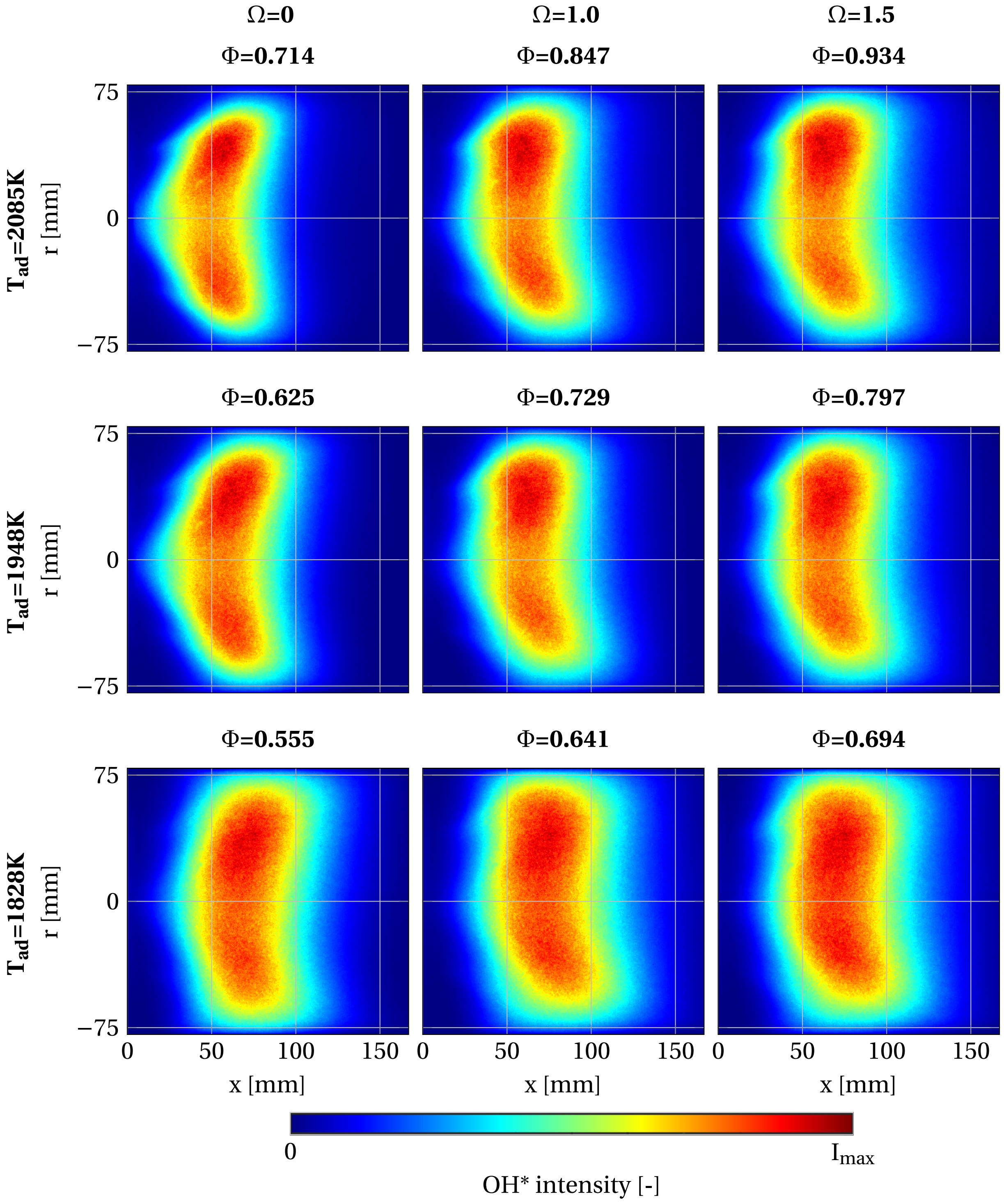

Figure 5.2: OH* chemiluminescence images for nozzle configuration C1 at constant T_{ad}.

The similar effects of water injection and equivalence ratio reduction show the strong influence of the flame temperature on the heat release distribution of the flame. In order to separate the effects of flame temperature reduction and water injection from each other, a second series of measurements is conducted at constant adiabatic flame temperatures. The OH* distributions in Fig. 5.2 show three series of measurements at different levels of T_{ad}. In each column, the adiabatic flame temperature decreases from top to bottom, whereas the Ω values rise from left to right. Compared to the results in Fig. 5.1, the influence of water addition is significantly lower. Although qualitatively similar effects of water addition can be found, changes within a measurement series at constant T_{ad} are smaller compared to operation at constant Φ. Independent of the exact temperature level in the combustor, a downstream shift of the flame as well as a minor extension of the heat release zone are determined for rising water contents. Similar as for operation at constant Φ, the flame shape in general is more compact at higher adiabatic flame temperatures. However, in contrast to the results for constant Φ, a compact heat release zone can be guaranteed for all investigated cases. Furthermore, the influence on the position of maximum OH* intensity is reduced which is beneficial for operation in modern gas turbines where the length of the combustion chamber is limited.

After this qualitative analysis of the flame shape, typical flame properties are now investigated quantitatively. Figure 5.3a shows the influence of water injection on the position of the center of OH* intensity and Fig. 5.3b on the flamelength. In order to identify the changes due to water addition, the values are normalized to dry operating conditions for each measurement series. Both parameters show a gradual increase over Ω, however, for measurement series at constant equivalence ratio a larger influence of the water injection is found. For measurements at constant adiabatic flame temperature, the flamelength as well as the position of the center of OH* intensity increase by about 10 % at Ω=1 whereas an increase of up to 30 % is found for operation at constant Φ. As the flame temperature decreases for operation at constant Φ, a larger reduction of the mixture reactivity is found for these measurements compared to operation at constant T_{ad}. Consequently, the influence on the flame properties is stronger.

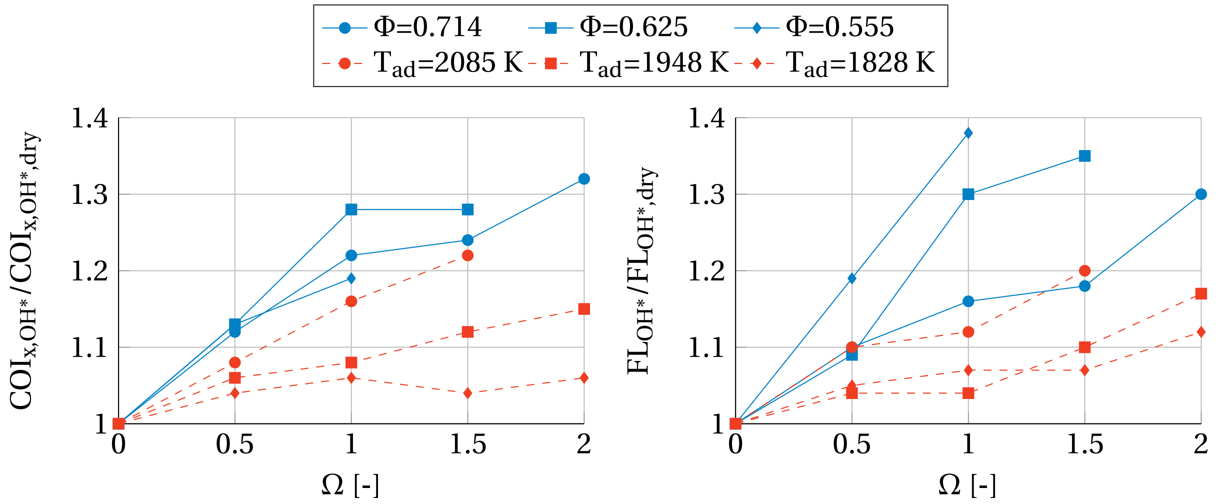

(a) Center of OH* intensity for variable Φ and Ω. **(b)** Flamelength for variable Φ and Ω.

Figure 5.3: Analysis of the flame properties for variable Ω.

Having in mind the strong influence of flame temperature and reactivity on the heat release zone, Fig. 5.4 combines the results of all measurement series at different adiabatic flame temperatures as well as different levels of water injection and links them to the mixture reactivity at the given operating point. As shown in chapter 3, the laminar flame speed s_L is a good measure for the reactivity of a mixture. However, as the flow in the test rig is highly turbulent, the turbulent flame speed s_t is suited better for this correlation. As described in section 2.2.4 the turbulent flame speed combines information about the changing mixture reactivity with turbulence data in the test rig. It is therefore well suited to describe the different influences on the combustion process in the test rig. The mixture properties for the investigated operating points are calculated from Cantera free flame simulations as described in section 4.3. In order to calculate s_t, the approach from Peters is used (see section 2.2.4). Turbulence parameters of the flow in the test rig are calculated from typical assumptions[2] as well as velocity measurements in the test rig.

Figure 5.4 reveals a correlation between s_t and the position of the center of OH* intensity. For higher values of s_t all measurements collapse to a single line in the graph. However, for s_t values below 5.5 m/s no unique curve can

---

[2] Isotropic turbulence, turbulence level 15%.

be found. As shown in Figs. 5.1 and 5.2, a distributed reaction zone forms for operation at low flame temperatures which significantly changes the overall shape of the flame. This alteration of the flame shape influences the flame length as well as the position of the center of OH* intensity. In order to include information about the different flame shapes into the curve in Fig. 5.4, an additional parameter has to be included. A closer look at the OH* chemiluminescence images in Figs. 5.1 and 5.2 reveals three different flame types. For T_{ad}=1900 K and higher a highly symmetric flame with a typical V-shape forms. At flame temperatures between 1800 K and 1900 K this flame shape alters. The high level of symmetry decreases and the V-shape changes to a flat flame shape. A third characteristic flame shape is found for adiabatic flame temperatures below 1800 K. The flame extends further downstream forming a widely distributed reaction zone in the combustion chamber.

A transfer of this flame shape information into Fig. 5.4 clearly separates three regions in the diagram. At adiabatic flame temperatures of 1900 K and higher, the values of COI_{x,OH^*} are low. A linear relation between the position of the center of OH* intensity and the turbulent flame speed can be found over a wide range of s_t. As described above, the flame shape changes for adiabatic flame temperatures between 1800 K and 1900 K. In Fig. 5.4, this effect is described with a shift of the curve to higher axial COI positions. Due to the decreased stability of the flame at lower temperatures as well as the low amount of measurement points, the correlation between the position of the COI and s_t is less certain as for T_{ad}>1900 K. Still, a similar linear relation can be found. Finally, a further reduction of the adiabatic flame temperature allows to identify a third set of measurements. This data set is characterized by a low amount of measurement points as well as a high fluctuation within the data. Consequently, no clear relation can be found between the position of the COI and s_t. However, due to the low reactivity at the lower flame temperatures, all operating points show very high values of the axial COI position. An interpolated curve shows the trend of the COI for this flame shape. In conclusion, stable operation of water injection in premixed natural gas flames is demonstrated for a wide range of operating conditions. The analysis of the OH* chemiluminescence images as well as the derived variables allows to analyze the effect of water addition on the global heat release in the flame. According to the measurements,

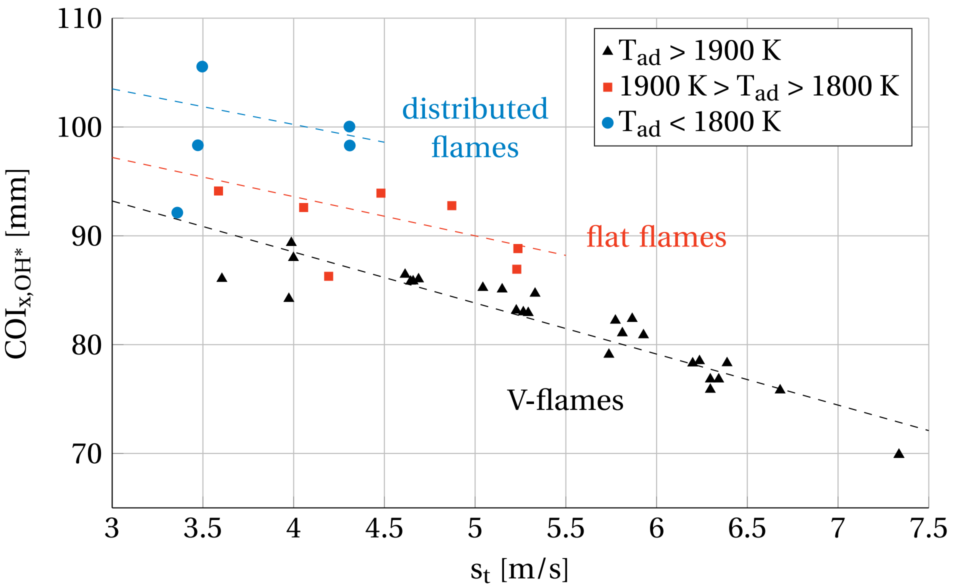

Figure 5.4: Correlation of the Center of OH* intensity with s_t at different levels of T_{ad}.

the physical effect of water addition is dominant. This means that the reduction of the adiabatic flame temperature due to the water addition governs the OH* chemiluminescence distribution. Furthermore, this indicates that the reactivity of a mixture is mainly determined by the corresponding flame speed, independent of the water concentration in the mixture. Due to the complexity of the investigated combustor configuration as well as the dominant physical effect of water injection, no influence on the global heat release distribution apart from the physical influence of water addition is found. In particular, it is not possible to identify any chemical effect.

5.2 Water Distribution in the Combustion Chamber

Besides the determination of the heat release distribution in the combustor, the water phase also has to be taken into consideration. In order to identify the effects of water injection on the flame, it is important to determine the distribution of the water droplets in the combustion chamber. The droplets are identified with time-resolved Mie scattering imaging. To eliminate turbulence effects in the main flow, the captured images are averaged over time. Figure 5.5 shows these time-averaged distributions of the Mie intensity in the combustor for a series of measurements at constant T_{ad} and constant atomizing air mass flow rate. Due to the positioning of the laser sheet, no Mie scattering data is obtained for axial distances lower than 2 mm. The investigations were conducted under reacting conditions in the lab scale combustor. The captured images show the Mie scattering intensity in the upper half of the combustion chamber close to the inlet. In all images the main flow is directed from left to right. Similarly, the amount of water increases from the image on the left to the one on the right. Due to the complex dependencies of Mie scattering intensity on droplet diameter, droplet density as well as scattering angle a calculation of the droplet sizes in the combustion chamber is not possible. Nevertheless, given certain assumptions, a quantitative comparison of the images at different Ω is possible. As the spatial distributions were determined at similar measurement conditions, influences on the measurement technique are assumed to be negligible. Furthermore, the droplet size distributions at the investigated operating points are relatively similar. Therefore, the Mie scattering intensities at these different operating points are expected to be similar as well. Assuming a constant Mie scattering intensity for droplets with different sizes, Mie scattering intensity and water droplet density are coupled proportionally. Consequently, higher water droplet densities are found at locations with higher Mie intensities.

A first look at the images in Fig. 5.5 shows large differences in the absolute intensities for different Ω values. For operation at low Ω, the overall droplet Mie scattering is low. However, with increasing water to fuel ratio the Mie intensity in the images rises. This fact shows the increasing number of droplets with increasing water content. Besides this difference, a closer investigation of the images in Fig. 5.5 reveals a high similarity of the droplet distributions in all images independent of the absolute value of Ω. Generally, the highest Mie intensities are found close to the inlet of the combustor at low radial distances from the symmetry axis. Independent of Ω droplets are located between radial distances of 5 and 40 mm with highest intensities around 20 mm. At the inlet of

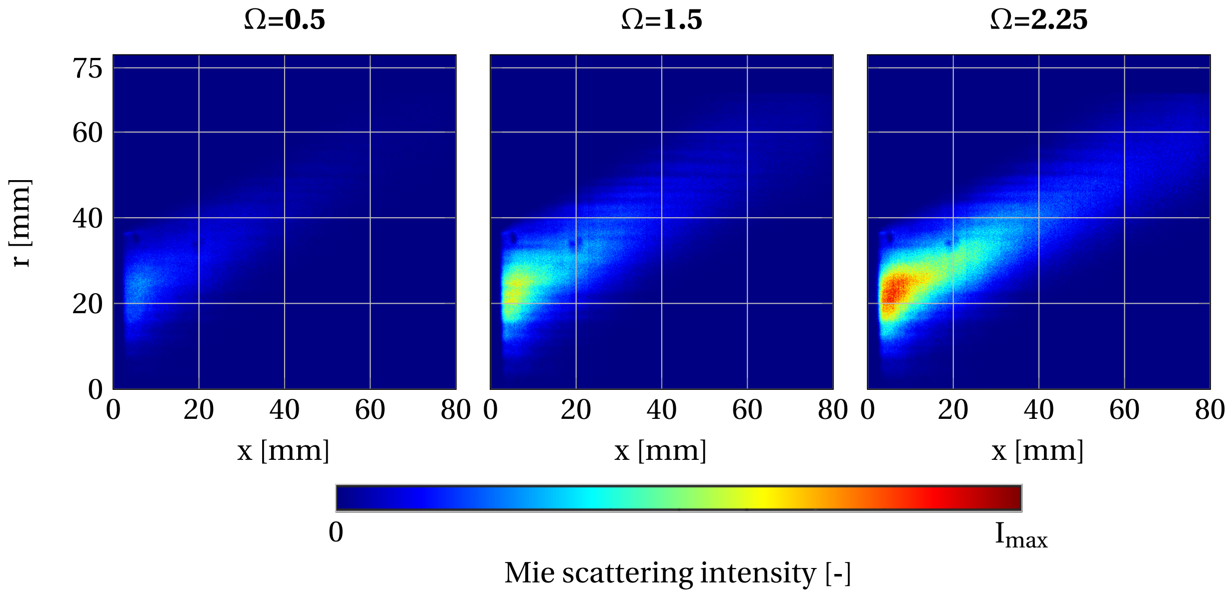

Figure 5.5: Particle density distribution in the combustion chamber at $\dot{m}_{a,at}$=3.5 g/s and T_{ad}=1948K.

the combustor a full cone structure of the water spray is observed. This means, that droplets are distributed over the complete outlet area of the mixing tube. With increasing axial distances the local droplet Mie scattering decreases and the maximum intensities shift to higher radii. This clearly shows the continuous evaporation of the droplets. Due to the intense interactions of the spray with the flame, the number of droplets drops. While the evaporation of the droplets at Ω=0.5 is completed within a short distance from the combustor inlet, droplets are advancing to higher axial distances for increased Ω. This effect continues until a significant concentration of droplets close to the wall is found for operation at Ω=2.25. Additional observations in the test rig have shown that water droplets reach the combustor wall for water to fuel ratios higher than 2.25 . Due to the high wall temperatures, these droplets evaporate instantaneously thereby creating high local water concentrations in the gas phase. In order to avoid damage to the test rig from droplets impacting at the combustor walls, no investigations at Ω values larger than 2.25 are conducted.

Figure 5.5 also reveals additional information about the radial position of the droplets in the combustor. At higher axial positions the structure of the spray changes and a hollow cone of droplets develops. While no droplets are found

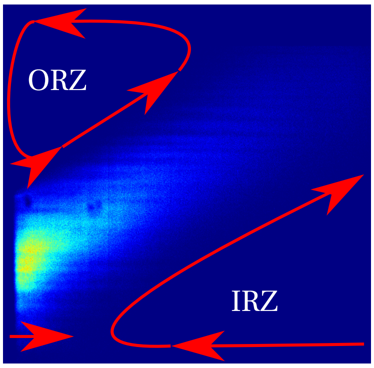

Figure 5.6: Scheme of the spray distribution in the combustion chamber.

in the center of the combustion chamber, the main Mie intensities are located within a small radial range at higher radial distances. This characteristic shape of the droplet distribution is influenced by three different effects. First, this typical spray structure is related to the flow field of the water nozzle. The air blast atomizer forms the spray and accelerates the droplets strongly in axial as well as radial direction. Consequently, a spray cone forms which determines the distribution of the droplets in the combustor. Secondly, the droplet distribution is related to the main flow structure in the combustor. For a better understanding, this flow structure is shown in Fig. 5.6. The vortex break-down in the main flow forms an inner recirculation zone (IRZ) close to the inlet. As a result, the streamlines of the main flow are deflected outward. This characteristic flow field changes the motion of the smaller droplets in the spray. Due to the low momentum of the small droplets these droplets follow the main flow along the streamlines, which increases the droplet Mie scattering at higher radii. The interaction of the spray with the outer recirculation zone (ORZ) is negligible because of the high axial momentum of the droplets. Besides this, the absence of droplets in the center of the combustor at higher axial distances is also related to the effect of the flame in the combustor. Due to the high heat release in the center of the combustor, the highest temperatures in the combustor are found here. Consequently, the evaporation of the droplets is increased locally. More details on the effect of the flame on the spray distribution will be presented in section 5.3.

In order to compare absolute values of the Mie intensity at different Ω values, the intensities in the images are integrated over the radius. Figure 5.7 shows

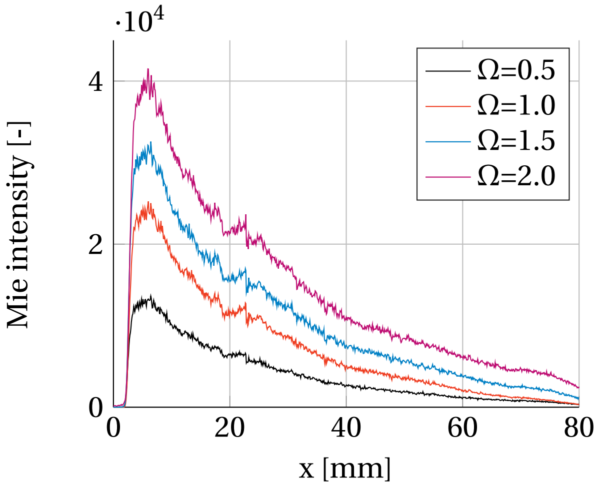

Figure 5.7: Integral Mie intensity in the combustion chamber.

the integral Mie intensity over the axial distance in the combustion chamber. A comparison of the Mie intensity between four different operating points reveals a high similarity between the curves as well as an increasing Mie intensity with rising water-to-fuel ratio. This fact has already been shown qualitatively in Fig. 5.5. Due to the rising water content in the combustor, the concentration of droplets increases which directly influences the Mie scattering of the laser light. Over a wide range of axial distances the Mie scattering intensity scales almost linear with Ω. As the droplet size distributions for different water-to-fuel ratios are relatively similar (see section 6.3.1) an increase of the Mie scattering intensity can directly be related to higher droplet densities in the combustor. Generally, higher Mie intensities are found at lower axial distances in the combustor while lower values occur farther downstream. Independent of Ω, a maximum of the Mie intensity is found at an axial distance of 5 mm of the measurement domain (see Fig. 5.7). Due to the high ambient temperatures in the combustion chamber, evaporation of the droplets occurs. Consequently, the Mie intensity drops within a short distance from the combustor inlet. For Ω=0.5 the Mie intensity is cut in half at an axial distance of 25 mm. Similar developments are found for higher water-to-fuel ratios, too. For Ω=0.5 and axial distances of 60 mm and higher the Mie intensity remains almost constant. Due to the low values of the droplet density non-linear effects of Mie scattering might occur, thereby influencing the measurement results. Nevertheless, as the measured Mie intensities are low, complete evap-

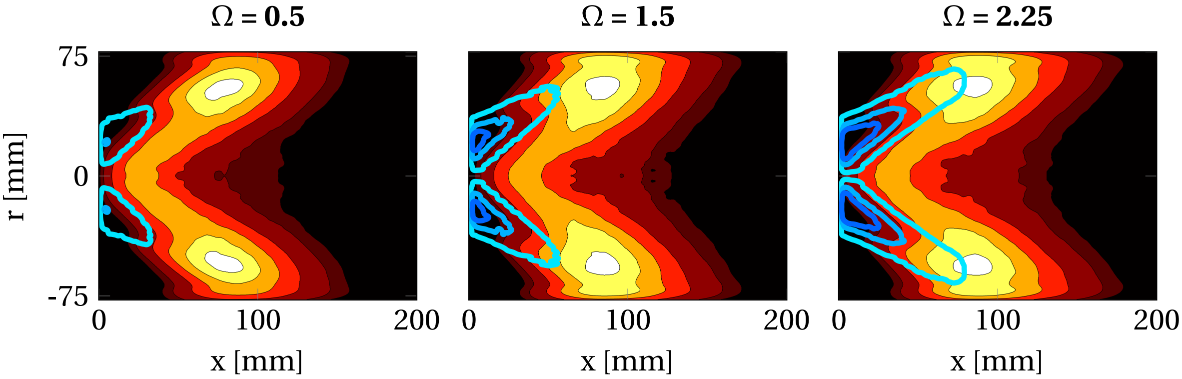

Figure 5.8: Combined plot of OH* chemiluminescence and droplet Mie scattering intensity in the combustion chamber at $\dot{m}_{a,at}$=3.5 g/s and T_{ad}=1948K.

oration of the water droplets can be assumed for axial distances higher than 60 mm. Due to the higher droplet densities at higher water contents, complete evaporation of the droplets is not possible as quickly as for operation at low Ω. Although the decrease of the Mie intensity is stronger at higher water contents compared to low water contents, a Mie intensity above zero is detected at x=80 mm for Ω=1.5 and above. This fact also corresponds to the findings in Fig. 5.5. At higher Ω values droplets can advance to higher axial distances in the combustor leading to increased Mie scattering there.

5.3 Interaction of Heat Release with the Spray

In order to clarify the influence of water droplets on the heat release distribution and vice versa, OH* measurements from section 5.1 as well as Mie scattering intensities from section 5.2 are combined. Starting from the images in Fig. 5.6, OH* intensities in the combustor centerplane are determined with an Abel inversion algorithm. Figure 5.8 shows OH* intensities as contours in red and yellow colors. Furthermore, isocontour lines of different droplet Mie scattering intensities are shown in the same graph using blue colors. Starting from low water content in the image on the left, Ω is increased stepwise from left to right. During the measurements the adiabatic flame temperature is held constant.

For Ω=0.5 the overlap between the two distributions is very small. Water droplets are mainly found close to the inlet of the combustor, whereas the flame is located at higher axial distances. As already described above, no droplets are found in the center of the combustor at higher axial positions. Besides the reasons described above, this droplet distribution is related to the shape of the heat release zone, with an inner recirculation zone close to the combustor inlet. The inner contour of the droplet Mie scattering isoline shows an inverse distribution compared to the heat release distribution in the inner recirculation zone. At this operating point, the droplet distribution clearly adapts to the heat release distribution in the combustor. With increasing axial distances the Mie intensity drops quickly due to evaporation. Additionally, Fig. 5.8 shows that evaporation is complete before the main part of the heat release zone begins.

However, for increasing Ω this situation changes. Due to the higher droplet densities at increased water contents, droplets advance further into the combustion chamber. As the downstream shift of the heat release zone is small, the overlap between the zones of high droplet Mie scattering and the heat release zone grows. Close to the inlet of the combustor a similar situation as for low water contents is found. Zones of high Mie intensity alternate with zones of high heat release. The isolines of the droplet Mie scattering adapt to the shape of the inner recirculation zone, however, due to the increased droplet densities evaporation of the water is not completed as quickly as for operation at Ω=0.5. Consequently, droplets advance to regions with high heat release at r=50 mm.

For operation at very high water contents droplets advance even further into these zones with high heat release. Although almost no overlap of the distributions is found at lower axial distances, evaporation of the droplets is not fast enough, which leads to significant droplet densities in the main flame zone. Due to the very high temperatures in the main combustion zone, droplets evaporate quickly there, leading to high local water concentrations. As the result, increased effects of water injection can be found at higher radii for these operating points. Observations for Ω values higher than 2.25 have shown droplets hitting the combustor walls. These droplets bypass the main reaction zone in the combustor and reduce the effectiveness of water injection. As the evaporation of the droplets is incomplete, the temperature reduction due to water addition is lower and higher local flame temperatures are found in the combustor. Consequently, the inhomogeneity in the combustor rises and chemical reactions as well as pollutant formation processes are influenced (see chapter 6). Figure 5.8 shows in general that the local heat release distribution adapts to the increased water content in the combustor. The reactivity of the mixture drops, thereby shifting the heat release zone downstream and closer to the wall. This in turn gives room for the evaporation of the droplets. However, as the diameter of the combustion chamber is limited, heat release increasingly interacts with the combustor walls. Consequently, the displacement of the flame is limited and the overlap of the water droplet distribution and the heat release distribution increases. Finally, when the overlap between the two distributions is high, the interaction of heat release and droplet evaporation increases. This creates locally inhomogeneous water distributions in the combustion chamber and influences pollutant formation (see chapter 6).

6 Pollutant Formation in Water Injected Premixed Flames

This chapter shows the influence of water injection on pollutant formation in a lab scale combustor. At first, global concentration measurements focus on CO as well as NO_x formation for different operating conditions. Furthermore, global CO formation is investigated numerically using one dimensional reaction kinetic simulations. Subsequently, local species concentration measurements clarify the pollutant formation under wet conditions in greater detail. Spatial distributions of the reaction progress variable as well as detailed CO concentration measurements are used to identify local quenching phenomena in the combustor. Finally, the dominating influence of the water droplet size on pollutant formation is shown based on droplet sizing results as well as global pollutant concentration measurements.

6.1 Global Pollutant Concentrations

6.1.1 NO_x Formation

At first, the influence of water injection on global NO_x concentrations is investigated for nozzle configuration C1[1]. Figure 6.1 shows NO_x concentrations for rising Ω while Fig. 6.2 exhibits the effect of changing equivalence ratio. The measurement position for all measurements is located on the burner axis, 470 mm downstream of the combustor inlet. This location correlates to a combustor residence time of 20 ms for dry operation, which is a common timescale in industrial premixed gas turbine burners. All measurements in

---

[1] For information on the different nozzle configurations see section 4.1.2.

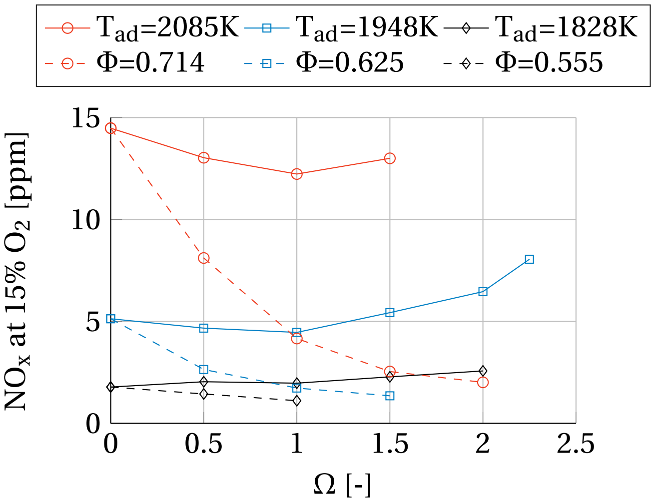

Figure 6.1: Dependency of global NO_x concentrations on Ω.

section 6.1 are conducted at an atomizing air mass flow rate of $\dot{m}_{a,at}$ of 3.5 g/s. In order to compare the measured values with each other, all concentrations are normalized to 15% O_2 in the dry exhaust gas.

Figure 6.1 shows the global NO_x concentrations over Ω at different temperature levels. The solid lines represent measurement series at constant adiabatic flame temperature, whereas measurements at constant Φ are represented with dashed lines. Independent of Ω a significant influence of the flame temperature on the overall NO_x level is found. The NO_x concentration of 15 ppm at dry operation and a flame temperature of 2085 K drops to 5 ppm at 1948 K and 2 ppm at 1828 K. As known from literature, NO_x formation is very sensitive to flame temperature [33]. Due to the exponential dependence of the reaction rate on temperature, NO_x formation increases quickly with rising T_{ad}.

At constant equivalence ratio, the heat capacity of the water-fuel-air mixture increases with rising water content in the reactant mixture. Consequently, the flame temperature drops and NO_x values at the combustor outlet decrease. According to Fig. 6.1, this effect increases at higher equivalence ratios. At an equivalence ratio of 0.714 and Ω=1 the NO_x concentration drops to 25 % of the value at dry operation. However, for operation at Φ=0.555 a lower reduction is found. This fact is related to the exponential dependency of the reaction rate on the mixture temperature. At high equivalence ratios the flame temperature in the combustor is high. Consequently, a reduction of the mixture temperature has a large effect on the NO formation rate. However, at lower equivalence ratios and lower flame temperatures this effect on the NO formation rate is small. For that reason, the effect of water injection on NO_x formation decreases at lower equivalence ratios.

Another important fact can be seen when comparing the operating ranges at different equivalence ratios. While operation is possible up to Ω=2 at Φ=0.714, the maximum water to fuel ratio decreases at lower equivalence ratios. For operation at constant Φ, the operating range of the test rig is limited due to droplets impacting the combustion chamber wall. As shown in section 5.2, at some point, complete evaporation is not possible anymore and water droplets impinge at the wall. This, in turn, creates high water concentrations close to the wall and reduces the effectiveness of water addition. Therefore, an optimum operation of the combustion chamber beyond these limits in not possible.

For operation at constant T_{ad}, the temperature reduction due to the water injection is compensated with additional fuel. This also influences the operating range of the combustor. At high flame temperatures, the operating range is limited due the constraint of constant flame temperature. With increasing water content, a rising temperature reduction has to be compensated. However, as an equivalence ratio of unity is reached, further addition of water can not be compensated. This limit is reached for operation at an adiabatic flame temperature of T_{ad}=2085 K and water contents higher than Ω=1.5. Due to the lower overall equivalence ratio at dry operation, this limit is shifted to values higher than Ω=2.5 for operation at an adiabatic flame temperature of T_{ad}=1948 K. At low flame temperatures, the operating range of the test rig is again limited due to the impingement of water droplets at the combustor walls. At an adiabatic flame temperature of T_{ad}=1828 K impingement occurs for water to fuel ratios of 2 and higher.

Besides effects on the operating range, the addition of supplement fuel also influences NO_x values in the combustor. For flame temperatures above 1900 K, a similar shape of the curves for different T_{ad} is found in Fig. 6.1. Again, the overall level of NO_x depends on flame temperature. Generally, two trends can be extracted from the curves: At low water to fuel ratios NO_x concentrations decrease slightly with increasing Ω values. In contrast, values are rising again at higher water to fuel ratios. At an adiabatic flame temperature of 2085 K, NO_x values are decreasing up to Ω=1 with a slight increase after this water to fuel ratio is exceeded. Nevertheless, due to the limited operating range at high flame temperatures, a reduction of the NO_x concentrations is found for all cases with water injection at this flame temperature. Similarly, NO_x concentrations drop up to water to fuel ratios of unity at T_{ad}=1948 K. Past this Ω value, NO_x concentrations are rising until the initial value is exceeded by more than 50 % at Ω=2.25.

These opposing trends in the curves can be explained with the high similarity between water and steam injection. As shown in section 3.3, Miyauchi and Göke have presented decreasing NO_x values for steam injected operation at constant T_{ad} [27, 52]. Compared to the results in Fig. 6.1, a high similarity of the results is observed. As described in section 5.3, water droplets evaporate quickly at low water contents. Therefore, a homogeneous mixture of water, fuel and air is achieved in the test rig. This homogeneous mixture is very similar to mixtures of fuel, air and steam which explains the analogy of water and steam injection at low water contents. Consequently, the flame temperature in the test rig is held constant while NO_x concentrations decrease slightly. However, this behavior changes at higher water contents. Due to the rising water content in the combustor, the influence of droplet evaporation on NO_x formation rises. At higher water contents, droplet evaporation is not completed before the beginning of the heat release zone (see section 5.3). This leads to deviations from the ideal behavior as demonstrated for steam injection. As the result, higher local flame temperatures occur and increasing NO_x values are found. Finally, effects of incomplete droplet evaporation predominate at very high Ω values and NO_x values rise above the level of dry operation. Nevertheless, as the rising NO_x concentrations are related to inhomogeneous water distribution and incomplete evaporation of the droplets, further improvements of water atomization and spray dispersion should be beneficial for reducing the nitrogen oxide emissions (see section 6.3.2).

At a low adiabatic flame temperature of 1828 K, NO_x values increase constantly

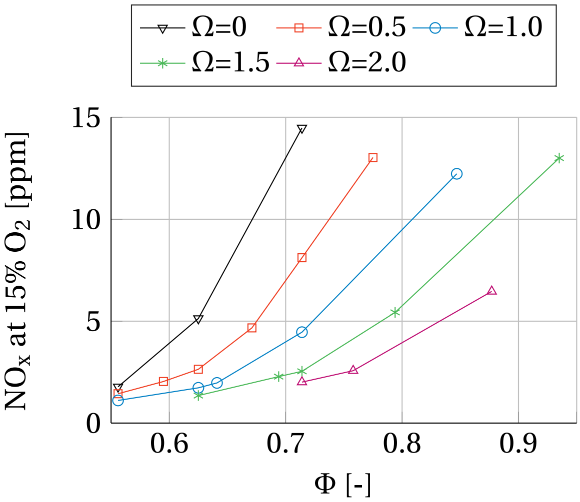

Figure 6.2: Dependency of global NO_x concentrations on Φ.

with the water to fuel ratio. However, up to Ω=1.5 this increase is very small in absolute numbers. This effect might be related to measurement uncertainties at low absolute values. For water to fuel ratios of 1.5 and higher the increase of the NO_x values is stronger. At these operating conditions the droplets are not evaporated quickly enough which leads to higher local temperatures and rising NO_x values. However, due to the low absolute level of the NO_x concentrations, the increase is moderate.

Figure 6.2 summarizes the results for NO_x formation at wet conditions. This plot includes the measurement values for all investigated cases independent of Ω. For dry operation NO_x values increase strongly with rising Φ. This effect is known from literature [33] and describes the influence of rising flame temperature. Due to the reduction of the flame temperature at constant Φ, NO_x values drop at higher water contents. Consequently, the curves for higher water contents are shifted to higher equivalence ratios in Fig. 6.2. Nevertheless, the typical shape of the NO_x curves over Φ is preserved and values are increasing steadily with rising equivalence ratios. Compared to dry operation the NO_x increase is slowed down at higher Ω which leads to smaller gradients of the curves. In terms of operating conditions, this means that the operating range of the combustor increases towards higher equivalence ratios due to water injection. Consequently, the combustor can be operated at increased Φ with higher overall power output, while holding the NO_x emissions constant.

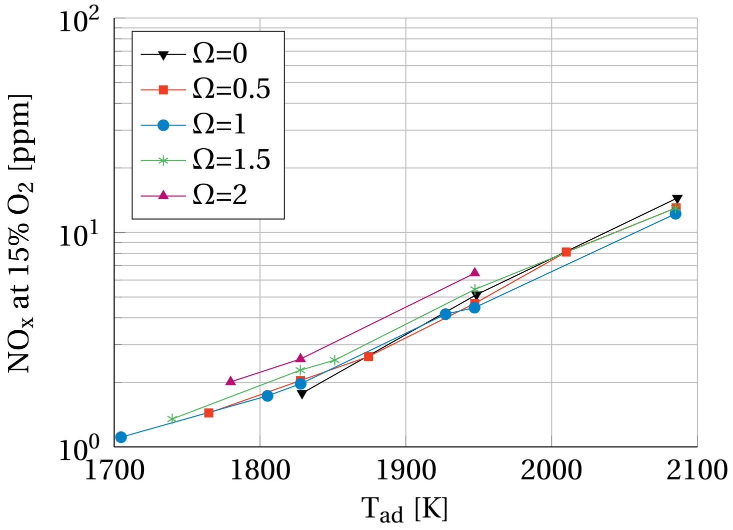

Figure 6.3: Dependency of global NO_x concentrations on T_{ad}.

As already shown in chapter 3, water injection can affect the flame either physically or chemically. In order to separate these two effects NO_x concentrations are plotted against calculated adiabatic flame temperatures in Fig. 6.3. Measurements for all cases investigated in this thesis are shown. Figure 6.3 reveals an almost logarithmic dependence of the NO_x concentration on the adiabatic flame temperature. This relation is found independent of Ω and shows the dominating influence of the adiabatic flame temperature on NO_x formation. Another important fact is that the curves for different Ω values collapse to one straight line over a wide range of T_{ad}. This clearly shows that the influence of water addition on the NO_x formation is dominated by the physical effect. No distinct chemical influence of water addition can be detected for moderate water to fuel ratios within the temperature range of 1700 K to 2100 K. Slight deviations from the linear behavior of the curves are found at low adiabatic flame temperatures. However, this fact might be related to low absolute values and high relative measurement errors at these operating points.

Additionally, discrepancies of the linear dependency between NO_x values and T_{ad} are found for higher Ω values. At Ω=1.5 and above, Fig. 6.3 shows an offset of the curve relative to the curves for lower water contents. This deviation seems to be closely related to the water distribution and the non-ideal mixing in the combustion chamber. As described above, evaporation of the water slows down and local hotspots form, thereby increasing NO_x formation in the combustor. Besides the water distribution in the combustion chamber the higher NO_x values might also be related to changes in the size of the water droplets. In order to discuss the influence of water droplet size on NO_x formation a detailed analysis is included in section 6.3 of this thesis.

In conclusion, the measurement data shows that water acts as inert diluent over a wide range of operating conditions. Given sufficient atomization of the droplets, global NO_x concentrations solely depend on the temperature level in the combustor, independent of the exact value of Ω. As already pointed out in section 3.3 statements claiming the existence of the chemical effect of water injection exist in literature [27, 41]. The results of the presented study do not confirm such statements. A chemical effect of water addition can still exist, however, due to the dominant physical effect of water addition it is not detected in the investigations in this thesis. Besides this, the complexity of the investigated flame as well as the measurement setup do not allow to separate both effects from each other.

6.1.2 CO Formation

Besides NO_x, CO is a major pollutant in gas turbine combustors. Generally, CO emissions can be split into two different types:

- CO emissions due to the chemical equilibrium.
- CO emissions originating from non-equilibrium processes.

If CO burns out completely, measured CO concentrations at the outlet correspond to the CO equilibrium concentration. However, if quenching of the reaction occurs, equilibrium is not reached and super-equilibrium CO concentrations are measured at the combustor outlet. Figures 6.4 and 6.5 show experimentally determined global CO concentrations at the combustor outlet for various operating conditions and nozzle configuration C1. Similar to the results for NO_x formation, measurement series at constant T_{ad} and constant Φ are shown for an atomizing air mass flow rate of 3.5 g/s. In order to separate

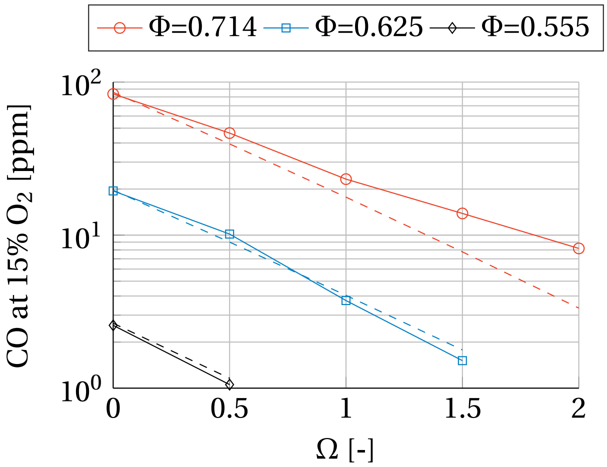

Figure 6.4: Comparison of global CO concentrations from experimental (–) and Cantera (- -) investigations at constant Φ.

CO emissions originating from non-equilibrium processes from the chemical equilibrium, numerical simulations of the CO equilibrium are included in the graphs. As described in section 4.3, these numerical calculations predict the equilibrium value of CO at the given, diabatic operating conditions in the combustor. Finally, the contributions of equilibrium and non-equilibrium CO are determined by comparing measured and calculated CO values. All values are normalized to an oxygen concentration of 15 % in the dry exhaust gas.

Figure 6.4 shows CO values for three measurement series at constant Φ. Due to the temperature dependency of the CO equilibrium concentration higher levels of CO are found for higher equivalence ratios. Independent of Φ CO concentrations decrease for rising water contents. This decline is closely related to the decreased flame temperatures at operating points with water injection. The measured CO curves show a high level of similarity with the calculated equilibrium CO concentrations. This shows that CO burns out completely over the whole operating range. However, for Φ=0.714 measured CO values lie above the equilibrium concentration at wet conditions. This effect increases at higher water to fuel ratios and shows the rising contribution of CO originating from quenching processes. Due to decreased flame temperatures at higher water contents, evaporation of the water slows down, leading to inhomogeneous water distributions in the combustor. Furthermore, due to

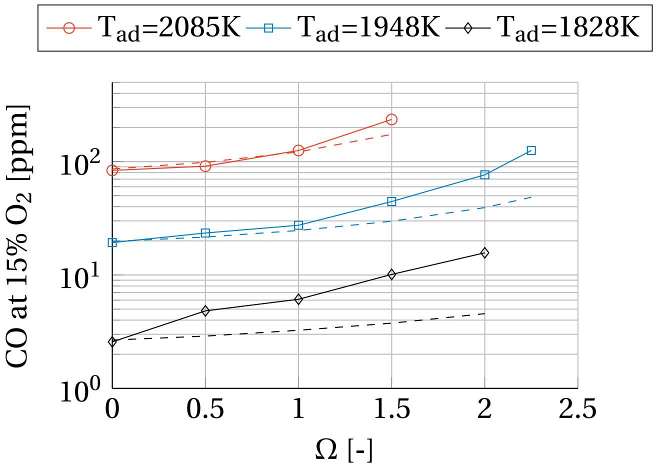

Figure 6.5: Comparison of global CO concentrations from experimental (–) and Cantera (- -) investigations at constant T_{ad}.

the higher equivalence ratio compared to other measurement series, the absolute values of the water mass flow are higher for operation at Φ=0.714. Consequently, the effects of inhomogeneous water distribution are more visible in this measurement series. As the result, the probability of local quenching phenomena grows. This, in turn, slows down the CO burnout at certain locations in the combustor leading to super-equilibrium CO values at the outlet.

As shown above, flame temperature has a significant influence on CO formation. To emphasize the dominating effect of flame temperature on CO formation, Fig. 6.5 shows global CO values at constant T_{ad}. Again, the measured values are compared with calculated equilibrium concentrations at similar operating conditions. Measured CO values increase steadily with rising Ω. At first this increase is slow, however, the gradual increase speeds up at higher water contents. The calculated equilibrium CO concentrations behave similarly, however, depending on the flame temperature, deviations originating from non-equilibrium processes are found in the experiment.

Generally, the rising CO values with increasing Ω are closely related to the mode of operation. As water is added, additional fuel is used to compensate the temperature reduction. This increases the content of C atoms in the reactant mixture and the equilibrium CO value rises. This behavior occurs, although the adiabatic flame temperature is held constant. However, the rise of

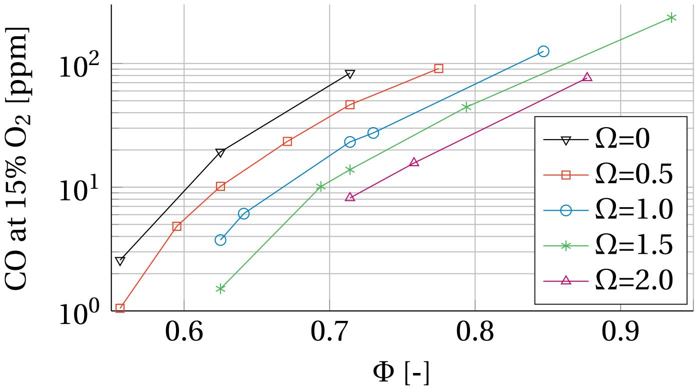

Figure 6.6: Dependency of global CO concentrations on Φ.

the CO equilibrium concentration only partly explains the measured high CO values. While measured and calculated CO concentrations are in good agreement over the complete operating range for T_{ad}=2085 K deviations from the ideal behavior rise with decreasing flame temperatures. For T_{ad}=1948 K and an atomizing air mass flow rate of 3.5 g/s, measured CO concentrations match the equilibrium CO values up to Ω=1. Above this threshold, the contribution of non-equilibrium CO rises until twice the equilibrium CO value is reached at Ω=2.25. A further reduction of the flame temperature leads to lower absolute CO concentrations as well as rising contributions of CO from quenching processes. Due to the lower temperature level in the combustor CO burnout slows down and local quenching is promoted. Consequently, the amount of super-equilibrium CO at the combustor outlet rises. The rising contribution of non-equilibrium CO at increasing water content seems to be related to inhomogeneous water distributions in the combustor (see description in section 6.1.1). Zones of high water content and low temperature form close to the combustor walls, thereby increasing local quenching probability and global CO values.

As seen from Figs. 6.4 and 6.5, the operating conditions of the test rig strongly influence CO formation. One important parameter in this context is the flame temperature in the combustor. However, influences of inhomogeneous water distribution in the test rig also play an important role. Figure 6.6 sums up the results on CO formation in premixed flames with water injection. The dependence of normalized CO concentrations on Φ is shown for different water contents. For dry operation a strong effect of equivalence ratio is found due to increasing flame temperatures. Water addition shifts the curve to higher equivalence ratios, however, the basic shape of the curve remains similar. Although, the contribution of non-equilibrium CO rises with increasing Φ, low CO values can still be achieved at high water contents. This extends the operating range of gas turbines towards higher equivalence ratios. Consequently, with a suitable choice of the operating conditions, water addition in gas turbine combustors is not limited by excessive CO formation.

6.2 Local Species Concentration Measurements

After the analysis of the global pollutant concentrations, pollutant formation is now investigated in more detail. For all experimental investigations in this section the test rig setup with nozzle configuration C1 is used and the atomizing air mass flow rate is set to 3.5 g/s. Local species concentration measurements of CO, O_2 and CO_2 show the influence of water injection on the combustion process on a spatially resolved measurement grid. These local measurements help to identify changes in the reaction distribution as well as alterations in the pollutant formation in wet flames. In the first part, the conversion of fuel to reaction products is investigated. Based on local CO and CO_2 concentration measurements distributions of the reaction progress variable in the combustor are calculated. Subsequently, pollutant formation in the combustor is investigated in more detail. Due to the large influence of water addition on CO formation, this analysis is focused on CO formation in wet flames.

6.2.1 Influence of Water Injection on the Reaction Progress

Figure 6.7 shows distributions of the reaction progress variable in the combustor for different operating conditions. The reaction progress variable is calculated according to Eq.4.5 and can take values between 0 and 1, where 0 denotes the unburned mixture and 1 describes the fully burned mixture. Two series of measurements are shown in the figure. Three field measurements with

(a) $\Phi = 0.625$, $\Omega = 0$, $T_{ad} = 1948$ K

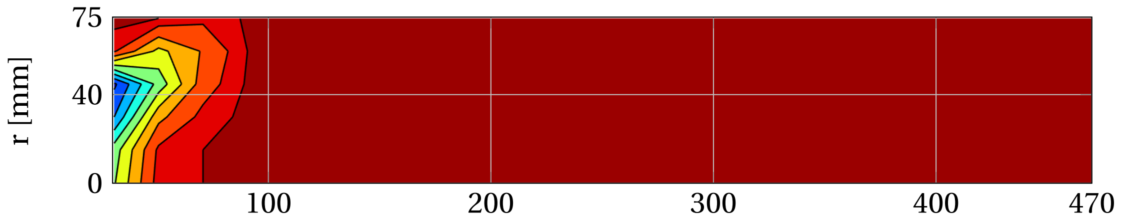

(b) $\Phi = 0.796$, $\Omega = 1.5$, $T_{ad} = 1948$ K

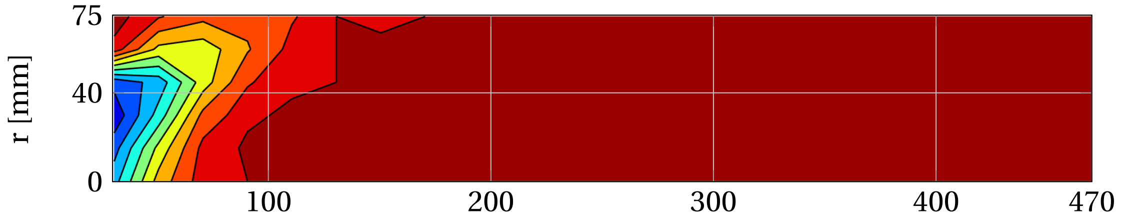

(c) $\Phi = 0.877$, $\Omega = 2.0$, $T_{ad} = 1948$ K

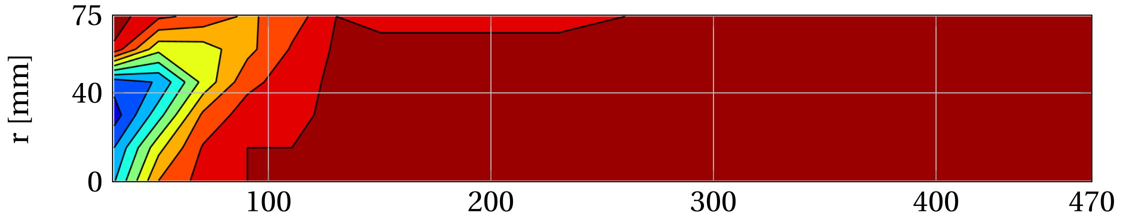

(d) $\Phi = 0.625$, $\Omega = 1.5$, $T_{ad} = 1739$ K

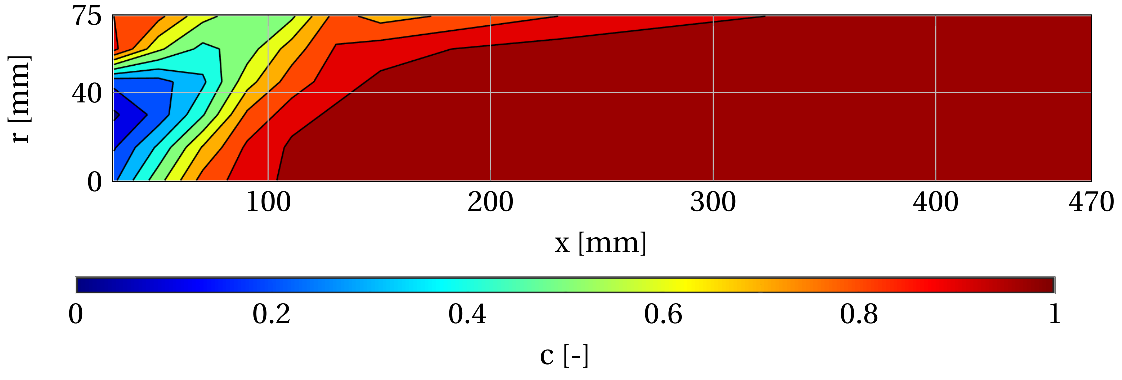

Figure 6.7: Distributions of the reaction progress variable at different operating conditions.

same T_{ad} and different Ω are shown in Figs. 6.7a to 6.7c whereas in Figs. 6.7a and 6.7d two cases with same Φ and different T_{ad} are compared with each other.

For dry operation in Fig. 6.7a, the reaction zone is compact and located close to the inlet of the combustor. The reaction progress quickly changes from 0 to 1 which indicates fast reaction of the fuel. Consequently, the progress variable reaches its maximum value of 1 over the complete combustor cross-section at axial distances higher than 90 mm. However, adding water at constant T_{ad} changes this behavior. With increasing water content, the flame is shifted downstream until a significant amount of unburned fuel air mixture is found at an axial distance of 90 mm. Due to the flow field in the combustor with an inner as well as an outer recirculation zone the downstream shift also moves the flame closer to the combustor walls. Consequently, low values of the reaction progress variable are detected close to the combustor walls at higher Ω values. With increasing amounts of water this effect becomes more evident.

Besides this displacement of the reaction progress the reaction zone extends farther downstream for operating conditions with water injection. While the extension is relatively small in the center of the combustor, significant effects are found in the near-wall regions, especially for reaction progress values between 0.9 and 1. As the result, the zone with c-values below 1 is extended to higher axial distances. While a reaction progress variable of unity is reached at 100 mm for dry operation, the location where $c=1$ is reached over the complete combustor cross section is shifted downstream to 130 mm for $\Omega=1.5$ and 170 mm for $\Omega=2$. Partly, these effects are related to the decreased reactivity of the fuel-air mixture as shown in section 3.2. As the result, the flame speed slows down which influences the length and position of the reaction zone. Additionally, the higher overall mass flow rate at wet conditions increases the flow speed in the combustor and reduces the combustor residence time. Assuming a constant timescale of reaction, the reaction zone extends downstream and shifts to higher axial distances.

When comparing images at constant Φ and decreasing flame temperature in Figs. 6.7a and 6.7d, similar effects occur. A downstream shift as well as a significant extension of the reaction zone are found. Compared to operation at constant T_{ad}, the effect of water injection is stronger. In the center of the combustor the reaction zone reaches down to more than 100 mm while c-values below 1 are found down to 300 mm axial distance in the near-wall regions. As already shown for the OH* chemiluminescence measurements this strong effect of water injection is related to the decreased temperature level in the combustor. As the temperature drop due to water addition is not compensated in this measurement series, the adiabatic flame temperature drops by more than 200 K. This reduces the reactivity of the fuel air mixture and slows down the reaction process. As the result, the reaction zone extends farther downstream. Analogue to operation at constant T_{ad}, a stronger effect of water addition is found at higher radial distances. For both operating conditions this effect is related to the inhomogeneous water distribution in the combustor. As shown before, zones of high water content form close to the combustor walls, thereby reducing the mixture reactivity locally. Consequently, lower values of the reaction progress are found. Additionally, this effect increases due to heat losses to the combustor walls. As the result, the fluid close to the wall cools down and the reactivity drops even further. The combination of the two effects explains the strong effect of water addition on reaction progress in the near-wall zones. Still, Fig. 6.7 shows that the reaction progress variable reaches its maximum value well before the exit of the combustor.

To quantify the effects of water addition on the axial evolution of the reaction progress variable, measured values are averaged over the combustor cross-section. Figure 6.8 shows the area-averaged reaction progress for different operating conditions. The curve for dry operation starts from c=0.5 at an axial distance of 30 mm and rises to c=1 within about 60 mm. At distances of 100 mm and higher, heat release is almost completed. For wet operation and constant T_{ad} similar curves are found. However, as already shown in Fig.6.7, these curves shift downstream by about 20 mm. While similar gradients of wet and dry curves are found for moderate reaction progress values, wet curves show a smaller slope at c>0.95. This indicates a reduction of the averaged heat release at higher c values. The change of Ω from 1.5 to 2 has only minor effect on the area-averaged reaction progress. As already shown in section 5.3, the heat release distribution and consequently the distribution of the reac-

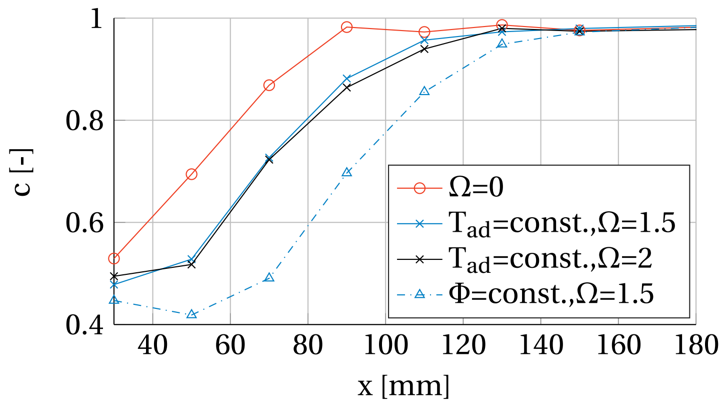

Figure 6.8: Axial distribution of the reaction progress variable averaged over r.

tion progress variable respond to the changed water content with a downstream shift. This gives room for the evaporation of the droplets. However, at higher water contents the displacement of the flame is limited by the combustor walls. Therefore, only minor changes of the flame position as well as the distribution of the reaction progress are found when increasing Ω from 1.5 to 2 . The last curve in Fig. 6.8 shows the reaction progress at constant Φ and decreased flame temperature. This curve shifts downstream by about 40 mm compared to dry operation, which shows the dominating influence of flame temperature on the heat release distribution in the combustor. At first, the reaction progress variable remains constant, before a steep rise up to c=0.95 occurs. Similar to cases at constant T_{ad}, heat release slows down for c>0.95 and the reaction zone extends farther downstream.

6.2.2 Local CO Concentrations

After the characterization of the reaction progress at dry and wet operating conditions, the focus is now on CO formation in the combustor. As shown in section 6.1, CO formation is influenced by equilibrium processes as well as non-equilibrium effects. 2 steps are relevant: CO formation and CO burnout. As the result, CO formation in the combustor is a complex process which can not be analyzed using reaction progress variable distributions. CO is formed during the consumption of the fuel molecules. As the fuel consumption zone in the combustor is small, high concentrations of CO occur. Subsequently CO reacts with oxygen and forms CO_2. This CO burnout reaction reduces the maximum CO values until CO concentration reaches its equilibrium value. However, as the burnout reaction is strongly temperature dependent [79], a reduction of the flame temperature can slow down or even stop CO burnout. The reaction is quenched and chemical equilibrium is not reached, leading to super-equilibrium CO concentrations at the combustor outlet [33]. According to the results presented in section 6.1, different contributions of non-equilibrium CO are detected in global CO concentration measurements. Although quenching phenomena are identified as source of elevated CO concentrations, no detailed information on the quenching processes is given. In order to overcome this shortfall, spatially resolved CO concentration measurements are conducted at dry and wet conditions. In the following, local concentration fields of CO in Figs. 6.9 and 6.10 are analyzed and quenching zones in the combustor are identified. Furthermore, reasons for the occurrence of quenching zones in the combustor are determined.

Figure 6.9 shows local CO concentrations in the combustor for rising water contents and constant T_{ad}. At dry operation (Fig. 6.9a) the CO concentration rises steeply close to the combustor inlet until a maximum value is reached at an axial distance of 50 mm. The burnout reaction quickly reduces the CO concentration and chemical equilibrium is reached. Due to the flow field in the combustor as well as the diabatic combustion chamber, higher temperatures are found in the center of the combustor leading to faster CO burnout. Up to a distance of about 300 mm higher CO values are found close to the wall compared to the center region. Due to heat losses over the combustor walls the temperature of the exhaust gas is lower, thereby slowing down the burnout reaction rate. This results in higher local CO values. However, this situation changes for distances larger than 300 mm. From this point on, lower CO concentrations are measured close to the wall compared to similar axial positions in the center of the combustor. For these axial distances the burnout of CO is completed in the center of the combustor. However, due to lower temperatures at the wall, local CO equilibrium values are smaller there. Consequently, the burnout reaction further reduces CO concentration and lower CO values are measured at the wall.

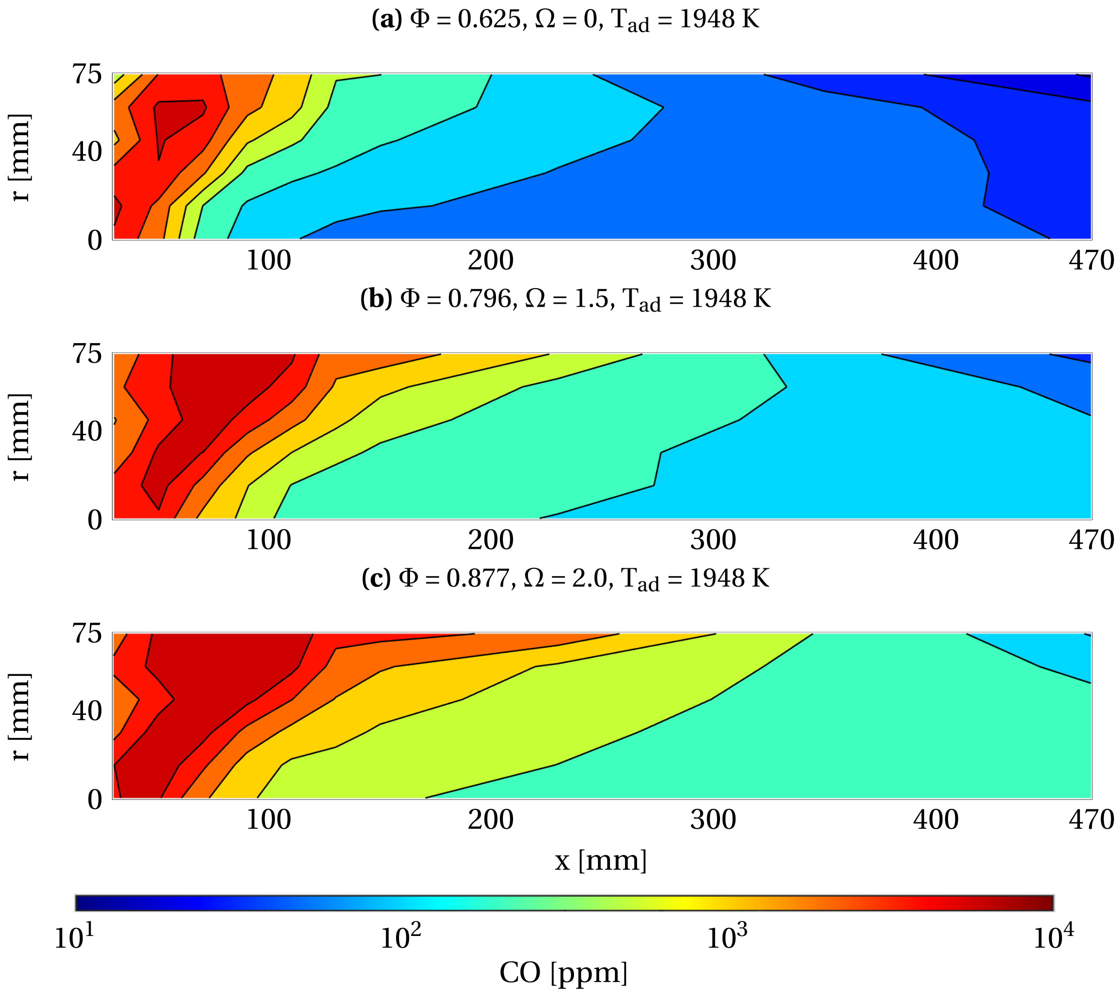

Figure 6.9: Distributions of the CO concentration at constant T_{ad}.

Water injection at constant T_{ad} changes this behavior. Starting with dry operation in Fig. 6.9a, the water content increases to Ω=1.5 in Fig. 6.9b and Ω=2 in Fig. 6.9c. Generally, the typical shape of the CO distribution is preserved. A steep rise of the CO concentration close to the combustor inlet is followed by a rapid reduction of the maximum values. However, the overall CO level is higher for operation with water injection. Due to the decreased reactivity of the reactant mixture, the fuel consumption zone is displaced downstream. This effect influences the CO values: While the influence on CO formation is small, differences in the CO burnout region are detected. Compared to dry operation, the zone of high CO content is larger. Similar to distributions of the reaction progress variable, this zone is extended and shifted downstream.

The extension is found especially in the near-wall regions, leading to high CO values at axial distances larger than 200 mm. As described in section 6.1 this increase is partly related to the increased equivalence ratio at wet operation.

Another factor influencing the CO distribution in the combustor is the reduced residence time at wet conditions. Water injection and the increased equivalence ratio raise the mass flow rate in the combustor. However, as the geometry of the combustion chamber remains constant, the velocity of the gas mixture rises. Assuming similar timescales for the CO burnout at dry and wet conditions, the burnout zone becomes longer at operating conditions with water injection. As already mentioned for dry operation, CO burnout seems to be faster in the center of the combustor. Due to higher temperatures as well as the flow structure in the combustor, CO drops more quickly there. In contrast, a stronger influence of water on CO formation is found close to the wall. Especially the length of the CO burnout zone rises significantly compared to dry operation. Due to the inhomogeneous distribution of the water droplets at higher Ω as well as the effect of heat losses at the wall, the quenching probability at the wall increases which slows down CO burnout. While CO concentrations of 1000 ppm are measured at 100 mm for dry operation this position is close to 220 mm at Ω=1.5 and 300 mm at Ω=2. These local effects also have an influence on global CO concentrations. As seen in Fig. 6.5, higher contributions of non-equilibrium CO are measured for higher Ω values. The combination of increased flow velocities at operating points with water injection as well as quenching phenomena in the near-wall regions lead to higher CO values in the downstream regions of the combustor. Finally, complete burnout of CO can not be achieved anymore and pollutant concentrations at the outlet increase.

To show the effects of reduced flame temperature on CO formation, local CO concentrations are determined at wet conditions and constant Φ. Figure 6.10 compares CO distributions at dry operation and at Ω=1.5. As the level of CO concentrations is lower compared to Fig. 6.9, the scaling of the colorbar is adapted accordingly. The situation at dry operation in Fig. 6.10a is identical to the one shown in Fig. 6.9a. Figure 6.10b presents the CO distribution for wet operation at Φ=0.625 and Ω=1.5. Compared to dry conditions at Φ=0.625

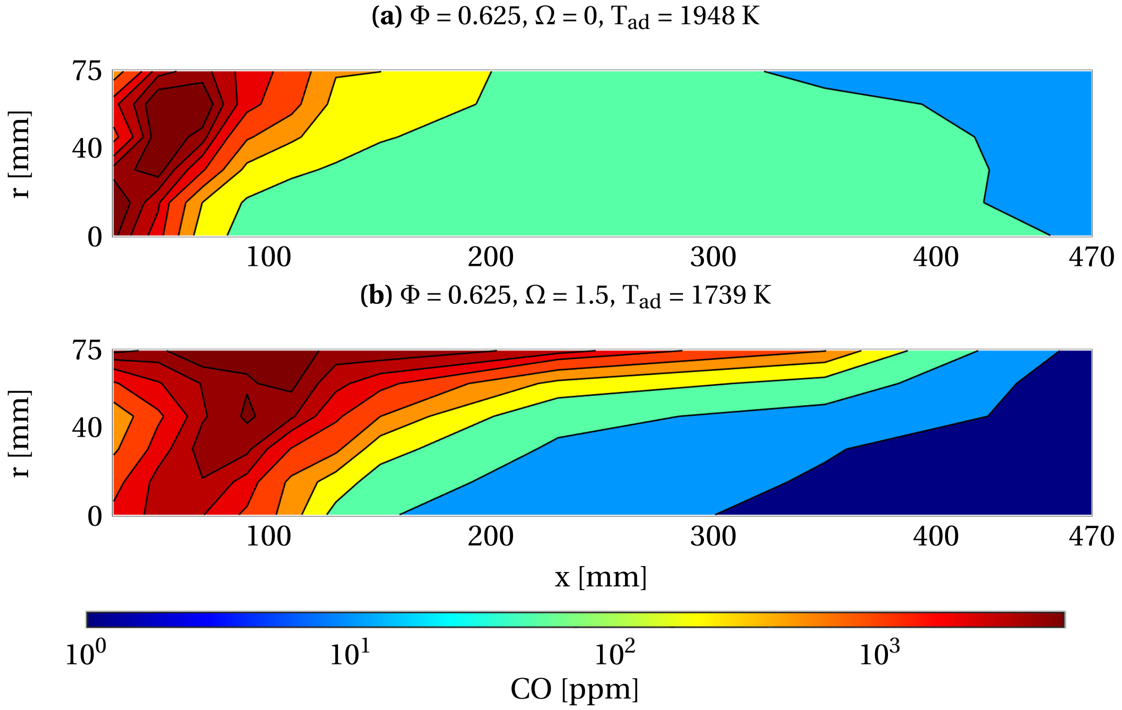

Figure 6.10: Distributions of the CO concentration variable at constant Φ.

the flame temperature drops by more than 200 K which influences the CO distribution considerably. Similar to wet operation at constant T_{ad}, the zone of high CO content is shifted downstream and closer to the wall. As already seen for distributions of the reaction progress variable, effects of water injection are stronger for operation at decreased temperature compared to operation at constant T_{ad}. Due to the lower temperature with water addition as well as due to the shorter combustor residence times, the zone of high CO content extends farther downstream. As shown for constant T_{ad}, CO concentrations decrease quickly in longitudinal direction in the center of the combustor. As the equilibrium CO value is lower for operation with water injection, lower global CO concentrations are measured. Close to the wall, high CO values are found from 30 mm up to 350 mm. The extension of the zone of high CO content is mainly influenced by increased water contents as well as by heat loss in the near-wall regions. Similar to the influences on the reaction progress variable, both effects decrease local flame temperatures and raise the quenching probability, slowing down CO burnout. However, due to very low CO values in the center of the combustor, radial mixing reduces these high local CO contents.

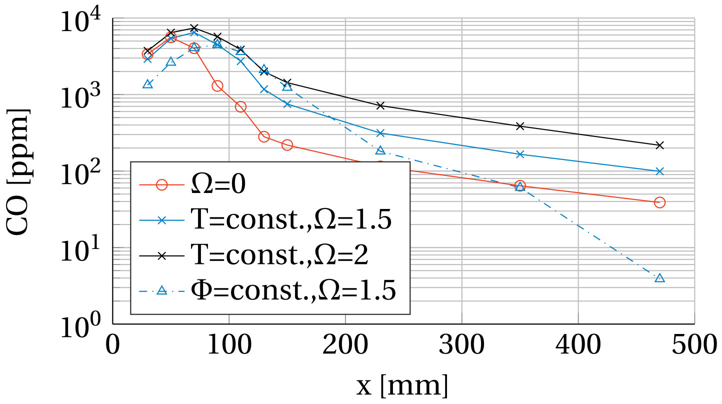

Figure 6.11: Axial distribution of the area averaged CO concentration.

Consequently, CO burns out completely and low concentrations are found at the combustor outlet.

Figure 6.11 shows a quantitative comparison of area-averaged concentrations at different axial locations. The curve for dry operation rises quickly up to axial distances of 50 mm where a maximum CO value of 5500 ppm is measured. Within a distance of 80 mm the concentration drops to 280 ppm until CO values are decreasing with a constant slope. Finally, an equilibrium CO value of 40 ppm is found at the outlet. Water addition at constant T_{ad} alters this curve. The position of the maximum CO values is shifted downstream to an axial distance of 70 mm while the maximum concentrations change to 6400 ppm at Ω=1.5 and 7200 ppm at Ω=2. Similar to dry operation, maximum CO values drop quickly and finally a constant slope of the CO curves is observed. This reduction of the area-averaged CO values for higher axial distances is related to heat losses in the exhaust gas due to the diabatic combustion chamber. Since adiabatic flame temperatures at dry and wet operation are similar, similar heat losses can be assumed. Consequently, identical slopes for dry and wet operation at constant T_{ad} are found.

For water injection at Φ=1.5, similar effects are found. The position of maximum CO concentration shifts downstream to an axial distance of 90 mm. Compared to curves at constant T_{ad}, a larger shift is observed. A similar effect has already been found in OH* chemiluminescence images as well as for the reaction progress variable in the combustor. Furthermore, the maximum CO

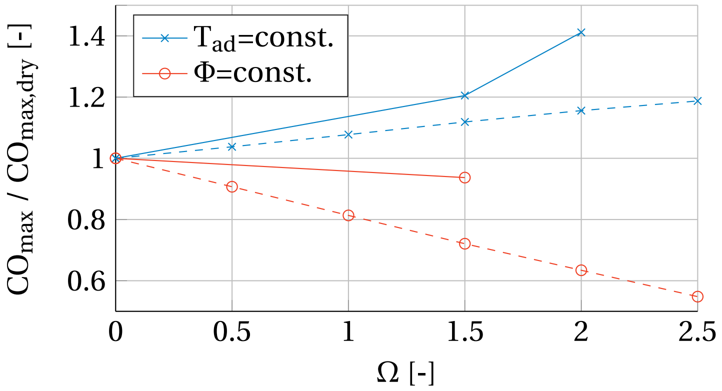

Figure 6.12: Maximum CO values at different operating conditions. Comparison of experimental (–) and Cantera (- -) investigations.

value drops by about 20% to 4400 ppm. Although the reduction of CO is slower than for dry operation, after 150 mm the curve assumes a constant slope. As the flame temperature is lower, heat losses in the combustor decrease and a steeper slope of the curve establishes.

To conclude the analysis of CO formation, the maximum CO values are examined more closely in Fig. 6.12. This figure compares the maximum CO values of the experimentally determined CO fields with numerical values from Cantera free flame simulations[2]. As shown for the Cantera equilibrium calculations, liquid water is implemented as steam. Furthermore, the inlet temperature of the simulation is decreased according to the water content in order to consider the heat of vaporization of the water. As measured CO values are determined in the dry exhaust gas, CO values from the simulation are normalized to dry conditions. Higher absolute values of CO are found in the numerical simulation as Cantera simulations are implemented for adiabatic operating conditions. In order to compare numerical results to CO values from experimental measurements, both, experimental an numerical values, are normalized with the corresponding dry CO value.

For operation at constant T_{ad} and Ω=2.5, the maximum CO value in the simulation increases by about 20 % compared to dry operation. This effect mainly originates from the higher equivalence ratio at wet operating conditions as

---

[2] The setup of the Cantera simulations is described in section 4.3.

well as from the higher water content in the exhaust gas. As experimentally determined values are measured in the dry exhaust gas, the increased water content influences the normalization of the CO. Consequently, higher CO values are found for higher Ω. However, a look at the experimentally determined values reveals an even bigger rise of the CO concentration. While the deviation is relatively small for Ω=1.5, a stronger rise of the maximum CO value appears for Ω=2. As the influence of rising Φ is already captured by the results of the simulations, the additional rise can only be related to non-ideal behavior of the combustion test rig. As shown before for global NO_x concentrations, the inhomogeneity of the water distribution rises with increasing Ω. Local hotspots form and the maximum CO values in the flame increase. Due to the rising inhomogeneity of the water distribution, the effect of the local hotspots increases progressively with Ω (see Fig. 6.12).

For operation at constant Φ and rising Ω, maximum CO values fall in the experimental and the numerical measurements. In the Cantera simulations, maximum concentrations drop by 40 % compared to dry operation for Ω=2.0. However, experimental values for constant Φ decrease slower than the numerical prediction. This means, that higher maximum CO values are detected in the experimental results compared to the numerical simulations. In the author’s opinion this effect is again related to the influence of local hotspots in the flame.

6.3 Influence of Droplet Size on Pollutant Formation

As shown above, the evaporation of the droplets strongly influences pollutant formation in flames with water injection. If droplets are evaporating fast, the influence of water injection on pollutant formation is low. However, if the evaporation of the droplets is too slow, NO_x and CO concentrations at the outlet rise. Consequently, an improvement of droplet evaporation should enhance the combustor performance in terms of pollutant formation. However, as a direct measurement of the evaporated mass flow rate was not possible in

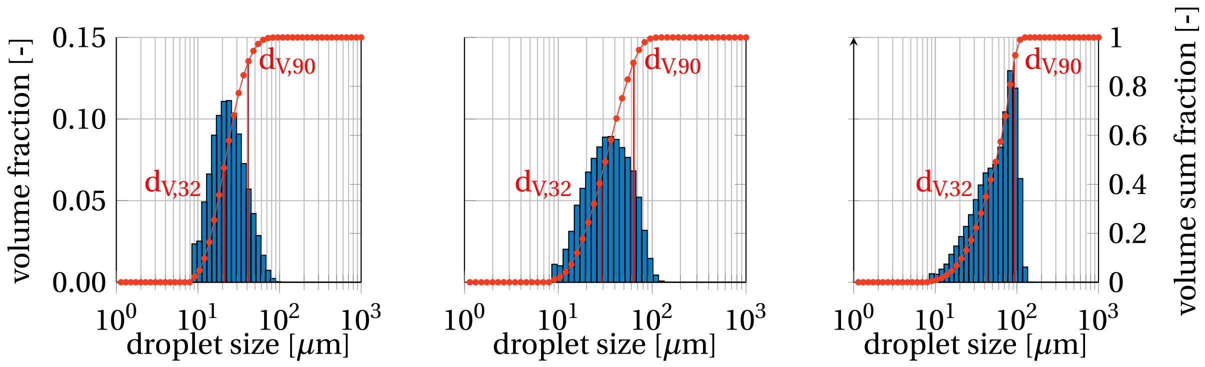

(a) $\dot{m}_{a,at} = 4.0$ g/s, $\Omega = 0.5$ **(b)** $\dot{m}_{a,at} = 4.0$ g/s, $\Omega = 1.5$ **(c)** $\dot{m}_{a,at} = 2.0$ g/s, $\Omega = 1.5$

Figure 6.13: Droplet size distributions for nozzle configuration C1 and different operating conditions.

the experimental setup, the evaporation behavior of the droplets is analyzed indirectly using droplet size measurements. As the evaporation behavior of droplets is closely coupled to the droplet size (see section 2.1.2), the next section is going to investigate the influence of water droplet size on NO_x and CO formation.

6.3.1 Droplet Size Distributions

In order to characterize the water injection system, droplet size measurements have been conducted in an external spray test rig using a Malvern Particle Sizer. Variations in the water mass flow rate as well as the atomizing air mass flow rate are analyzed in the following. Figure 6.13 shows the particle size distributions for 3 different operating conditions. The comparison of these size distributions shows the influences of changes in water or atomizing air mass flow rate on the particle size distributions. Figure 6.13a and 6.13b show the effect of a variation of Ω, whereas the distributions 6.13b and 6.13c reveal the influence of the atomizing air mass flow rate on droplet size distributions. Although the effects are shown only for one specific set of parameters, conclusions can be drawn independently of the exact mass flow rates.

Figure 6.13a shows a typical particle size distribution for nozzle configuration

C1[3] at high atomizing air mass flow rates and low water mass flow rates. At an atomizing air mass flow rate of 4 g/s and Ω=0.5 the used nozzle configuration shows a well atomized spray with a $d_{V,32}$ of 21 μm and a $d_{V,90}$ of 41 μm. Due to the high atomizing air mass flow rate as well as the low water mass flow rate, a high relative velocity between the two phases is achieved. Consequently, good atomization occurs. With increasing Ω, the atomization quality of the nozzle deteriorates. Figure 6.13b shows the histogram for a water to fuel ratio of Ω=1.5. While the variance of the distribution is small for the low water mass flow rate a broader distribution is found for Ω=1.5. Furthermore, the number of larger droplet sizes increases and the maximum of the histogram is shifted to higher diameter values. Generally, higher water mass flow rates raise the velocity of the water flow in the nozzle. Given a constant atomizing air mass flow rate, the relative velocity between water and air decreases, thereby deteriorating the atomization quality (see explanation in section 2.1.2). While the $d_{V,32}$ increases marginally from 21 μm to 23 μm, the $d_{V,90}$ rises from 41 μm to 68 μm compared to operation at Ω=0.5. Following the d^2 law it can be concluded that evaporation of this spray is slower compared to operation at lower water mass flow rates. However, as the volume fraction of very large droplets is relatively low, the effect remains moderate.

In order to investigate the influence of droplet size on pollutant formation, combustion experiments with different atomization qualities are required. Reducing the atomizing air mass flow deteriorates the atomization performance of the nozzle and shifts the histogram to higher droplet sizes. As shown in Fig. 6.13c, the share of droplets larger than 80 μm rises considerably which slows down the evaporation of the water in the combustor. The Sauter mean diameter $d_{V,32}$ rises to 44 μm and a $d_{V,90}$ of 93 μm is found. The reduction of the atomization quality in the spray is again related to the lower relative velocity between water and air flow. As shown in section 2.1.3, this decrease reduces the Reynolds number as well as the Weber number. Consequently, the atomization quality declines since bigger droplets form.

Figure 6.14 shows the spray quality of nozzle configurations C1 and C2 for a wide range of operating conditions. In order to assess the spray quality quickly,

---

[3] For detailed explanations on the different nozzle configurations see section 4.1.2.

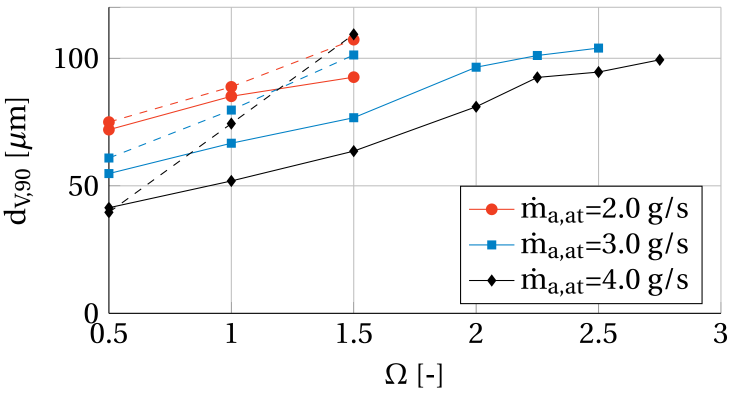

Figure 6.14: $d_{V,90}$ for different operating conditions. Comparison of nozzle configuration C1 (–) and C2 (- -).

one representative diameter is chosen for each droplet size distribution. As shown in Fig. 6.13 changes of the Sauter mean diameter are small, although the atomization quality is changing significantly. For this reason, the $d_{V,90}$ is taken as the measure for atomization quality.

Figure 6.14 shows the development of the $d_{V,90}$ for different Ω as well as different atomizing air mass flow rates. Furthermore, curves for a second nozzle configuration (C2) are included. The two nozzle configurations differ only in the outlet diameter of the water nozzle (see section 4.1.2). While the outlet diameter is 1.8 mm for configuration C1, this diameter is 0.8 mm for configuration C2. Due to the lower outlet area of the second water nozzle, the flow speed of the water rises at similar mass flow rates. Consequently, the differential velocity between water and atomizing air and the atomization quality drop. For the investigated nozzle configurations C1 and C2 it is observed that the spray quality deteriorates with rising Ω and decreasing atomizing air mass flow rates. While $d_{V,90}$ rises gradually with increasing Ω, a variation of $\dot{m}_{a,at}$ shifts the curves towards higher or lower representative diameters. These trends are found for both nozzle configurations. However, the $d_{V,90}$ for nozzle C2 shows a stronger dependency on Ω. Consequently, the slopes of the curves for C2 are steeper compared to configuration C1. For Ω=1.5 a wide range of droplet sizes between 65 μm and 110 μm is found depending on atomizing air mass flow rate as well as nozzle configuration. Smallest droplet diameters are found for configuration C1 and an atomizing air mass flow rate of 4 g/s.

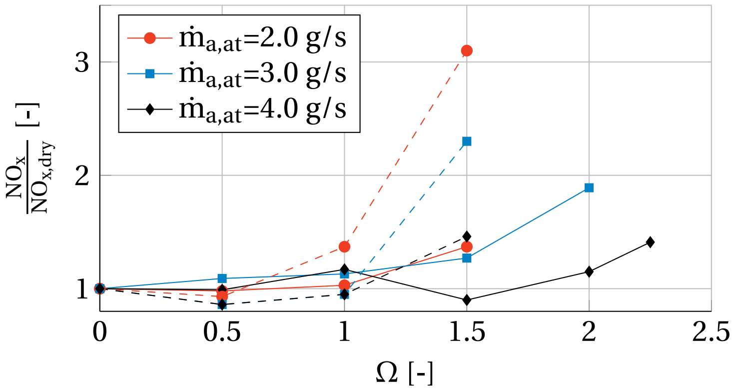

Figure 6.15: NO_x concentrations for nozzle configuration C1 (–) and C2 (- -) at constant T_{ad} and different atomizing air mass flow rates.

6.3.2 Influence of Atomization Quality on Global NO_x Concentrations

The influence of water droplet size on NO_x formation in the combustor is shown in this section. In order to analyze pollutant formation, NO_x concentrations at constant T_{ad} are determined for different water to fuel ratios and different water droplet size distributions. The measurements are conducted downstream of the combustor outlet with the global emission measurement probe introduced in section 4.1.1. As usual, all measured values are normalized to 15% O_2 in the exhaust gas. In order to compare the different NO_x curves qualitatively, values at wet operating conditions are divided by the respective concentration at dry operation.

Figure 6.15 shows NO_x curves at constant T_{ad} for identical operating points and different atomizing air mass flow rates. Measurement values for nozzle configurations C1 and C2 are included in the graph. As shown in section 6.3.1, the variation of these parameters strongly influences the droplet size distributions in the water spray. Generally, all curves share a common characteristic shape with a constant part at the beginning and a rise at higher water contents. For water contents below Ω=1, the NO_x ratio remains constant, independent of the droplet size distribution in the water spray. However, for Ω values above unity, significant deviations are found. While values for operation with nozzle configuration C2 rise steeply, NO_x concentrations for nozzle configuration C1 remain constant up to higher values of Ω. Similarly, NO_x values at lower atomizing air mass flow rates rise considerably faster compared to operating points with higher atomizing air mass flow rates. As mentioned above, these differences between the NO_x curves are directly related to the evaporation behavior of the water droplets. For an atomizing air mass flow rate of 2 g/s Fig. 6.14 shows high values of $d_{V,90}$. For Ω>1 the representative droplet size rises to 90 μm and higher. Due to the large droplet size, evaporation of the water phase is slowed down and higher local temperatures in the combustor occur. Consequently, Fig. 6.15 shows a steep increase of the NO_x curve for Ω values higher than unity. With increasing atomizing air mass flow rate droplet size decreases and evaporation of the water phase becomes faster. As the result, lower NO_x values are measured at the combustor outlet. For an atomizing air mass flow rate of 4 g/s the lowest NO_x increase is found for configuration C2. This effect originates from the high atomization quality at high air mass flow rates and the faster evaporation. It can be concluded that a further improvement of the NO_x emissions at high water contents would be possible after a further improvement of the nozzle geometry beyond the configuration C2.

As shown in Fig. 6.14 nozzle configuration C1 produces finer droplets compared to configuration C2. Consequently, the surface to volume ratio of the water phase rises and evaporation of the droplets is accelerated. The effect of increased evaporation is shown in Fig. 6.15. Curves for nozzle configuration C1 show lower values for the NO_x ratio independent of Ω. Again, lowest NO_x values are measured for the highest atomizing air mass flow rates. For an atomizing air mass flow rate of 2 g/s the curve remains constant up to Ω=1.25 and with an increase of the atomizing air mass flow rate constant NO_x values are obtained up to Ω=2.

Figure 6.16 relates normalized NO_x values to droplet diameters ($d_{V,90}$) of the injected water sprays. One series of measurements is shown for each nozzle configuration at constant T_{ad}, variable Ω as well as variable atomizing air mass flow rate. Independent of the nozzle configuration, a characteristic curve of the NO_x ratio is found. As long as the atomization of the water is good enough, droplets evaporate quickly and the local flame temperature is held

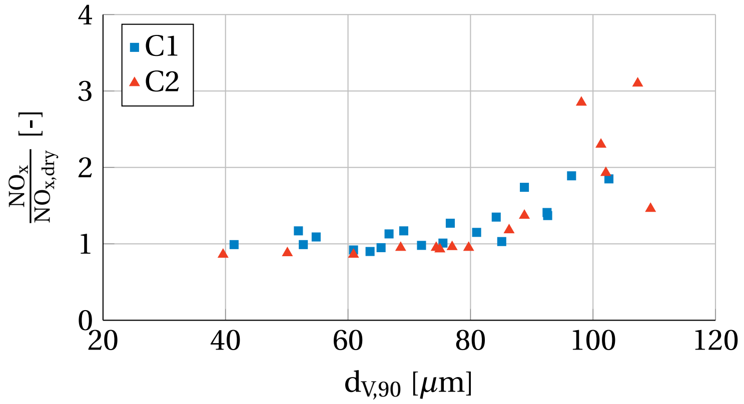

Figure 6.16: Characteristic droplet diameter of the NO_x increase for measurements at constant T_{ad}.

constant. Consequently, the NO_x ratio remains constant for $d_{V,90}$ values lower than 80 μm. However, if the characteristic droplet size rises above a critical diameter of 80 μm the NO_x ratio starts to rise. A rise of $d_{V,90}$ from 80 μm to 100 μm leads to a NO_x increase of 100%. While droplets smaller than the critical diameter evaporate quickly, droplets above this size are too big to evaporate completely before entering the flame zone. As shown in the macroscopic analysis in section 5.3, these droplets advance to higher axial distances in the combustion chamber and lead to higher local flame temperatures as well as higher NO_x values in the combustor. For $d_{V,90}$ values above 100 μm this development intensifies and an even steeper increase of the NO_x ratio is found.

The close dependency of the NO_x values on the water droplet diameter confirms the dominant influence of droplet evaporation on combustion. Furthermore, this fact allows to use NO_x concentration measurements to assess the performance of water injection systems. Due to the high sensitivity of NO formation to changes in the flame temperature, evaporation of droplets in the combustor can be analyzed indirectly. For droplet sizes smaller than the critical droplet diameter, premixed combustion with water injection is highly similar to premixed combustion with steam injection. However, for droplet sizes above this critical diameter the evaporation behavior of the water phase changes and influences heat release as well as pollutant formation in the combustor. From a technical point of view, this behavior at higher droplet sizes

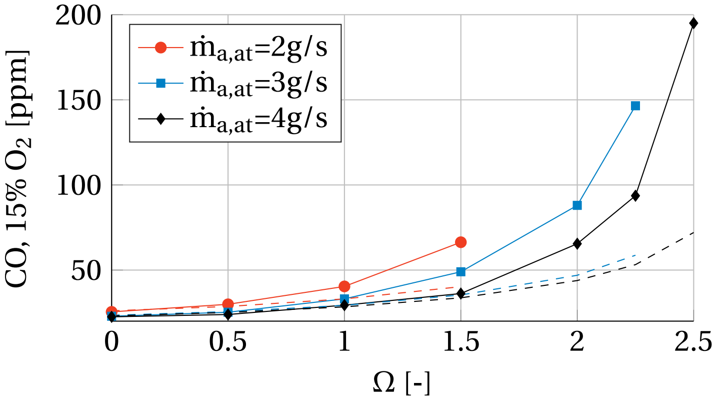

Figure 6.17: Global CO concentrations at constant T_{ad} and different atomizing air mass flow rates. Comparison of experimental (–) and Cantera (- -) results.

limits the operating range of the combustor due to increasing NO_x values. However, given the analysis in Fig. 6.15, the operating range of the combustor can easily be increased if the water droplet size is decreased to values below the critical droplet size.

6.3.3 Influence of Atomization Quality on Global CO Concentrations

To complete the analysis of pollutant formation in wet premixed flames, the influence of droplet size on CO values is investigated in this section. Similar to the investigations for global NO_x concentrations, global CO measurements are conducted for nozzle configuration C1 at constant T_{ad} and variable water droplet sizes. All values are normalized to 15% O_2 in the dry exhaust gas. Figure 6.17 gives an overview of global CO values at different atomizing air mass flow rates and variable Ω. Analogue to investigations in section 6.1, experimentally determined CO values are compared to CO equilibrium values from Cantera calculations. In the experiments, the operating range is limited due to droplets impinging at the combustor wall. As seen in the global analysis, experimentally determined CO values show a strong dependency on Ω. Independently of the atomizing air mass flow rate, CO values rise with increasing water content. As the equivalence ratio increases with Ω the rise of the CO concentration is related to the rising fuel concentration in the reactant mixture. However, the data show a deviation of measured values from CO equilibrium values. Changes of the CO concentration with rising Ω are therefore not completely related to the changing CO equilibrium. In fact, the contribution of CO from non-equilibrium processes is rising with increasing water contents thereby influencing measured global values.

While the equilibrium curves are relatively similar for different atomizing air mass flow rates, higher deviations are found for experimentally determined values. For Ω=1.5, global CO values vary between 66 ppm at an atomizing air mass flow rate of 2 g/s and 36 ppm at 4 g/s. As the overall operating conditions in the test rig are almost identical, this difference of the CO concentrations is directly related to the atomization quality of the water spray. At higher atomizing air mass flow rates, smaller droplets form and evaporation of the water is accelerated. Consequently, the water distribution in the combustor is more homogeneous compared to poorly atomized sprays and the probability of local quenching is lower. As the result, measured CO values reach equilibrium concentrations and the contribution of non-equilibrium CO is low. For lower atomizing air mass flow rates, bigger water droplets form. Evaporation slows down, the quenching probability in the near-wall regions increases and the contribution of non-equilibrium CO rises. As the inhomogeneity of the water distribution rises at bigger droplet sizes, a further increase of the measured CO values is found for decreasing atomizing air mass flow rates. For an atomizing air mass flow rate of 4 g/s, measured CO values reach the equilibrium value up to a water content of Ω=1.5. However, due to the worse atomization quality, this limit drops to Ω=1 at 3 g/s and Ω=0.5 at 2 g/s.

After the qualitative analysis, the dependency of CO on droplet size is investigated for nozzle configuration C1. Figure 6.18 shows the dependency of CO at constant T_{ad} on the water droplet size. Due to the higher equivalence ratio required for keeping T_{ad} constant, larger absolute values are measured at higher water contents. For low Ω values, the global CO concentrations are constant, independent of the water droplet size. At these operating conditions, the water mass flow rate is relatively low compared to the overall reactant mass flow and droplet sizes are small. Water evaporates quickly and the influence of water on

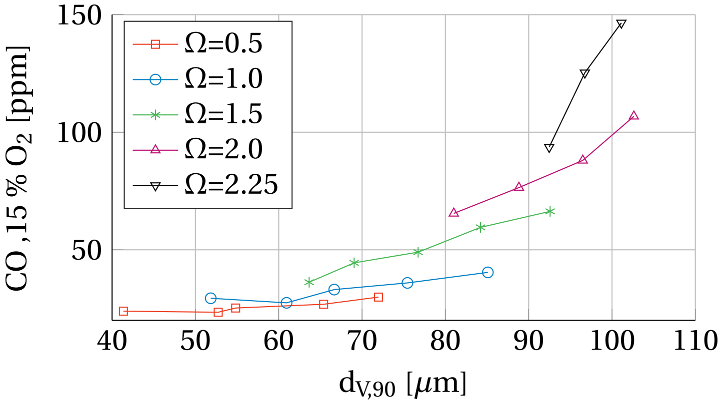

Figure 6.18: Global CO concentrations for nozzle configuration C1 and constant T_{ad} at different Ω values.

the combustion reaction is small. As a result, no local quenching phenomena occur and CO burns out independently of the atomizing air mass flow rate. At higher Ω values, a dependency of the CO concentrations on the water droplet size is found. At constant Ω, higher CO values are measured for higher water droplet sizes. Figure 6.18 shows that this effect becomes stronger for higher water contents. As mentioned above, these effects are related to the increased probability of local quenching. Due to these negative effects of droplets with high $d_{V,90}$, a small droplet size is of high importance in technical combustion systems. Given a sufficient atomization quality non-equilibrium CO can be avoided and complete CO burn out is achieved.

7 Conclusions

In this study, experimental and numerical methods are employed to clarify the influence of water injection on premixed natural gas flames. Optical investigations at an atmospheric combustor test rig focus on the determination of OH* chemiluminescence as well as Mie scattering of the liquid water droplets in the combustor. Besides the optical investigations, a detailed study on the influence of water addition on pollutant formation is conducted, focusing on carbon monoxide as well as on nitrogen oxide emissions. In order to understand the phenomena occurring during premixed combustion with water injection, the experimental data is accompanied by reaction kinetic simulations. The following key findings are obtained:

OH* chemiluminescence measurements show that water injection shifts the flame downstream and extends the heat release zone to higher axial distances. This behavior is strongly dependent on adiabatic flame temperature. At temperatures above 1900 K the influence of water injection on the flame shape and position is small, however, at lower adiabatic flame temperatures water injection alters the heat release distribution in the combustor significantly. A correlation of the flame position with the turbulent flame speed of the fuel-air-water mixture reveals a strong dependency of the heat release distribution on mixture reactivity. Independent of the water to fuel ratio, mixture reactivity governs the heat release distribution over a wide range of operating conditions.

Simultaneous measurements of OH* chemiluminescence and droplet Mie scattering allow to assess the interaction of water phase and flame. With rising water content interaction between droplets and the flame increases. At high water contents evaporation slows down and droplets advance farther into the combustion chamber to regions with high heat release. Consequently, the influence of water injection on the flame rises which also affects pollutant formation in the combustor.

Global NO_x concentrations show a strong dependency on flame temperature and water droplet size. At constant flame temperatures and rising water contents, NO_x values remain stable up to near stoichiometric operation and water to fuel ratios of 2. Above this limit values increase strongly due to local hotspots in the combustor. For well-atomized sprays a correlation with calculated adiabatic flame temperatures reveals that water acts as inert diluent over a wide range of operating conditions. In contrast, poor atomization of the liquid phase leads to local hotspots in the flame and higher global NO_x values.

At constant adiabatic flame temperatures global CO values rise with increasing water to fuel ratios. This increase is partly related to higher equivalence ratios at wet operating conditions. However, the combination of experimental results with reaction kinetic simulations shows increasing contributions of CO from non-equilibrium processes for low flame temperatures and high water to fuel ratios. Local measurements in the combustor show that the increased CO values originate from quenching zones close to the combustor walls. These quenching zones develop due to high local water concentrations as well as heat losses at the combustor walls. Similar to the results for global NO_x values, atomization of the water strongly influences the CO level in the combustor. For well-atomized sprays, global CO values reach chemical equilibrium while poor atomization leads to local quenching as well as elevated CO concentrations at the combustor outlet. Given a well-atomized spray as well as a suitable choice of operating conditions, water injection in the test rig is not limited by excessive CO formation.

Experimental and numerical investigations show that water injection in premixed gas turbine combustors is applicable for a wide range of operating conditions. Near-stoichiometric operation of the test rig at low NO_x and low CO values was demonstrated for different flame temperatures. Under the given operating conditions of the test rig a gas turbine performance simulation suggests a potential power increase of up to 30% compared to dry operation due to water injection. In order to achieve stable operation at wet operating conditions and low pollutant emissions the flame temperature in the combustor shall be above 1900 K. This results in a compact flame shape as well as complete CO burnout. Furthermore, water shall be well-atomized and distributed evenly over the combustor inlet cross-section. The small droplets foster fast evaporation of the water and prevent local hotspots as well as local quenching in the combustor which allows operation at low pollutant emissions.

Bibliography

[1] D. Ahrens. *NO_x-Formation in Reacting Premixed Jets in Hot Cross Flow.* PhD Thesis, Technische Universität München, 2015.

[2] E. Albin, H. Nawroth, S. Göke, Y. D'Angelo, and C. Paschereit. Experimental Investigation of Burning Velocities of Ultra-Wet Methane-Air-Steam Mixtures. *Fuel Processing Technology*, 107:27–35, Mar 2013.

[3] N. Ashgriz, editor. *Handbook of Atomization and Sprays: Theory and Applications.* Springer US, 2011.

[4] V.S. Babkin and A.V. V'yun. Effect of Water Vapor on the Normal Burning Velocity of a Methane-Air Mixture at High Pressures. *Combustion, Explosion, and Shock Waves*, 7(3):339–341, 1971.

[5] G.H. Badeer. GE Aeroderivative Gas Turbines - Design and Operating Features. Technical Report GER-3695E, GE Power Systems, 2000. GER-3695E.

[6] A. Bhargava, M.B. Colket, W.A. Sowa, K.H. Casleton, and D.J. Maloney. An Experimental and Modeling Study of Humid Air Premixed Flames. *Journal of Engineering for Gas Turbines and Power*, 122(3):405, 2000.

[7] A. Bhargava, D.W. Kendrick, M.B. Colket, W.A. Sowa, K.H. Casleton, and D.J. Maloney. Pressure Effect on NO_x and CO Emissions in Industrial Gas Turbines. In *Volume 2: Coal, Biomass and Alternative Fuels: Combustion and Fuels: Oil and Gas Applications: Cycle Innovations.* ASME International, May 2000.

[8] R. Borghi. On the structure and morphology of turbulent premixed flames. In *Recent Advances in the Aerospace Sciences*, pages 117–138. Springer Nature, 1985.

[9] C. Brennen. *Fundamentals of Multiphase Flow.* Cambridge University Press, 2005.

[10] K. Brun, R. Kurz, and H.R. Simmons. Aerodynamic Instability and Life-Limiting Effects of Inlet and Interstage Water Injection Into Gas Turbines. *Journal of Engineering for Gas Turbines and Power*, 128(3):617, 2006.

[11] Bundesministerium für Wirtschaft und Technologie (BMWi). *Energie der Zukunft - Erster Monitoring Bericht.* Bundesministerium für Wirtschaft und Technologie (BMWi), 2012.

[12] J.B. Burnham, M.H. Giuliani, and D.J. Moeller. Development, Installation, and Operating Results of a Steam Injection System (STIG™) in a General Electric LM5000 Gas Generator. *Journal of Engineering for Gas Turbines and Power*, 109(3):257, 1987.

[13] A.G. Chen, D.J. Maloney, and W.H. Day. Humid Air NO_x Reduction Effect on Liquid Fuel Combustion. *Journal of Engineering for Gas Turbines and Power*, 126(1):69, 2004.

[14] D.Y. Cheng and A.L.C. Nelson. The Chronological Development of the Cheng Cycle Steam Injected Gas Turbine During the Past 25 Years. In *Volume 2: Turbo Expo 2002, Parts A and B.* ASME International, 2002.

[15] N. Chigier, editor. *Combustion Measurements.* CRC Press, 1991.

[16] C.T. Crowe, J.D. Schwarzkopf, M. Sommerfeld, and Y. Tsuji. *Multiphase Flows with Droplets and Particles.* Taylor & Francis Inc, 2011.

[17] D.L. Dagget. Water Misting and Injection of Commercial Aircraft Engines to Reduce Airport NO_x, 2004. NASA/CR-2004-212957.

[18] G. Damköhler. Der Einfluss der Turbulenz auf die Flammengeschwindigkeit in Gasgemischen. *Zeitschrift für Elektrochemie und Angewandte Physikalische Chemie*, 1940.

[19] W. H. Day. Humid Air Turbine Cycle Technology - Technical Progress Report - Final Report. Technical Report TW-0077, U.S. Department of Energy and Pratt & Whitney, 2002.

[20] B.Z. Dlugogorski, R.K. Hichens, E.M. Kennedy, and J.W. Bozzelli. Propagation of Laminar Flames in Wet Premixed Natural Gas-Air Mixtures. *Process Safety and Environmental Protection*, 76(2):81–89, May 1998.

[21] F.L. Dryer. Water Addition to Practical Combustion Systems—Concepts and Applications. *Symposium (International) on Combustion*, 16(1):279–295, Jan 1977.

[22] M. Elkotb, M. Mahdy, and M.E. Montaser. Investigation of External-Mixing Air-Blast Atomizers. In *Proceedings of the Second International Conference on Liquid Atomization and Spray Systems*, 1982.

[23] Federal Ministry of Economics and Technology (BMWi). *Research for an Environmentally Sound, Reliable and Affordable Energy Supply - 6th Energy Research Programme of the Federal Government.* Federal Ministry of Economics and Technology (BMWi), 2011.

[24] B. Galmiche, F. Halter, F. Foucher, and P. Dagaut. Effects of Dilution on Laminar Burning Velocity of Premixed Methane/Air Flames. *Energy & Fuels*, 25(3):948–954, Mar 2011.

[25] K. Göckeler. *Influence of Steam Dilution and Hydrogen Enrichment on Laminar Premixed Methane Flames.* PhD Thesis, Technische Universität Berlin, 2015.

[26] K. Göckeler, O. Krüger, and C. Paschereit. Laminar Burning Velocities and Emissions of Hydrogen-Methane-Air-Steam Mixtures. *Journal of Engineering for Gas Turbines and Power*, 137(3):031503, Oct 2014.

[27] S. Göke. *Ultra Wet Combustion: An Experimental and Numerical Study.* PhD Thesis, Technische Universität Berlin, 2012.

[28] S. Göke and C. Paschereit. Influence of Steam Dilution on NO_x Formation in Premixed Natural Gas and Hydrogen Flames. In *50th AIAA Aerospace Sciences Meeting including the New Horizons Forum and Aerospace Exposition.* American Institute of Aeronautics and Astronautics (AIAA), Jan 2012.

[29] D.G. Goodwin, H.K. Moffat, and R.L. Speth. Cantera: An Object-oriented Software Toolkit for Chemical Kinetics, Thermodynamics, and Transport Processes. http://www.cantera.org, 2017. Version 2.3.0.

[30] H. Guo, W.S. Neill, and G.J. Smallwood. A Numerical Study on the Effect of Water Addition on NO Formation in Counterflow CH_4/Air Premixed Flames. *Journal of Engineering for Gas Turbines and Power*, 130(5):054502, 2008.

[31] International Organization for Standardization. ISO 2314: Gas turbines - acceptance tests. ISO Standard, 1999.

[32] M. Jonsson and J. Yan. Humidified Gas Turbines—A Review of Proposed and Implemented Cycles. *Energy*, 30(7):1013–1078, Jun 2005.

[33] F. Joos. *Technische Verbrennung*. Springer Berlin Heidelberg, 2006.

[34] C. Kail and B. Rukes. Fortschrittliche Gas- und Dampfturbinenprozesse zur Wirkungsgrad- und Leistungssteigerung bei GUD-Kraftwerken. *VDI Berichte*, (1182):71–87, 1995.

[35] K. Y. Kim and W. R. Marshall. Drop-size distributions from pneumatic atomizers. *AIChE Journal*, 17(3):575–584, May 1971.

[36] G.W. Koroll and S.R. Mulpuru. The Effect of Dilution with Steam on the Burning Velocity and Structure of Premixed Hydrogen Flames. *Symposium (International) on Combustion*, 21(1):1811–1819, Jan 1988.

[37] O. Krüger. *On the Influence of Steam in Premixed Hydrogen Flames for Future Gas Turbine Applications*. PhD Thesis, Technische Universität Berlin, 2015.

[38] I. Langmuir and K. Blodgett. A Mathematical Investigation of Water Droplet Trajectories. Technical report, Air Material Comand, Wright Patterson Air Force Base, 1946.

[39] M. Lauer. *Determination of the Heat Release Distribution in Turbulent Flames by Chemiluminescence Imaging*. PhD Thesis, Technische Universität München, 2011.

[40] C. Lechner. *Stationäre Gasturbinen.* Springer Berlin Heidelberg, 2010.

[41] T. LeCong and P. Dagaut. Experimental and Detailed Modeling Study of the Effect of Water Vapor on the Kinetics of Combustion of Hydrogen and Natural Gas, Impact on NO_x. *Energy & Fuels*, 23(2):725–734, Feb 2009.

[42] A. Lefebvre. *Atomization and Sprays.* CRC Press, 1988.

[43] A.H. Lefebvre and D.R. Ballal. *Gas Turbine Combustion: Alternative Fuels and Emissions.* CRC Press, 2010.

[44] S. Lellek, C. Barfuß, and T. Sattelmayer. Experimental Study of the Interaction of Water Sprays With Swirling Premixed Natural Gas Flames. *Journal of Engineering for Gas Turbines and Power*, 139(2):021506, Sep 2016.

[45] S. Lellek and T. Sattelmayer. Influence of Water Injection on Heat Release Distribution, Lean Blowout and Emissions of a Premixed Swirl Flame in a Tubular Combustor. In *ASME Turbo Expo 2015: Turbomachinery Technical Conference and Exposition Volume 4A: Combustion, Fuels and Emissions.* ASME International, Jun 2015.

[46] S. Lellek and T. Sattelmayer. NO_x-Formation and CO-Burnout in Water Injected, Premixed Natural Gas Flames at Typical Gas Turbine Combustor Residence Times. In *ASME Turbo Expo 2017: Turbomachinery Technical Conference and Exposition Volume 4A: Combustion, Fuels and Emissions*, 2017.

[47] H. Liu. *Science and Engineering of Droplets: Fundamentals and Applications.* Elsevier Science, 1999.

[48] A.N. Mazas, B. Fiorina, D.A. Lacoste, and T. Schuller. Effects of Water Vapor Addition on the Laminar Burning Velocity of Oxygen-Enriched Methane Flames. *Combustion and Flame*, 158(12):2428–2440, Dec 2011.

[49] B.J. McBride, S. Gordon, and M.A. Reno. Coefficients for Calculating Thermodynamic and Transport Properties of Individual Species. *NASA Technical Memorandum 4513*, 1993.

[50] W.K. Metcalfe, S.M. Burke, S.S. Ahmed, and H.J. Curran. A Hierarchical and Comparative Kinetic Modeling Study of C1 - C2 Hydrocarbon and Oxygenated Fuels. *International Journal of Chemical Kinetics*, 45(10):638–675, Aug 2013.

[51] G. Mie. Beiträge zur Optik trüber Medien, speziell kolloidaler Metallösungen. *Annalen der Physik*, 330(3):377–445, 1908.

[52] T. Miyauchi, Y. Mori, and T. Yamaguchi. Effect of Steam Addition on NO Formation. *Symposium (International) on Combustion*, 18(1):43–51, 1981.

[53] M.J. Moore. NO_x Emission Control in Gas Turbines for Combined Cycle Gas Turbine Plants. *Proceedings of the Institution of Mechanical Engineers, Part A: Journal of Power and Energy*, 211(1):43–52, Jan 1997.

[54] C. Morris and M. Pehnt. *Energy Transition - The German Energiewende.* Heinrich Böll Foundation, 2012.

[55] M. Nič, J. Jirát, B. Košata, A. Jenkins, and A. McNaught, editors. *IUPAC Compendium of Chemical Terminology.* International Union of Pure and Applied Chemistry (IUPAC), Jun 2009.

[56] R. Pavri and G.D. Moore. Gas Turbine Emissions and Control. Technical Report, GE Power Systems, 2001.

[57] N. Peters. The Turbulent Burning Velocity for Large-Scale and Small-Scale Turbulence. *Journal of Fluid Mechanics*, 384:107–132, Apr 1999.

[58] N. Peters. *Turbulent Combustion.* Cambridge University Press (CUP), 2000.

[59] H. Pitsch. CEFRC Combustion Summer School. Technical Report, RWTH Aachen, 2014.

[60] T. Poinsot and D. Veynante. *Theoretical and Numerical Combustion.* Edwards, 2005.

[61] S.B. Pope. *Turbulent Flows.* Cambridge University Press, 2000.

[62] L. Prandtl. *Guide to the Theory of Flow.* 1944.

[63] G. Pretzler, H. Jäger, T. Neger, H. Philipp, and J. Woisetschläger. Comparison of Different Methods of Abel Inversion Using Computer Simulated and Experimental Side-On Data. *Zeitschrift für Naturforschung A*, 47(9), Jan 1992.

[64] A. Putnam. Integratable Form of Droplet Drag Coefficient. *Journal of the American Rocket Society*, 1961.

[65] W.E. Ranz and W. R. Marshall. Evaporation from Drops. *Chemical Engineering Progress*, 48(3):173–180, 1952.

[66] T. Richter. *Zerstäuben von Flüssigkeiten.* Expert-Verlag GmbH, 2016.

[67] J. Sangl. *Erhöhung der Brennstoffflexibilität von Vormischbrennern durch Beeinflussung der Wirbeldynamik.* PhD Thesis, Technische Universität München, 2011.

[68] B. Schetter. Gas Turbine Combustion and Emission Control. In *VKI Lecture Series on Combined Cycles for Power Plants*, Aug 1993.

[69] M. Schorr. Gas Turbine NO_x Emissions Approaching Zero - Is it Worth the Price? Technical Report, GE Power Generation, 1999.

[70] R. Seiser and K. Seshadri. The Influence of Water on Extinction and Ignition of Hydrogen and Methane Flames. *Proceedings of the Combustion Institute*, 30(1):407–414, Jan 2005.

[71] C.G. Seydel. *Thermodynamische Auslegung und Potentialstudien von Heavy-Duty Gasturbinen für kombinierte Gas- und Dampfkraftwerke.* PhD Thesis, Ruhr Universität Bochum, 2014.

[72] G.P. Smith, D.M. Golden, M. Frenklach, N.W. Moriarty, B. Eiteneer, M. Goldenberg, C.T. Bowman, R.K. Hanson, S. Song, W.C. Gardiner, V.V. Jr. Lissianski, and Z. Qin. http://www.me.berkeley.edu/gri_mech/.

[73] N. Stadlmair, P. Mohammadzadeh Keleshtery, M. Zahn, and T. Sattelmayer. Impact of Water Injection on Thermoacoustic Modes in a Lean Premixed Combustor Under Atmospheric Conditions. In *ASME Turbo*

Expo 2017: Turbomachinery Technical Conference and Exposition Volume 4A: Combustion, Fuels and Emissions, 2017.

[74] S. Steinbach. *Einfluss der Transportvorgänge auf die Effizienz von Harnstoffkatalysatoren in SCR-Abgasanlagen.* PhD Thesis, Technische Universität München, 2007.

[75] M. Stieß. *Mechanische Verfahrenstechnik - Partikeltechnologie 1.* Springer Berlin Heidelberg, 2008.

[76] A. Stodola. *Dampf- und Gasturbinen.* Springer Nature, 1924.

[77] M. Suyari and A. Lefebvre. Drop-Size Measurements in Air-Assisted Swirl Atomizer Sprays. In *Central States Combustion Institute Spring Meeting*, 1986.

[78] W. Traupel. *Thermische Turbomaschinen 2.* Springer, 2001.

[79] S. Turns. *An Introduction to Combustion: Concepts and Applications.* McGraw Hill Book Co, 2011.

[80] U.S. Environmental Protection Agency. Alternative Control Techniques Document - NO_x Emissions from Stationary Gas Turbines. Technical Report, U.S. Environmental Protection Agency, 1993.

[81] T. Waim. Düsenentwicklung für die Urea-SCR Technik von Medium Speed Diesel Motoren. Master Thesis, Technische Universität München, 2012.

[82] J. Warnatz, U. Maas, and R.W. Dibble. *Combustion.* Springer Berlin Heidelberg, 2006.

[83] A. Wasicek. Machbarkeitsstudie für eine Gasturbine mit Wassereindüsung zwischen Verdichteraustritt und Brennkammereintritt. Master Thesis, Technische Universität Wien, 2003.

[84] G. Wozniak. *Zerstäubungstechnik.* Springer, 2012.

[85] Y.B. Zeldovich. The Oxidation of Nitrogen in Combustion Explosions. *Acta Physicochimica USSR*, (21):277–628, 1946.

[86] D. Zhao, H. Yamashita, K. Kitagawa, N. Arai, and T. Furuhata. Behavior and Effect on NO_x Formation of OH Radical in Methane-Air Diffusion Flame with Steam Addition. *Combustion and Flame*, 130(4):352–360, Sep 2002.

A Supervised Theses

In the course of this work, the following student theses (Bachelor Thesis, Semesterarbeit, Master Thesis) have been prepared under the author's supervision. Parts of the students' work is included in this thesis. The author would like to thank the students for their commitment and their support of the research project.

Student	**Thesis**
Michael Jud	CFD-gestützte Auslegung eines Vormischbrenners, 2014
Patrick Jiskra	Gasturbinenverbrennung mit Wasserinjektion: CFD-Studie verschiedener Injektionssysteme, 2014
Severin Reiz	Water Injection in Gas Turbines - Kinetic Modeling with Cantera, 2014
Christoph Barfuß	Wassereindüsung in eine Gasturbinenbrennkammer mit Methan-Vormischflamme: LIF- und OH*-Chemilumineszenz Analyse, 2015
Simon Tartsch	CO-Messung in vorgemischten Erdgasflammen: Reaktionskinetische Untersuchungen sowie thermische Auslegung einer wassergekühlten Messlanze, 2015
David Gutierrez de Arcos	Experimental Characterization of a Water Spray from a Two-Fluid Atomizer with Laser Diffraction Measurements, 2015
Jose Pintor	Local Species Concentration Measurements in a Test Rig Combustion Chamber with Water Injection, 2016
Patrick Strempfl	Simulation einer vorgemischten Erdgasdrallflamme mit Wasserinjektion, 2016

B Previous Publications

Significant parts of this thesis have already been published by the author in conference proceedings and journal papers [44–46]. All relevant publications are registered according to the valid doctoral regulations. However, not all of them are quoted explicitly everywhere. Whether these personal prior printed publications were referenced depends on maintaining comprehensibility and providing all necessary context. A list of these papers is shown below.

1. S. Lellek, and T. Sattelmayer: Influence of Water Injection on Heat Release Distribution, Lean Blowout and Emissions of a Premixed Swirl Flame in a Tubular Combustor Distribution. *Proceedings of the ASME Turbo Expo 2015*, GT2015-42602, Montreal, Canada, June 15-19, 2015
2. S. Lellek, C. Barfuß, and T. Sattelmayer: Experimental Study of the Interaction of Water Sprays With Swirling Premixed Natural Gas Flames. *Journal of Engineering for Gas Turbines and Power*, 139(2), 021506, Sept. 2016
3. S. Lellek, and T. Sattelmayer: NO_x-Formation and CO-Burnout in Water Injected, Premixed Natural Gas Flames at Typical Gas Turbine Combustor Residence Times. *Proceedings of the ASME Turbo Expo 2017*, GT2017-63128, Charlotte, NC, USA, June 26-30, 2017 (recommended for publication in *Journal of Engineering for Gas Turbines and Power*)